

## **INFORMATION TO USERS**

**This manuscript has been reproduced from the microfilm master. UMI films the text directly from the original or copy submitted. Thus, some thesis and dissertation copies are in typewriter face, while others may be from any type of computer printer.**

**The quality of this reproduction is dependent upon the quality of the copy submitted. Broken or indistinct print, colored or poor quality illustrations and photographs, print bleedthrough, substandard margins, and improper alignment can adversely affect reproduction.**

**In the unlikely event that the author did not send UMI a complete manuscript and there are missing pages, these will be noted. Also, if unauthorized copyright material had to be removed, a note will indicate the deletion.**

**Oversize materials (e.g., maps, drawings, charts) are reproduced by sectioning the original, beginning at the upper left-hand corner and continuing from left to right in equal sections with small overlaps.**

**Photographs included in the original manuscript have been reproduced xerographically in this copy. Higher quality 6" x 9" black and white photographic prints are available for any photographs or illustrations appearing in this copy for an additional charge. Contact UMI directly to order.**

**Bell & Howell Information and Learning  
300 North Zeeb Road, Ann Arbor, MI 48106-1346 USA**

**UMI<sup>®</sup>**  
**800-521-0600**



# **Design of a Composite Link for the Freedom-7 Haptic Hand Controller**

by

**John McDougall**

**Department of Mechanical Engineering**

**McGill University, Montreal**

**A Thesis Submitted to the Faculty of Graduate Studies and Research  
in Partial Fulfillment of the Requirements of the Degree of  
Master of Engineering**

**© John McDougall 1997**



National Library  
of Canada

Acquisitions and  
Bibliographic Services

395 Wellington Street  
Ottawa ON K1A 0N4  
Canada

Bibliothèque nationale  
du Canada

Acquisitions et  
services bibliographiques

395, rue Wellington  
Ottawa ON K1A 0N4  
Canada

*Your file* *Votre référence*

*Our file* *Notre référence*

The author has granted a non-exclusive licence allowing the National Library of Canada to reproduce, loan, distribute or sell copies of this thesis in microform, paper or electronic formats.

The author retains ownership of the copyright in this thesis. Neither the thesis nor substantial extracts from it may be printed or otherwise reproduced without the author's permission.

L'auteur a accordé une licence non exclusive permettant à la Bibliothèque nationale du Canada de reproduire, prêter, distribuer ou vendre des copies de cette thèse sous la forme de microfiche/film, de reproduction sur papier ou sur format électronique.

L'auteur conserve la propriété du droit d'auteur qui protège cette thèse. Ni la thèse ni des extraits substantiels de celle-ci ne doivent être imprimés ou autrement reproduits sans son autorisation.

0-612-44026-5

Canada

# ***Abstract***

**The Freedom-7 Haptic Hand Controller is a high performance haptic device developed jointly between McGill and MPB Technologies. This thesis discusses previous work in the field of haptic devices, the research into the bonding of metals to composites, optimization procedures for composite laminates, and includes a brief overview of human haptic capabilities. The discussion includes the analysis process used to design a composite box-beam structure to replace one link of the translation stage of the hand controller, and to determine the optimal bond characteristics for the joining of a small diameter composite tube to a metal end fitting. Iterative finite element analysis as well as failure and vibration testing were used to determine the efficiency of the designs, and to measure the improvements in the dynamic properties of the haptic device's structure. Though certain difficulties were encountered during the manufacturing of the prototype that lead to disappointing physical test results, the simulations prove that a haptic device such as the Freedom-7 could greatly benefit from the inclusion of composite materials into the structure.**

# *Résumé*

Le contrôleur haptique **Freedom-7** est un dispositif de haute performance développé conjointement entre l'Université McGill et MPB technologies. Cette thèse résume les travaux existants sur les dispositifs haptiques, les méthodes d'adhérence entre les matériaux composés et les métaux, les procédures pour optimiser la structure des laminés ainsi que les recherches sur les capacités du système haptique humain. La discussion fait part de l'analyse d'une structure monocoque en fibre de carbone utilisée pour remplacer un joint d'aluminium dans le dispositif. De plus, l'optimisation de la géométrie d'un joint adhésif entre un tube en fibre de carbone et une garniture en aluminium est expérimentée. L'efficacité du design a été évaluée par une analyse empirique ainsi que différents tests mesurant la résistance et la vibration. Ces derniers servent aussi à évaluer les améliorations des caractéristiques dynamiques de la structure du dispositif. Certains problèmes de fabrication nuisent à la performance du dispositif lors des tests physiques, mais les simulations par ordinateur prouvent que la possibilité existe d'accroître considérablement la performance avec l'utilisation de matériaux avancés.

# ***Dedication***

**This work is dedicated to several groups of people, without whose support it never would have been completed. To my parents, for getting me here. To my friends for supporting me. To Prof. Larry Lessard for putting up with me. And to Emilie for being there for me.**

**Thanks must also go to Prof. Vincent Hayward for initiating the Freedom- 7 project. Also, to the people at MPB Technologies, Dr. Ian Sinclair, Sander Boelen, and Jean Poulin for all their help in the initial stages of the project. Special thanks must also go to Dr. Diao Xiaoxue for his invaluable help at the end of the project.**

# *Table of Contents*

1. Introduction to Freedom-7.....	1
1.1 Haptic Devices .....	1
1.2 Requirements for Haptic Devices.....	2
1.3 Advanced Material Advantages .....	4
1.4 Freedom-7 .....	5
1.5 Objectives of this thesis.....	11
2. Literature Review .....	12
2.1 General Haptics .....	12
2.2 Literature Review of Bonded Joints.....	17
2.3 Literature Review of Laminate Optimization.....	23
3. Design of Bonded Tubes .....	29
3.1 Introduction .....	29
3.2 Material Survey of Composite Tubes.....	29
3.3 Geometry and Parameter Variation of Bonded Inserts.....	33
3.4 Axisymmetric Finite Element Models .....	34
3.5 Results of Parameter Variation .....	36
3.6 Three Dimensional Finite Element Model .....	43
4. Bonding Tests.....	49
4.1 Three-Point Bend Test .....	49
4.2 Calculations for Bending Moment Load Case .....	51
4.3 Test Results .....	53
5. Design of Box Beam .....	56
5.1 Introduction .....	56
5.2 Dimensional Requirements for the Box Beam.....	56
5.3 Finite Element Model of the Distal Stage Linkage .....	58
5.4 Results of Finite Element Model.....	60
6. Box Beam Prototype .....	61
6.1 Carbon Fiber Box Beam.....	61

6.2 End Fittings .....	65
6.3 Bonding of End Fittings .....	66
6.4 Structural Tests on Freedom-7 .....	67
6.5 Frequency Response of Translation Stage .....	68
6.6 Refined Finite Element Model of Distal Stage Linkage .....	71
6.7 Maximum Acceleration Test.....	76
6.8 Summary for Box Beam Prototyping and Testing .....	77
7. Conclusions and Recommendations.....	79
7.1 Recommendations for Future Work.....	80
8. Bibliography.....	81
1. Appendix A .....	9-i
2. Appendix B .....	10-ix

# *Table of Figures*

Figure 1.4.1 - PHANToM .....	5
Figure 1.4.2 - PER-Force device .....	6
Figure 1.4.3 - SARCOS dexterous arm master .....	6
Figure 1.4.4 - Large Workspace Hand Controller (LWHC).....	7
Figure 1.4.5 - STYLUS Hand Controller .....	8
Figure 1.4.6 - Freedom-7 Translation Stage.....	9
Figure 1.4.7 - Freedom-7 Distal Stage .....	10
Figure 1.4.8 - The Freedom-7 Haptic Hand controller.....	10
Figure 3.2.1 - High-tech Arrow Shafts.....	30
Figure 3.3.1 - Bond Geometry for Parameter Variation.....	33
Figure 3.4.1 - Axisymmetric Finite Element Model of Bonded Geometry.....	34
Figure 3.4.2 - Reference Locations on Bond Geometry.....	35
Figure 3.5.1- Variation of Peak Principal Stress with Adherend Wall Thickness .....	37
Figure 3.5.2- Variation of Peak Principal Stress with Axial Engagement.....	37
Figure 3.5.3- Variation of Peak Principal Stress due to Bond Line Thickness .....	38
Figure 3.5.4 - Maximum Principal Stress Contours in Epoxy Material for Test 1.4 (Bond AD Broken) .....	38
Figure 3.5.5 - Maximum Principal Stress Contours in Epoxy Material for Test 1.1 (Bond AD Exists) .....	39
Figure 3.5.6 - Maximum Principal Stress Contours in Epoxy Material with Epoxy Fillet for Test 1.3 (Bond BAD Exists).....	39
Figure 3.5.7 - Variation of Principal Stress Along Bond due to Adherend Thickness (a) .....	40
Figure 3.5.8 - Variation of Principal Stress Along Bond due to Bond Line Thickness (l).....	41
Figure 3.6.1 - Three Dimensional Finite Element Model of Bonded Tube Geometry .....	43

<b>Figure 3.6.2 - Maximum Principal Stress Contours in Composite Tube</b>	
Close to Bonded Region.....	45
<b>Figure 3.6.3 - Maximum Principal Stress Contours for Bonded Face of</b>	
Aluminum Insert .....	46
<b>Figure 3.6.4 - Maximum Principal Stress Contours in Epoxy Bond Material .....</b>	<b>47</b>
<b>Figure 4.1.1 - Sketch of three-point bend test setup.....</b>	<b>49</b>
<b>Figure 4.1.2 - Three-point bending test specimen.....</b>	<b>50</b>
<b>Figure 4.1.3- Variation of dimensions for three point bending tests.....</b>	<b>51</b>
<b>Figure 4.2.1- Shear and bending moment diagrams for three-point bending tests.....</b>	<b>51</b>
<b>Figure 4.3.1 - Graph of piston force vs. centerpoint displacement .....</b>	<b>54</b>
<b>Figure 4.3.2 - Broken three-point bend specimen .....</b>	<b>54</b>
<b>Figure 5.2.1 - Clearance area for the distal stage driving strings .....</b>	<b>57</b>
<b>Figure 5.2.2 - Exploded view of carbon fiber distal stage assembly.....</b>	<b>57</b>
<b>Figure 6.1.1 - Time-temperature Profile for LTM25 Cure Cycle.....</b>	<b>62</b>
<b>Figure 6.1.2 - Lay-up Procedure for Composite Box-Section.....</b>	<b>64</b>
<b>Figure 6.6.1 - Refined model of distal linkage for vibration simulation.....</b>	<b>71</b>
<b>Figure 6.6.2 - Refined finite element model of distal linkage with added</b>	
cover for vibration simulation .....	72
<b>Figure 6.6.3 - Normal mode vibration in x direction of distal stage with an</b>	
added cover .....	73
<b>Figure 6.6.4 - Normal mode vibration in x direction for uncovered distal stage .....</b>	<b>73</b>
<b>Figure 6.6.5 - Stress contours in uncovered pulley block base .....</b>	<b>75</b>
<b>Figure 6.6.6 - Stress contours in covered pulley block base .....</b>	<b>75</b>

# ***Glossary of Terms***

***active DOF*** - any DOF that can exert a force or torque on the user's hand / body

***actuation dimensionality*** - the number of active degrees-of-freedom in the device

***adherend*** - the part of a bonded joint that is being glued

***adhesive*** - the glue holding the two adherends together

***actuator*** - any system to convey torque or force to a part of the robotic device

***backdriveable*** - the ability to move a robotic structure by applying force to the end effector without any aiding joint torques

***backlash*** - small movements in bearings and other joints

***bi-directional*** - a data stream that flows in two directions, i.e. read and write

***bond line thickness*** - the distance between two adherends that is filled with adhesive

***constrained impedance*** - infinite stiffness contact

***crispness*** - subjective term referring to the quality of a sensation felt through a haptic interface

***cure*** - the process of heating, pressurizing and then cooling an epoxy to change the state from liquid to solid

***degrees-of-freedom (DOF)*** - the number of directions in which a device is free to move in either translation or rotation

***device intrusion*** - physical presence of the haptic device in the operator's workspace

***engagement*** - the length of the adhesive bond

***fidelity*** - the ability of a haptic interface to accurately represent a virtual environment

***fiber orientation*** - the direction along which the fibers in the composite material are aligned

***haptics*** - the branch of study dealing with the human sense of touch

***master robot*** - a robotic structure that controls through teleoperation another robot

***mold*** - a rigid tool used to form the uncured composite material into a useable shape

***slave robot*** - a robotic structure that is controlled by another robot or hand controller

***teleoperation*** - action transmitted over a distance by an electronic signal

*transparency* - term used in describing the haptic interface, referring to the inability of the operator to sense the interface

*unconstrained impedance* - free motion

*vacuum bag* - a thin plastic sheet used to create an airtight covering over a composite part in order to apply vacuum pressure to the part during the cure

*virtual environment* - a computer representation of a real or imaginary environment

# ***1. Introduction to Freedom-7***

## **1.1 Haptic Devices**

In the short span of twenty years, the computer has gone from an expensive, novelty item to an essential tool that can be found in all walks of life. The gains in computing power have been enormous: early generations of computers were the size of a room and could do less than what most wristwatch calculators do today. This quantum leap in speed and capability, as well as an increasing demand for high speed access to information, has contributed to the incursion of the computer into every aspect of our lives.

With the increased speed of computers, users can exist and interact with virtual environments that would have been impossible to imagine only a decade ago. A virtual environment is a computer equivalent of the real world. It can be anything from a flight simulation to a museum, where the user can browse through thousands of rare paintings. The one thing about the virtual environment that remains constant is that it does not physically exist anywhere except as a collection of 1's and 0's in the binary memory of a computer.

Where before people could only experience these virtual environments through sight and sound, with the introduction of a variety of haptic devices they can now explore with the sense of touch also. Haptics is the branch of psychology that deals with the cutaneous sense data, in other words the data that is transmitted to the brain by the pressure receptors in the skin. Therefore, a haptic device is a device that will translate computer signals into pressure or force on the user. The skin pressure that the user feels from the device, combined with the visual and auditory inputs from the virtual environment, create a greater sense of being inside the environment generated by the computer.

The haptic device is a bi-directional interface [1] between the human user and the computer. It has to be able to accept user input as well as deliver its own data output

back to the user. The effectiveness of this delivery is what will differentiate a “good” haptic device from a “bad” one. However, determining the quality of this delivery is not as simple as it seems. The requirements for haptic devices are different from other robotic applications. For clarity, a set of terms will be used to describe the general attributed of all hand controllers:

- *DOF* - degrees-of-freedom
- *hand controller* - any device that serves as an interface between the user and virtual environment that is intended to be used by an operator’s hand
- *active DOF* - degrees-of-freedom on which there is force exerted by the hand controller
- *actuator* - any force or torque applicator
- *end-effector* - point at which the interface between human operator and hand controller occurs
- *FFB* - force feedback

## 1.2 Requirements for Haptic Devices

The earliest haptic devices were designed to give information to the users about force states in the real environment that they were controlling. These first FFB devices were connected physically to the remote environments by mechanical linkages such as wires. For instance, in the biplanes of World War I, the pilots could feel the forces on their control surfaces transmitted through their flight control sticks, making the control stick into a haptic device [2]. The first generation of haptic devices connected electronically to a remote environment were devised for use in the nuclear industry, to enable operations to be carried out in extremely hazardous environments [1,2]. These devices consisted of dynamically identical *master* and *slave* robots, since the computing power at the time was not sufficient to calculate extensive transformations between the two. The master refers to the controlling device, and the slave refers to the remote device.

In a virtual reality application, the most important concern is whether the operator feels like he/she is really inside the environment [3-7]. If the virtual environment seems

real, the interface between the user and the virtual space (i.e. the computer, the screen, the hand controller, etc.) are considered *transparent*. The operator does not notice that they are there. Unlike traditional robotic applications where end effector positioning is of great importance, in a hand controller application this precision comes secondary to the resolution of the device [1], due to the limited capacity of the human sensory system to absolutely locate a given point in space. Resolution is the maximum deflection about a stationary point that the device generates at an equilibrium state. A vibratory deflection caused by the control system, actuator inadequacies or structural faults decreases the transparency of the hand controller.

To achieve transparency in a haptic device like a hand controller, there are several key requirements that need to be met. First, the structure of the hand controller must have a very low inertia. If the operator is moving through free space inside the computer, they should not feel a large mass of the hand controller resisting their motions. The low inertia of the controller must be coupled with an almost constant and diagonal inertia tensor. Achieving an inertia tensor that is constant and diagonal will allow the inertia felt by the operator to be equal in all configurations of the hand controller mechanism. It will not seem heavier or lighter towards the edges of the workspace than it does in the middle. Furthermore, a low link inertia will increase the *crispness* of such FFB sensations as impact with an immovable wall. Minimizing the link inertia will increase the maximum acceleration that a given actuators can create at the end effector. The second requirement of the structure of the hand controller is link stiffness. The stiffer the links, the greater the dynamic benefits. The resonant natural frequency of a structure is dependent on its stiffness: the higher the stiffness the greater the natural frequency. With stiffer links comprising the structure of the hand controller, higher frequency phenomenon such as working a drill or scratching a rough surface with a pencil can be simulated without the danger of reaching a resonant frequency of the structure and inducing vibration. As the virtual pointer comes into contact with a solid wall, the computer needs to sample the pointer location and calculate a joint force consistent with the proximity to the wall. To achieve the *fidelity* of such a simulation, the response of the controller must be at a very high frequency, on the order of 200 Hz.

### **1.3 Advanced Material Advantages**

There are many advantages to the incorporation of advanced composite materials into the design and construction of a haptic hand controller. When designers restrict themselves to traditional materials, there is a limit to the design changes that can be made to optimize link stiffness to weight ratios. For traditional materials such as steel and aluminum, the stiffness and density are constant. Inevitably, compromise has to be made in one of the design areas.

With the increased use of advanced composite materials in many areas of industry, the design tools for applying these materials are becoming more available. As designers become more comfortable working with these materials, more advantages become apparent. The ability to tailor the material properties of a laminate for a specific task is unique to this type of material. A designer can optimize the material in a robotic link for tensile modulus and damping [8-14], two properties which are necessarily fixed in traditional materials. Designers are no longer restricted to modifications in the link cross sections to obtain desired results for link dynamics.

## 1.4 Freedom-7

There already exists several models of haptic devices that are used specifically for virtual reality applications. They can be divided into three categories. The first is the low DOF (degree-of-freedom) devices. These are haptic devices that have bi-directional data flow on three DOF's or less. They include the PHANToM [1,3,5,15,16] device (Figure 1.4.1), which is active in the three translational modes and has a three DOF rotational gimbal attached to a thimble that can be worn on the user's index finger. The Pantograph [1,16,17] has only two active translational modes. Work has been done at UBC to

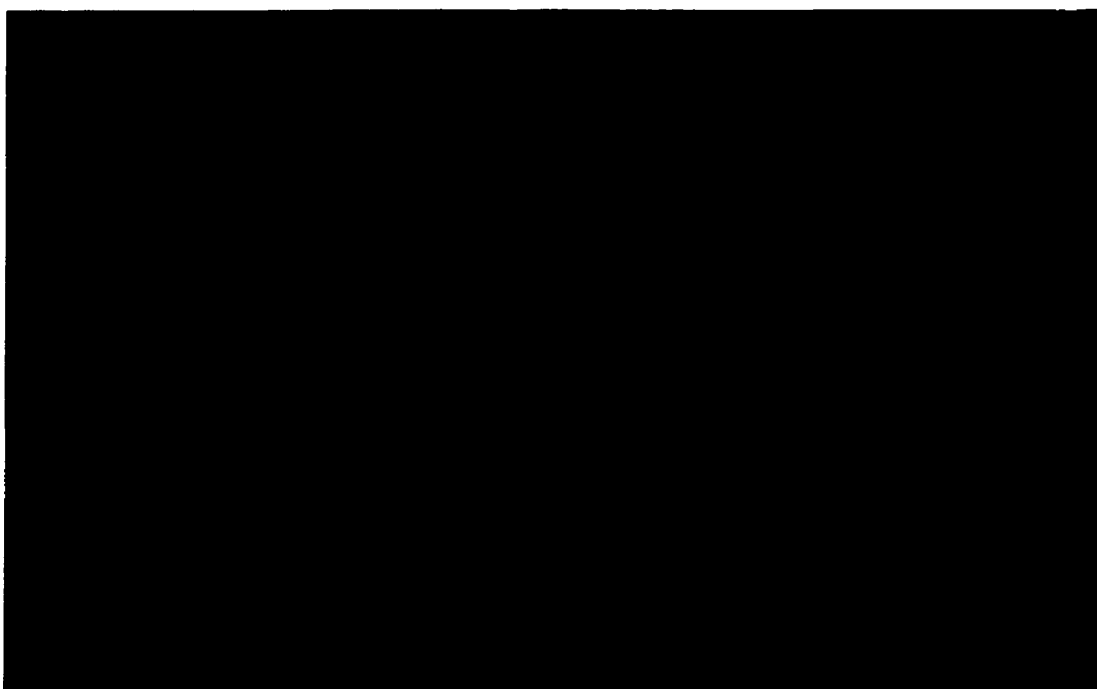


*Figure 1.4.1 - PHANToM*

include a third active rotational mode to the Pantograph [1]. As well, several haptic applications have used multiple Pantograph units simultaneously to obtain increased active DOFs [16]. There are several FFB joysticks on the market such as the Immersion Corporation's line of Impulse Sticks [18]. These devices can only provide an estimate of the task that the operator performs in the virtual environment. They are not sufficient to fully simulate a real system.



In the case of the PHANTOM device, the simulated environment is similar to a point probe. The user can investigate the virtual environment in the three Cartesian directions, but has no active rotational DOFs. This limits the variety and realism of the interactions that the user can have with the remote environment.

The high DOF devices have enough complexity to fully simulate an interaction with a virtual environment. They do not need to approximate a task but can represent it fully. Examples of these high DOF devices are the Texas 9-string and the SPIDAR-II, both stringed haptic interfaces [16], the PER-Force joystick from Cybernet Systems Co. [16] (figure 1.4.2), the SARCOS dexterous arm master (figure 1.4.3), and the FREFLEX

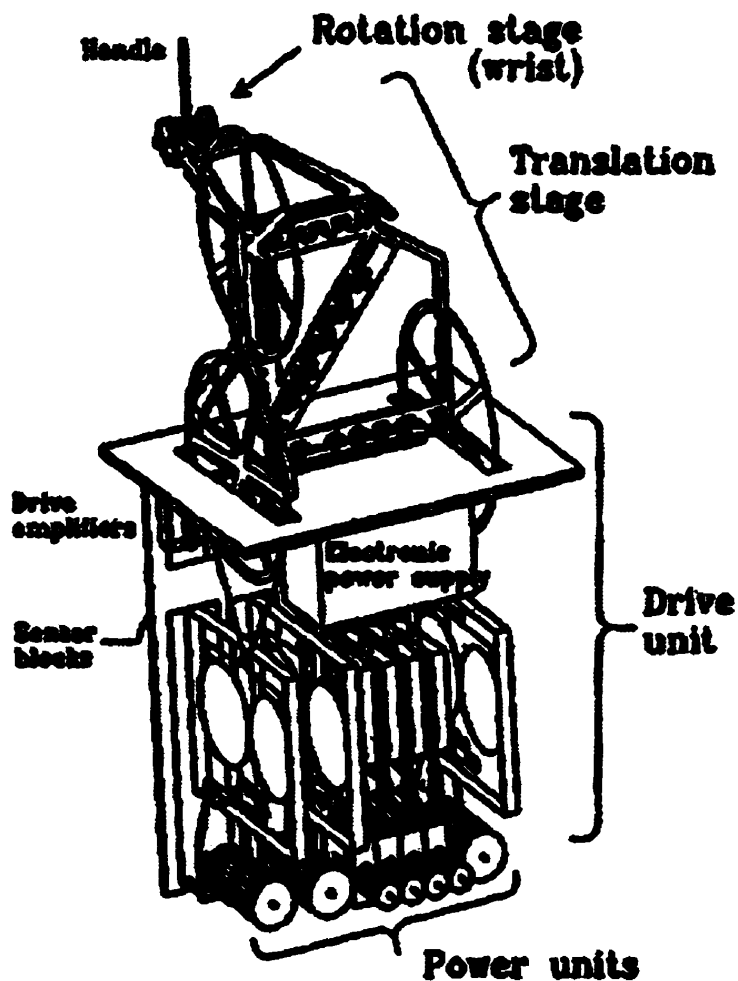
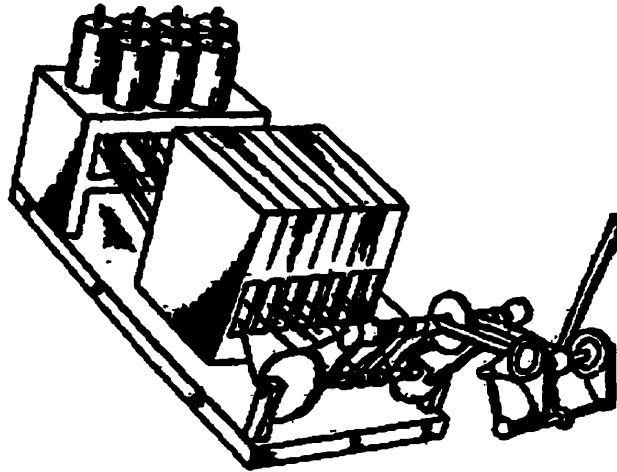


Figure 1.4.4 - Large Workspace Hand Controller (LWHC)



*Figure 1.4.5 - STYLUS Hand Controller*

exoskeleton masters, among many others. These FFB devices all have several drawbacks, the most common of which is high complexity and intrusion into the user's workspace [16].

Previous work by MPB and McGill resulted in two high DOF hand controllers. The first was a large workspace hand controller (LWHC) [6, 19]. It consisted of a 3-DOF rotational wrist mounted on a 3-DOF translational stage (see figure 1.4.4). Large friction loads consistent with extremely overloaded bearings were detrimental to the performance of the LWHC. Another device constructed at McGill was the cantilevered HC called the STYLUS [19]. The distal stage of this model was suspended from the end of a jointed cantilever arm (figure 1.4.5). The major drawback to this controller was the static load on the driving strings generated by the gravity vector. The high modulus polymeric strings required to drive the force feedback of the controller are prone to creep. This configuration would therefore be unacceptable for a production model.

The Freedom-7 hand controller is the latest high DOF hand controller to emerge from the cooperation between MPB and McGill [19]. It has six active DOF in the translation and rotational modes as well as an optional active seventh DOF at the end effector to simulate a plunger or a pair of scissors. The latest prototype, which exists in an all aluminum form, solves the problems associated with the previous two prototypes. The parallel design of the translation stage (figure 1.4.6) does not require the high modulus fibers for actuation, and they are restricted to the actuation of the distal stage only. Low friction, brush-less DC motors are used as direct-drive actuators on the translation stage and allow for counterbalancing of the gravity force vector. An improved design of the distal stage (figure 1.4.7) reduces the inertia felt by the operator. Simple tendon paths make assembly easier and allow for zero force on the fibers at equilibrium, eliminating any creep deformation. A schematic of the entire assembly of the Freedom-7 hand controller can be seen in figure 1.4.8.

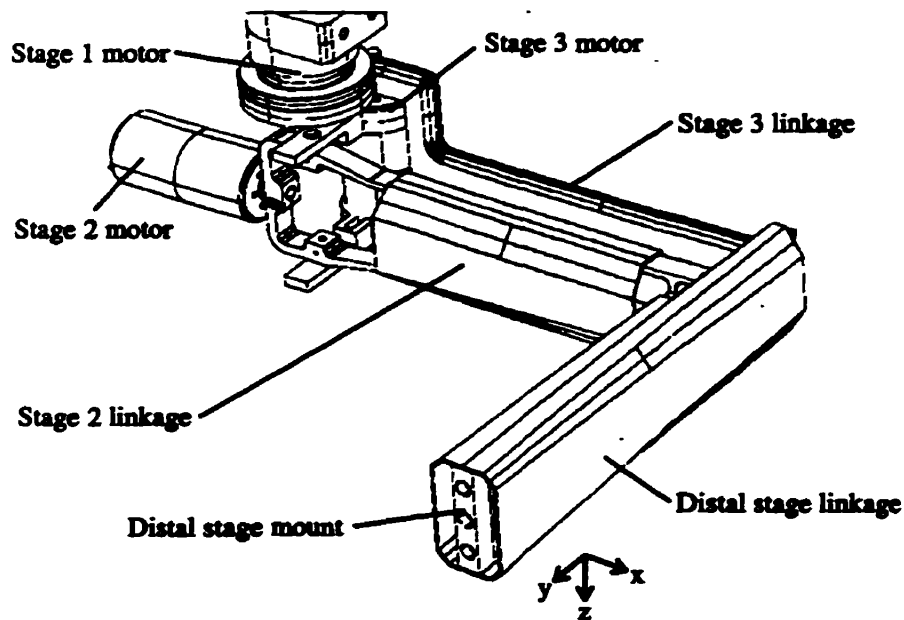


*Figure 1.4.6 - Freedom-7 Translation Stage*

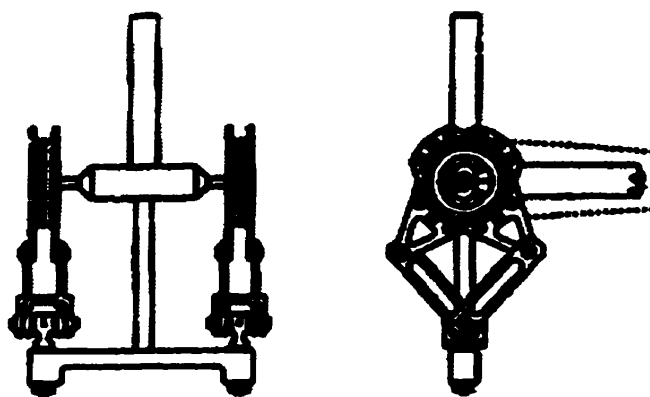


*Figure 1.4.7 - Freedom-7 Distal Stage*

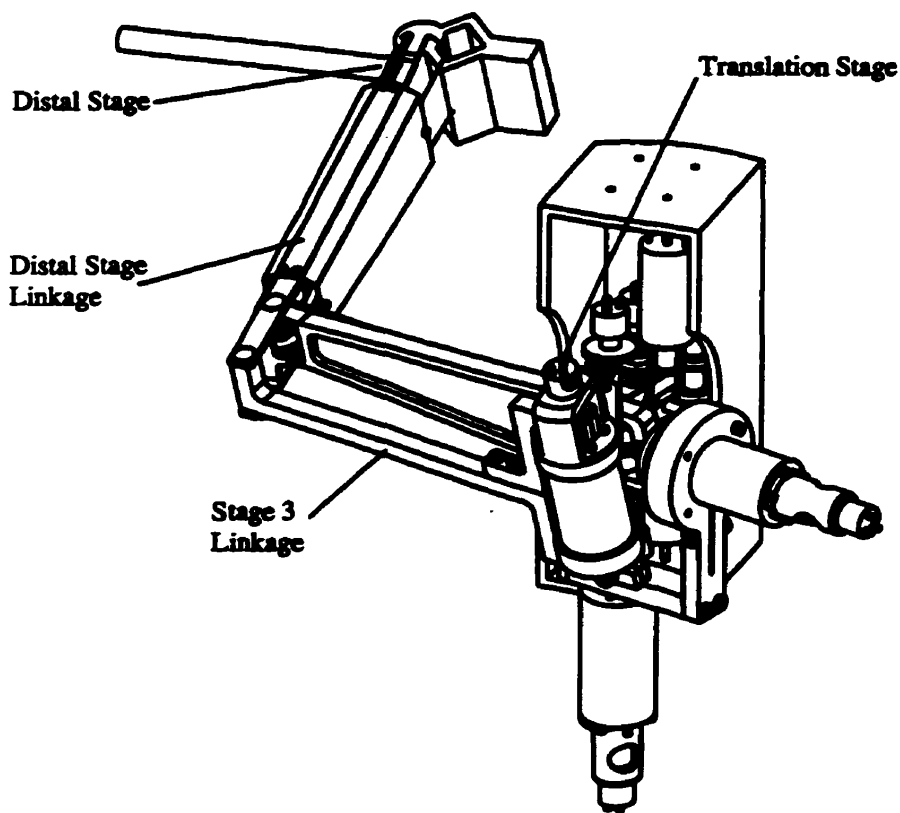


*Figure 1.4.8 - The Freedom-7 Haptic Hand controller*

## 1.5 Objectives of this thesis

There exists two avenues for improvement to this design that will be undertaken in this work. The first is to replace the stage 3 linkage (figure 1.4.6) by a small diameter, commercially available carbon fiber tube with bonded metal inserts. Second, the distal stage linkage (figure 1.4.6) will be replaced by a composite box-beam structure. The purpose of both these inclusions is to increase the stiffness of the resulting structure while decreasing the link mass and inertia. However, incremental improvements of the dynamic characteristics of haptic devices need to be measured based on specific performance criterion that do not correspond necessarily to those used for traditional robotic applications. As such, proper measurements have to be made to determine the overall effect the incorporation of advanced materials into the structure has on the performance of the haptic device.

The following research topics are associated with the design and inclusion of these two parts in the Freedom-7 haptic hand controller:

- Theory and application of proper end fixtures, i.e. proper design of composite metal interfaces will be addressed. The design of the metal inserts will be optimized for several basic geometric criteria.

- Lay-up choice for the optimization of a box beam structure will be examined. The choice of a lay-up for composite parts can be greatly affected by the applied load conditions.

- Optimization of composite parts for high natural frequency and high damping will be performed. The haptic hand controller requires a very high bandwidth, like many other potential applications for composite materials.

- Testing of bonded joint strengths in bending will be performed. This testing is rarely seen in the literature, where the most common forms of loading for a circular cross section joint are torsion and axial.

- Application of proper test methods to determine performance characteristics of haptic devices will be performed. There is very little in the way of serious performance criterion for haptic devices, and this topic should be addressed in order to simplify further work in this field.

## ***2. Literature Review***

### **2.1 General Haptics**

Before any action is taken to optimize the construction of a haptic device, several questions need to be answered. First of all, what factors will contribute most to the improvement of the device? In [1], Hayward and Strong propose several discreet performance measures that can be used to quantitatively determine the standard of a haptic device. These measures include degrees of freedom associated with the device (actuated and non-actuated), the type of device-body interface, the range of motion of the device, peak force, inertia and damping and peak acceleration. However, many of these characteristics can be subject to different interpretations; for instance should the inertia be measured from the point of view of the actuators or the user, and does the peak force mean the maximum actuator force, the highest transient force that can be felt by the user, or the maximum continuous force that can be applied by the end effector? It becomes very important to determine which factor will most affect the eventual performance of a device because expensive incremental improvements to non-critical factors will not serve to increase the *feel* of the device.

The authors of [1], Hayward and Astley, suggest that the most important characteristic of a haptic interface is *bi-directionality*. The haptic channel, as a human sense, will both receive input from and give output to the environment. Therefore, any device that seeks to use this sensory channel must be bi-directional as well. Achieving both reading and writing of haptic information by a mechanical device requires a design that accounts for the inherent limitations and capabilities of the human haptic organs such as the fingertips, hands, and arms. In [2], Durlach and Mavor review a great deal of work that has been done to measure the sensing capabilities and limits of the human sense of touch, including both the hand and the arm. Though a full characterization of the human sense of touch is well beyond the scope of this work, certain elements of previous work can be used to help determine meaningful criterion for the performance measures and design goals of the haptic interface. The human hand has 22 degrees of freedom of

motion actuated by muscles and tendons, not including the many other sensory systems such as pain, pressure, heat, etc. that are actuated by numerous sensory nerve endings located under the surface of the skin. Haptic operations are divided into two categories, *exploration* and *manipulation*. Exploration is dominated by the sensory system located in the skin, and serves to determine the material and textural properties of the object being explored. Manipulation is a motor dominated operation that consists of modifying the environment through the exertion of forces on an object, and requires bi-directionality of the data stream for successful task completion. The haptic data stream itself can be divided into two parts: the *kinesthetic* and the *tactual* data. Tactual data refers to the data transmitted by the nerve endings under the skin and dominates the exploration tasks. The kinesthetic data refers to the positioning sense derived by the nervous system from information on joint angles and tendon forces. This data stream will obviously dominate the manipulation tasks, and is the most interesting for the purposes of this work. Any mechanical design of a haptic interface will be heavily dependent on the limitations of the kinesthetic data resolution. Of the works that the authors [2] reviewed, the following data was provided for the kinesthetic data resolution for the average human:

1. It is possible to detect joint rotations of a fraction of a degree over the time interval of seconds [2].
2. The kinesthetic sense had a bandwidth on the order of 20-30 Hz, but goes up to 1 kHz for the tactual data stream [2].
3. The farther the joint is from the center of the body (the more distal the joint) the lower the sensitivity to absolute joint rotations. The method for determining this is called the *just-noticeable-difference* (JND). The JND for the finger joints is 2.5 degrees, for the wrist and elbow joint is 2 degrees and for the shoulder joint is 0.8 degrees [2].
4. The kinesthetic sense can determine to within 8 percent the differences in position of a fixed point in space or a repeated movement [2].
5. A stiffness of at least 25 N/mm is needed for a surface to be perceived as rigid [2].

In [20], Hayward discusses previous work that was done to measure the effect of these haptic parameters on an eventual design of a haptic interface. The tests were performed in a six DOF simulator on various subjects. The conclusions of these tests were that the sensitivity of the subjects to discrete motions varied much with the subject's training. A surgeon had the best sensory discretization. They also concluded that, as the most demanding senses were involved with high frequency motions, the actuation of the haptic device is much more important than its overall precision in absolute positioning. This conclusion is contrary to conventional robotic practice where the end effector positioning is normally of the utmost importance, even more so than available joint torques and link speeds. Thus high frequency resolution becomes an important design criteria for haptic devices.

Other researchers in the haptic design area have come up with requirements for haptic devices. In [3], Massie defines the ultimate feedback device as a "device ... able to apply forces, torques and dermal stimulation to any part of the hand." This is obviously an immensely complex task. Just the degrees of freedom of mechanical motion in the hand, 22 in all, would make this kind of haptic device prohibitively complex. Massie goes on to list three subjective measures of a potentially realizable haptic device. They are *device intrusion*, *actuation dimensionality* and *fidelity*. Device intrusion is simply an ergonomic function of the design, and really has little to do with the dynamic behavior of the haptic device. Actuation dimensionality refers to the active number of DOF's in the device. Fidelity is the ability of the haptic device to accurately simulate the virtual event. To achieve sufficient fidelity in a device, it should necessarily be ground referenced. If the device is mounted to a fixed surface such as the floor or a rigid tabletop, the forces that it will exert on the operator will cause a reaction force on the ground, not on another part of the operator's body as would be felt for a body referenced device. This will allow for a more realistic impression of the virtual environment. However, Massie states that a ground based device with long linkages to allow for a greater range of motion will reduce the fidelity of the simulation.

In [21], Lawrence and Chapel define the ideal hand controller in terms of mechanical impedance, and use this to determine a range within which a non-ideal hand

controller can function as an ideal hand controller. They state that, with the ideal hand controller, when there is no contact created in the virtual environment, the user should feel no force, and that when in contact with a virtual wall or other immovable object, the stiffness should be infinite. They suggest that the *transparency* of the system will be improved by increasing structural stiffness and torque output of the hand controller, while decreasing link stiffness. Lawrence and Chapel propose two mechanical impedances, the *constrained impedance* and the *unconstrained impedance*, which correspond to infinite stiffness contact and free motion respectively, as two measures of performance for the hand controller. The unconstrained impedance is a function of the force sensing threshold of the human haptic system, and the roll-off frequency above which a human operator is unable to follow a sinusoidal input to the hand controller, as well as the amplitude of this input. The simple sinusoidal input is a method of measurement that can be constant for all haptic devices. The value for the unconstrained impedance required by any haptic device will therefore be very sensitive the abilities and training of individual operators. The constrained impedance for a low frequency contact situation is a function of the maximum reasonable force exerted by the user divided by the kinesthetic resolution of the human operator. At high frequency, the low frequency factor comes into a more complex equation including the same roll-off frequency and amplitude for the sinusoidal input to the human operator. Therefore, the constrained impedance for the ideal haptic device is also very dependent on the qualities and training of the operator, except in the low frequency case. A device that has enough fidelity for use by a construction worker would not necessarily feel good to a surgeon. It is possible to determine generally the haptic sensing abilities of the targeted user population, but to do so with any degree of accuracy is almost impossible. However, we can assume for the purposes of the Freedom-7 project that, as the target user population for this device is surgical training [22], the structural impedances on the mechanism will be very demanding.

In [23], Fasse and Hogan attempted to measure the haptic perception of a group of subjects in a methodical statistical way. Their results show that there is much more work to be done in order to model and measure the haptic perception of humans. Two experiments were performed to gauge the subjects' ability to discriminate between

lengths and angles in virtual rectangles and triangles respectively. The subjects all had similar discrimination patterns, but the patterns themselves did not fit into a physical Reimannian representation of space. There seems to be little quantifiable link between the traditional methods of mechanics and human haptic perception, and a different approach is required if deterministic criteria are to be introduced into this facet of engineering.

In general, the design goals of the haptic hand controller for control and stability in an interface with a human operator are summed up by Kazerooni and Snyder in [24]. The haptic device must be *backdriveable*, the operator must be able to move the system's end effector without any aiding torques applied to the actuators. The joints should have very low friction and *backlash* [22]. The structure must be very rigid, and designed with the minimum number of stiff lightweight components.

The industry leader for haptic hand controllers, the PHANToM [3,4,6,8,16] device (see figure 1.4.1) from SensAble devices, addresses some but not all of the requirements set out in this section. According to [5], the designers of the PHANToM device consider that the most important haptic interactions involve only the positioning and forcing of a virtual point in three dimensions. The PHANToM device provides three active DOFs in the translation of a finger thimble mounted on a universal joint. The thimble allows the user's finger to assume any orientation, but has no active DOFs to provide haptic simulation. The translation stage is designed out of lightweight aluminum tubing with the direct-drive actuators providing for the static counterbalancing. The translation structure therefore allows for the low inertia and low friction, required of a haptic device, leading to a very low free mechanical impedance. However, the lightweight structure of aluminum tubes and the light actuators do not provide a very high level of constrained mechanical impedance. The incorporation of composite materials into the structure of a haptic device has the obvious advantage of simultaneously meeting the design goals of stiffness and light weight while increasing structural damping, as well as providing for imaginative uses of materials to protect sensitive components while acting as primary structural members.

## 2.2 Literature Review of Bonded Joints

The area of study of adhesively bonded joints is very important to the development of the use of composite materials in mechanical structures. The adhesively bonded joint comprises the most effective method of joining composite materials to metals and to other materials. The field of study of the bonded joint includes material selection for both the *adherends*, or the bonded entities, and the *adhesive*, or the glue material that bonds the adherends together. Another area of interest is the stress in the bonded joint, and the effect that the joint geometry has on the stress distribution. It is this second field within the greater study of bonded joints that will be of greatest interest to this work, as the material selection for the adherends and adherent are somewhat more limited by other factors, including availability and compatibility with other materials in the Freedom-7 structure.

There are several design problems associated with adhesively bonded joints that are unlike other types of mechanical joints. In [25], Lees seeks to acquaint engineers unfamiliar to adhesively bonded joints with the particular requirements of this type of fastening. Lees lists seven problem areas with adhesives in joints that must be addressed in the final choice of a joint design:

- adhesives tend to have poor impact behavior
- failure occurs easily for a peel or cleaving force
- material properties are very sensitive to surrounding environmental conditions
- there exists little accurate or useful design data
- there is little data referring to environmental effects
- lack of codes for implementation of standard designs
- poor communication between manufacturers and engineers

Of these seven factors, the most important for the eventual choice of the joint geometry are the first two, those that determine the acceptable loading scenarios of the adhesive joint. Lees goes on to say that the design of the joint should be made such that the adhesive is not exposed to high tensile loads. The preferred load case for a bonded joint

is in shear. For a lap joint, the most important geometry detail would have to be the design of the edge, with bond fillets and tapered adherends contributing greatly to the overall strength of the bonded joint.

The typical joint geometry that Lees examines in [25] is the single lap joint. This can give several good indications about preferred design criterion for other types of bonded joints. First, the maximum load supported by a joint is determined by the shear area of the adhesive. However, as the majority of the adhesives are polymeric, they can be subjected to creep deformation. As such, at least part of the joint should be essentially unstressed for there to be no creep deformation under a static or repeating load. The thickness of the adherends affect the distribution of stresses along the adhesive bond. By reducing the thickness of the adherend near to the edge of the bond area, there is a reduction in the stress concentration near the edge of the bond. However, by reducing the adherend thickness in a single lap joint, there exists the possibility of inducing plastic deformation in the adherends, resulting in peel and tensile stresses applied to the adhesive. Adhesives should, at all times, be free from these peel stresses. At worst, any non-shear stresses experienced by the adhesive should be compressive in nature, and certain design changes in the bond geometry could easily allow this to occur.

The final recommendation by Lees comes in the choice of the adhesive. A ductile adhesive allows for the stress in the joint to be more evenly distributed over the bond area. For this reason, a more ductile adhesive will often result in a stronger bond than the use of a very stiff, brittle adhesive.

In [26], Adams and Harris examine in detail the double lap joint for the bonding of unidirectional carbon fiber reinforced plastic (CFRP) to a steel adherend. The overall recommendation is that the failure in an appropriately designed joint should occur in the adhesive and not in the adherend. Adams and Harris use finite element methods to accurately determine the locations of the stresses in the joint, and the effects that the different geometry parameters have on the joint strength. The thickness of the adhesive, called the *bond line thickness*, is not modified, neither is the thickness of either adherend. The parameters that are examined are: the effects of the bond fillet at the edge of the joint, and the effect of the tapering of the steel adherend. Using the finite element method

to examine both the shear and transverse stresses in the components of the joint, Adams and Harris draw several conclusions about the final design of a bonded joint. First, the peak transverse stresses in the adhesive, which would cause peeling failure in the adhesive, occur near the corner of the steel adherends. They also conclude that the tapering of the steel adherends has very little effect on this undesirable loading of the adhesive when the adhesive material ends abruptly at the edge of the steel adherend. The reduction in the transverse stress in the adhesive is obtained by adding a fillet to the adhesive beyond the steel adherend. Furthermore, the introduction of an internal taper to the steel adherend in combination with the adhesive fillet goes even farther towards reducing the peeling stress in the adhesive material. Finally, the two modes of failure predicted by Adams and Harris with the finite element model shown in [26] is the inter-laminar failure of the CFRP due to the increased transverse stresses in the adhesive close to the material boundary, and cohesive failure in the adhesive due to the concentration of stresses in the adhesive material along the free edge of the adhesive fillet. For a repair situation, the first failure mode is undesirable, as an inter-laminar failure of the CFRP is not easy to see or to fix.

Much of the work associated with the bonding of metal to composites is in the field of composite aircraft wing repair [17, 27, 28]. In [27], Xiong and Raizenne develop an analytical model to determine the strength of a composite/metal patch joint. The overall geometry of the joint considered is that of a composite material patch, adhesively bonded to a metal *substrate*, or base material, for patching and fatigue enhancing of the metal part. The model is capable of taking into account the tapering of the composite patches and calculates the adhesive shear stresses as well as the interface peel stresses between the composite and the adhesive material, and the inter-laminar transverse stresses in the composite. The model takes into account the differential thermal coefficients of expansion of the differing materials that result in thermally induced stresses and is used to predict joint failure.

Xiong and Raizenne draw five conclusions about the joint geometry and material properties for this type of patch joint:

- The most critical area for the fatigue enhancement of the metal substrate under compression is the tapering of the composite patch, which can cause matrix shearing in the patch.

- The predictions of the failure load and mode are heavily dependent on the choice of material properties for the different components of the joints, so material choice and environmental factors are a very important consideration in the design of a composite patch joint.

- The most critical area of the bonded joint for a tensile load case is near the center of the patch, by the edge of the crack in the metal substrate.

- The tapering of the composite patch is useful to reduce the stress in the adhesive near the edge of the patch, but can result in excessive stresses building up in the plies of the composite material near to the adhesive boundary.

- All stresses need to be considered, rather than just the shear area for the adhesive as is common, for proper design of a patch joint.

Further work suggested by the authors is the investigation of the plasticity effects of the bond material, the bending effects on the joint due to load eccentricity and the effect of de-bonding at the extremities of the joint.

In [28], Charalambides et. al. use finite element analysis and physical testing methods to determine failure criteria on environmentally treated patch joints. The main conclusions were that the environmental treatment of the patch joints, each test specimen was immersed in a 50° C water bath for 16 months, had very little effect on the strength of the joint in tension or fatigue. However, the fatigue performance of the patched specimens is much worse than that of the whole, untouched specimens. Joint failure criteria based on maximum critical stress or strain did not produce results consistent with the test specimens. It is their conclusion that this method of predicting the strength of the joint is not adequate due to the edge effects of the finite element mesh, and instead propose a fracture-mechanics based method that yields better results.

In [29], Price and Moulds consider the variables governing the design of a bonded interface between a composite prop-shaft and a metal end fitting for the purpose of transmitting torque. The goals of this design are the reduction of overall weight and cost,

reduction of whirling problems caused by the unbalances generated by mechanical fasteners, the potential elimination of an intermediate bearing, the reduction of noise and vibration and a lower part count for the assembly. Price and Moulds use an analytical program based on continuum mechanics to evaluate the effect of progressively modifying certain joint geometry variables such as adherend wall thickness, bond line thickness and material properties. The program determines the stress distribution along a single lap joint and compares it to an elastic limit for the epoxy material. The effect of dissimilar materials in the joint with a heat cured adhesive is very high, and not recommended. The choice of a cold cured adhesive is beneficial to the joint strength, in that it does not result in high residual stresses in the bond that will aggravate any further loading on the joint. The effect of changing one adherend to GRP (glass reinforced plastic) causes an increase in the stress in the bond near the edge due to the differential deformation of the adherends. To reduce the stress concentration, the thickness of the composite adherend must be increased, to bring the stiffness close to that of the aluminum, and the bond line thickness must be increased to allow for more material in which to distribute the stress. The final joint configuration for the single lap joint is a 5 mm thick aluminum adherend, a 3 mm thick GRP adherend and a 0.2 mm bond line thickness of a two part, ductile, cold cured epoxy. These conclusions are used in the design of the bonded interface between a metal end fitting and a composite tube. The first geometry considered is a simple plug-tube joint, that causes excessively high loads near the end of the plug, while the center of bonded area is unloaded. A bore hole added to the center of the plug, making a partial right cylinder of the insert succeeds in distributing the more of the stress towards the inner part of the bond from the edges, but does not succeed in lowering the stress in the adhesive below the elastic limit everywhere. There still exists a stress concentration near the edges of the bonded area. By tapering the edges of the insert, the stress in the bond can be reduced further near the tapered edge, but it remains high at the other end of the bonded region, near the end of the tube. This stress concentration can be reduced by increasing the bond line thickness, at the risk of causing creep deformation in the bond. The final conclusion by Price and Moulds is that, if it is possible to bond both the inside and the outside of the tube to the metal end fitting, the increase in the overall strength of

the bond is staggering. For any high load scenario, this would be the ideal bonded geometry. They go on to recommend several criteria for a successful joint design:

- A weaker, but ductile adhesive is preferable to stronger yet brittle one. Toughened adhesives will work best.
- The joint design must take into account environmental degradation of the adhesive material properties.
- The *engagement* of the bond, the length of the adhesive bond, should be kept as short as possible if a heat cured adhesive is used. This will reduce the differential expansion stresses in multi-material joints.
- The bond line thickness should as great as possible without allowing the joint to experience creep fatigue.
- There must be no contamination of the composite part by mold release agents.
- Composite surfaces can be prepared by chemical solvent wiping, followed by light abrasion and dust removal. Also, bonding pre-treatments can be used to reduce corrosion and increase the wetting of a surface by the adhesive.

The use of bonded joints in various realms of design has a great potential for growth. The bonded tubular joint has the benefit of reducing parts count by eliminating mechanical fasteners, and by incorporating material that is already available in industry, it has the potential of reducing manufacturing costs as well. There is some difficulty inherent in the bonding process, but with proper jig design in an assembly line production method, these problems are easily surmountable.

## 2.3 Literature Review of Laminate Optimization

One of the most attractive reasons for using composite materials in a robotic structure is the ability to precisely tailor material properties such as stiffness and material damping. The material properties of a part made from a composite material are highly dependent on the sequence that the individual plies are laid-up, and on the orientation of the fibers embedded in the plies. By varying the number of plies in a lay-up, and the fiber orientation, a base material such as unidirectional carbon fibers embedded in an epoxy matrix can exhibit material properties over a very large range. There has been much work done on methods of optimizing the lay-up for various properties, including several linear programming schemes for determining the optimum lay-up for maximizing a particular material property such as damping. This section will seek to overview some of the work already done in implementing composite components for robotic systems, as well as detailing some of the existing lay-up optimization methods.

In [8], Lee et. al. develop an anthropomorphic robot using composite materials to construct the links. They state that the specific stiffness of the links has to be high and the material damping has to be, in any robotic structure, high enough to allow for higher positional accuracy and dynamic performance. The high specific stiffness of the links will allow lighter links to carry the same payload. Hence the actuators can be made correspondingly smaller and less expensive. The high material damping of the links will allow for the damping out of vibrations induced in the structure by high accelerations, and create a greater end point accuracy for the manipulator. Lee et. al. show that the longitudinal stiffness of an *angle ply*, individual plies that are placed with the fiber direction at an angle to the part direction, drops off sharply at  $15^\circ$ , and they choose a lay-up stacking sequence of  $\pm 15^\circ$  for the composite arm with a box-type section. The robot in [8] also used filament wound drive transmission shafts, made from carbon-fiber material. The interfaces between the links and between the drive shafts and the motors were made using bonded end fittings on the composite parts. A choice of bond line thickness of 0.1mm was made, with an engagement length of 100mm for the box-beam

forearm, and 50mm for the drive transmission shafts. The shear area required by the load case expected for the robot would dictate a minimum bond engagement of 20mm, but Lee et. al. suggest that the longer bond lengths make for an easier joining process, and the forearm joint might become unstable in bending if a shorter bond engagement were chosen. The end fittings are machined as a double-lap joint. Both the inside and the outside of the composite parts are bonded to the metal adherends. Hybrid joints are used for the pivots on the composite forearm. The joints consist of a metal plate bonded on the outside of the box section, with a bolted reinforcing plate on the inside. Such a joint can be expected to perform well in shear as well as in tension and compression. The composite arm was compared to an equivalent steel arm for a variety of static and dynamic criteria. The fundamental natural frequency of the composite arm was more than twice that of the steel arm, and the inherent damping ratio was seven times as much for the composite arm than for the steel arm. The mass of the composite arm was less than one quarter that of the steel arm. Overall, the inclusion of the composite materials in the robotic structure, while involving some complicated bonding techniques, seems to be very advantageous to the dynamic performance of the device.

For accurate control of robots including composite materials in the structure, accurate modeling of the dynamic characteristics of the composite material has to be performed. In [30], Gordaninejad et. al. take as a base assumption for the dynamic model of a composite robot arm that the rigid and flexible motions of the arm must be coupled. The basis of this assumption is that, for modern high speed robot manipulators, the vibrations induced in the structure are not so small as to be negligible in the dynamic modeling of the robot structure, as is traditionally the case for large, low speed manipulators. By applying their model of coupled dynamic terms to a simulated composite box beam made of angle plies, they show that an increase in deflection for angle plies up to about  $15^\circ$  of ply angle is negligible compared to the unidirectional plies (the highest obtainable specific stiffness). However, the maximum normal bending stress in the part shows a minimum for the angle plies at  $15^\circ$ . This suggests a reasonable first assumption for an ideal ply angle for the material of the box beam. Gordaninejad et. al. show conclusively that the coupling of the dynamic terms in the calculation of end point

deflection is required for accurate modeling of a robotic system. In [31], Gordaninejad et al. develop a similar coupled dynamic modeling of a revolute-prismatic beam made of composite materials.

To design for specific material characteristics such as material damping, a method for predicting the value of the property is required. Ni and Adams, in [9], attempt to formulate a predictive damping equation based on the strain energy in a symmetrically laminated composite beam vibrating at a natural frequency in free flexure. The damping calculations are functions of three measured parameters of the base material; the longitudinal, transverse and shear specific damping capacity. The values for the three specific damping coefficients for the laminated beam are calculated as sums of the material properties and orientations over the thickness of the laminates. The results of the theoretical calculations are very close to the values that Ni and Adams measured for the free flexural damping of the symmetrically laminated beams.

In [13], Adams and Bacon also attempt to evaluate both theoretically and experimentally the damping associated with a composite material lay-up. Specifically, they evaluate the effect of the fiber orientation and the laminate geometry on the damping produced in a composite specimen. In general, the damping in an angle ply laminate reaches its maximum at a fiber orientation of  $35^\circ$ , and the dominant dissipation term is the shear stress term. The majority of the damping that can be associated with a composite part is due to the resin system used, more so than the fibers. This is shown by the increase in the damping for a decrease in the fiber modulus. The lower the fiber modulus, the greater the strain energy in the matrix material, and the higher the damping will be for the laminate.

The same authors as [13] suggest in [10] some methods for increasing the damping in a multi-layer, unidirectional laminate specimen. Adams and Bacon show that the presence of imperfections in a laminate, such as resin poor areas, voids or even small cracks can lead to greater values of damping in the laminate. They also say that the majority of the damping occurs with the strain energy in the matrix in the longitudinal, or fiber, direction. The strain energy stored in the matrix material as a dilation will contribute little to the overall damping of the laminate. Finally, as the modulus of the

fibers is reduced, the energy stored in the matrix increases. The damping associated with the shear deformation of an off-axis laminate is essentially unchanged, but the longitudinal damping increases. Therefore the overall damping associated with the laminate will show an increase. While the presence of voids and cracks can be very detrimental to the life of a laminate, a similar effect of increasing the laminate damping beyond the predicted levels can be obtained by a slight deviation in the straightness of the fibers during manufacturing. For parts made from unidirectional material, this could be very helpful in improving the dynamic characteristics of the composite part.

Extensive knowledge of the required performance criterion for any manipulator is needed to be able to accurately specify the material parameters that will be obtained with the optimization of the laminate. In [11], Lee et. al. construct a SCARA type direct drive robot with composite material linkages. A SCARA robot is a sturdy, pick-and place robot. Two revolute linkages form a two dimensional planar workspace, through which a prismatic linkage can be moved in order to perform the required tasks. The lay-up of the composite materials was determined by the static deflection calculations of the end effector. The outer arm of the SCARA robot is subjected to very little torsion loads, so a filament winding angle boundary of between  $5^\circ$  and  $15^\circ$  was chosen for this linkage. The end effector deflection was calculated over the workspace joint angles for a range of winding angles for the inner arm. The winding angles chosen were  $20^\circ$  for the inner arm and  $10^\circ$  for the outer arm, while the maximum deflection of the end effector over the entire workspace did not exceed 30 microns for 10 N of payload. Only the stiffness material parameter was chosen for the optimization of these parts, and no considerations other than the static load deflection were taken into account.

In [14], Sung and Thompson propose a systematic method for optimizing the lay-up of a robotic structure for maximum performance benefits. They show the influence that material properties of a laminate can have over the performance of a robot with a simple schematic. The fiber orientations and characteristics combined with the matrix characteristics, lay-up and stacking sequence have a direct effect on the density, the strength and the damping of the material. The material density combined with the link geometry determines the mass of the structure. The strength of the material and the link

geometry determine the stiffness of the structure. However, the material damping is the only factor that contributes to the structural damping if the articulated joints are considered ideal. Finally, the mass and stiffness of the structure combined with the damping properties of the material will determine the accuracy, the cycle time, the workspace, payload and repeatability of the robotic manipulator. In many cases, the link geometry will be fixed for reasons of interference, or drive system routing. For this reason, it becomes necessary to provide a means to optimize all three material properties, density, strength and damping, simultaneously to obtain a fully optimized robotic structure. The linear programming techniques used in this article are designed to optimize the properties of thin laminate beams, that will subsequently be bonded together to form a box-section structure. The optimization routine determines the lay-up that obtains the maximum material damping subjected to certain constraints on the fiber angle, maximum laminate thickness and hence link weight, fiber volume fraction and bending stiffness terms for the Cartesian directions  $x$  and  $z$  (the axis of the link is considered to be the  $y$  direction). The laminate geometry obtained from the optimizing routine showed significantly improved damping over the arbitrarily chosen initial design for the composite part.

The optimization routine proposed in [14] is further refined by Sung and Shyl in [12] to determine the optimum lay-up for a complete box-section, rather than a box-section made from bonded laminate plates. The proposed optimized box beam could be manufacture by bag molding around an internal mold as a single part. Sung and Shyl propose several illustrative examples to show the flexibility of the optimization routine. The first is a simple serial manipulator, where the magnitude of the endpoint vibration is to be minimized. The results of the optimization routine show that the wall thickness of the laminates increase to the maximum value permitted by the constraints as the routine is dependent more upon the stiffness of the links than the overall link weight. The second example, using the same manipulator, seeks to have the shortest settling time for a prescribed maneuver. The same constraints on the box-section were imposed as for the first example, but the optimum lay-up was quite different. For the shortest settling time, the fiber-volume fraction tended to be minimized, as the damping of the material was

heavily dependent on the matrix content of the lay-up. The potential for optimizing the material properties is extensive. The gains made in these two simple examples are testimony to the importance of a careful choice of all the material characteristics for optimizing a laminate. However, detailed criterion are required for a proper optimization to be possible. The same manipulator, subjected to two slightly different optimization criteria returned two very different lay-ups. The increase in the matrix volume fraction for the second optimization of the manipulator would be contrary to the requirements of the first optimization of the manipulator. Also, neither case resulted in a minimum weight for the manipulator links. Both optimizations sacrificed link weight to the benefit of the material properties of the laminate.

Unfortunately, the detailed determination of the performance criteria for a haptic device is beyond the scope of this work. Subsequently, a full optimization of the laminate for the box-section linkages cannot be performed. As a preliminary optimization technique, an iterative finite element modeling of the lay-up in question will be used instead of the more rigorous non-linear programming covered in this section.

## ***3. Design of Bonded Tubes***

### **3.1 Introduction**

Small diameter commercially available composite tubing was considered as a basis for the construction of the linkages of the translation stage because it permits several interesting options. For an undetermined load scenario, such as that found in the links of the translation stage of the haptic controller, the most efficient cross section for dealing with multi-axis loads is circular. Also, relatively inexpensive commercially available cylindrical tubes made from carbon-fiber material present a viable alternative to the heavy machining costs associated with complex aluminum parts.

### **3.2 Material Survey of Composite Tubes**

An extensive search was made to find adequate material in the form of small diameter carbon-fiber tubes readily available from the commercial sector. The choice of pultruded carbon-fiber tubes was made based on the design goals for the Freedom-7 project: decrease the link weight and increase the link stiffness. Unidirectional carbon-fiber tubing provides the highest stiffness to weight ratio for any material. However, it turned out to be no easy task to find this material on the market. Pultrusion of carbon fibers requires special dies and very expensive setups. The epoxy matrix material commonly used in conjunction with carbon fibers does not lend itself easily to the pulltrusion process, as the cure time for this material is normally quite long.

Several market sectors were targeted as potential suppliers: the construction industry, the aeronautics industry and the sports equipment industry. It was discovered that, in the construction industry, the majority of the composite material tubing is made of glass fibers. The diameter of this tubing was also too large to be useful in the translation stage of the Freedom-7. A search in the aeronautics industry turned up several candidates for the link material. The most promising came from the Aerospace Composite Products [32] a company in California. The material obtained from them was originally intended for the construction of spars and control surface push rods in model airplanes. The tubes were part carbon fiber, part glass fiber material. There was one type of tubing made of woven carbon fiber material, the RH-2. The sports industry had many more material options available. The hunting industry manufactures carbon fiber arrows for high tech



*Figure 3.2.1 - High-tech Arrow Shafts*

sport hunters, and composite ski poles can be found all over the market. Three samples of arrows were obtained from various hunting stores in the Montreal area. These are shown in figure 3.2.1. The top arrow, an all aluminum shaft, is the XX75, the middle shaft is the all-composite unidirectional shaft, the V-Max, and the bottom is the Easton ACC, an aluminum shaft surrounded by a woven carbon fiber sheath. Finally, the cross country ski pole industry turned up the most promising material in the form of unidirectional pultruded carbon-fiber polyester ski pole blanks, bought from Top Sports [33], a sports equipment manufacturer in Montreal.

In order to determine the best candidate for the link material from all the available tubes, a three-point bend test was performed to determine the effective longitudinal modulus of the material. The effective modulus was divided by the density of the tube to

determine the effective specific longitudinal modulus of the tube. This was done according to the following calculations:

$$EI_{eff} = \frac{P \cdot L^3}{48 \cdot y_{max}}$$

$$EI_s = \frac{EI_{eff}}{\rho}$$

- $EI_{eff}$  is the effective longitudinal modulus times the moment of inertia of the tube (flexural stiffness)
- $P$  is the weight suspended at the middle of the three-point bend setup
- $L$  is the length between the two supports of the three-point bend setup
- $y_{max}$  is the maximum deflection at the center of the beam measured by a dial gauge
- $\rho$  is the density of the tube material
- $EI_s$  is the effective specific longitudinal modulus times the moment of inertia of the tube (specific flexural stiffness)

A summary of the results of the three-point bending tests on the different tubes can be found in table 3.2.1. The desired property for the optimization of the structure is the maximum  $EI_s$ , as that determines the flexurally stiffest tube material and geometry for the lightest weight. The ski pole material, the unidirectional carbon-fiber polyester, is therefore the preferred material for the construction of the stage 3 linkage.

*Table 3.2.1 - Summary of Composite Tube Properties*

	Length	D <sub>i</sub>	D <sub>o</sub>	Mass	EL <sub>eff</sub>	EL <sub>c</sub>
TU-04	0.206	0.0105	0.0129	0.0165	$2.689 \times 10^{-2}$	$1.481 \times 10^{-3}$
RH-2	0.768	0.006	0.008	0.0218	$1.247 \times 10^{-2}$	$9.662 \times 10^{-6}$
Vmax	0.838	0.00384	0.00644	0.0246	$9.278 \times 10^{-3}$	$6.635 \times 10^{-6}$
ACC	0.870	0.00618	0.0076	0.0203	$8.036 \times 10^{-3}$	$5.293 \times 10^{-6}$
TU-06	0.287	0.0058	0.0071	0.0059	$3.997 \times 10^{-3}$	$2.561 \times 10^{-6}$
XX75	0.850	0.00864	0.00956	0.0294	$7.087 \times 10^{-3}$	$2.531 \times 10^{-6}$
TU-07	0.148	0.00384	0.0074	0.0152	$7.145 \times 10^{-3}$	$2.186 \times 10^{-6}$

### 3.3 Geometry and Parameter Variation of Bonded Inserts

The composite tubes require bonded metal inserts to allow for bearing fittings. A choice was made to use exterior cylindrical fittings. The tube cross section did not allow for the more aesthetic internal fittings due to small inner tube diameters. The external fittings were easier to implement.

As shown previously, this type of bonded joint has been studied for torsion loading, such as is found in composite prop-shaft design [29]. However, little analysis had been done on this type of joint for three-dimensional bending and tensile loads that are consistent with the hand controller load cases.

For the model considered in this work, several parameters were chosen, and varied in different finite element models to gauge their effect on the concentration of principal stresses in the bond material. Figure 3.3.1 shows a schematic diagram of the bonded geometry, with the parameters  $a$ ,  $e$ , and  $l$  are, respectively, the adherend thickness, the axial engagement and the bond line thickness. In each model, the diameter of the composite tube, the adhesive fillet and the fillet on the inside adherend surface remain constant.

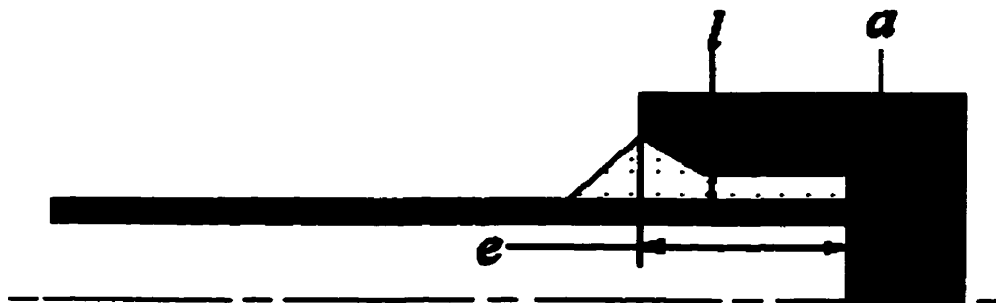


*Figure 3.3.1 - Bond Geometry for Parameter Variation*

### 3.4 Axisymmetric Finite Element Models

The finite element models used to determine the effects of the geometry parameters on the bond strength were constructed using axisymmetric elements. The first iteration of the testing was done using meshes similar to that seen in figure 3.4.1. The

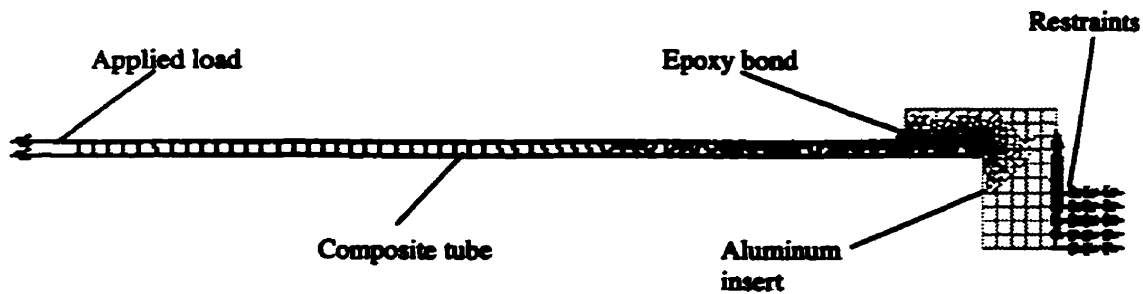


*Figure 3.4.1 - Axisymmetric Finite Element Model of Bonded Geometry*

elements composing the composite tube are of an orthotropic material having the properties of unidirectional carbon fiber material [34]. The material axis for these elements was set to be the same as the axial direction of the tube. The material properties of the isotropic epoxy bond were determined from literature. The elements of the metallic insert were assigned isotropic material properties consistent with aluminum-6061 [35].

The elements of the tube are joined (they have coincident nodes) with the elements of the epoxy bond along the bottom face (CFB in figure 3.3.2). The elements of epoxy and aluminum are connected along the entire interface for test 1 and 2 for each model, and the bond DAB in figure 5.3.2 is broken in tests #.3 and #.4 in each model. This discontinuity is consistent with a bond that is going to be loaded purely in shear. As the results will show in the next sections, the break is also consistent with a potential first failure mode.

**Table 3.4.1 - Parameter Variation for Axisymmetric Finite Element Models**

Test Number	$a$ (mm)	$l$ (mm)	$e$ (mm)
Tests 1.1-1.4	2.0	0.25	5.0
Tests 2.1-2.4	0.5	0.25	5.0
Tests 3.1-3.4	4.0	0.25	5.0
Tests 4.1-4.4	2.0	1.0	5.0
Tests 5.1-5.4	2.0	0.05	5.0
Tests 6.1-6.4	2.0	0.25	10.0
Tests 7.1-7.4	2.0	0.25	3.0

A total of seven finite element models were constructed to analyze the effect of the different parameters on the maximum principal stress in the bond. Each of the seven models had four tests performed. The first and fourth test were without the bond fillet at the extreme end of the composite tube (line FB in figure 3.4.2). The second and third tests both have this fillet. As mentioned before, the first and second tests have a bond between the aluminum and the epoxy on line DAB in figure 3.4.2 where in the third and fourth tests, this bond has been broken. Table 3.4.1 shows the test numbers and the parameter variations for each model. Tests 1.1-1.4 are the arbitrarily chosen base tests. Tests 2.1-2.4 and 3.1-3.4 vary the adherend thickness  $a$  from 0.5 mm to 4.0 mm. Tests

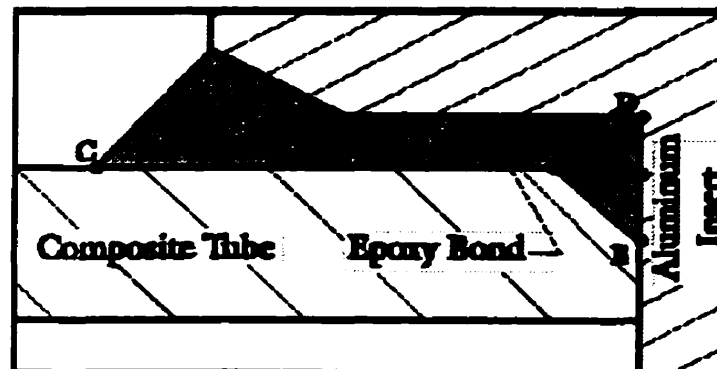


**Figure 3.4.2 - Reference Locations on Bond Geometry**

4.1-4.4 and 5.1-5.4 vary the bond line thickness  $l$  from 0.05 mm to 1.0 mm. The last two sets of tests, namely 6.1-6.4 and 7.1-7.4, vary the axial engagement  $e$  from 3.0 mm to 10 mm.

### 3.5 Results of Parameter Variation

To properly interpret the results that will be shown in this section, the purpose of the optimization must be made clear. As was stated previously, the design goal of the Freedom-7 is to provide a hand controller structure that will minimize the link weight and inertia felt by the operator, while at the same time meeting all the design criterion such as minimum required strength and lowest resonant natural frequency. To obtain this goal, the links, and subsequently the bonded inserts, have to be designed with the following purpose in mind: minimize the weight and material without sacrificing minimum strength requirements. In our case, if removing material from the interface increases the maximum principal stress in the bond, then this is a desirable effect, so long as the final geometry is able to withstand a minimum required load. However, if increasing the material in the bonded interface (such as increasing bond line thickness and adherend thickness) increases the maximum principal stress in the bond, then this becomes a very undesirable effect, countering both design goals of minimum weight and minimum required strength. Figure 3.5.1 shows the variation of the peak maximum principal stress with respect to the variation of  $a$ , the adherend wall thickness. The maximum principal stress concentration in the epoxy bond decreases with an increase in the adherend wall thickness. Figure 3.5.2 shows the variation of the peak maximum principal stress with the variation of  $e$ , the axial engagement of the tube into the metal insert. The stress concentration decreases with the increase of the axial engagement of the bonded entities. Figure 3.5.3 shows the variation of the peak maximum principal stress in the epoxy bond material with the variation of the bond line thickness  $l$ . There is a minimum for the peak principal stress in the bond material near a bond line thickness of 0.25 mm.

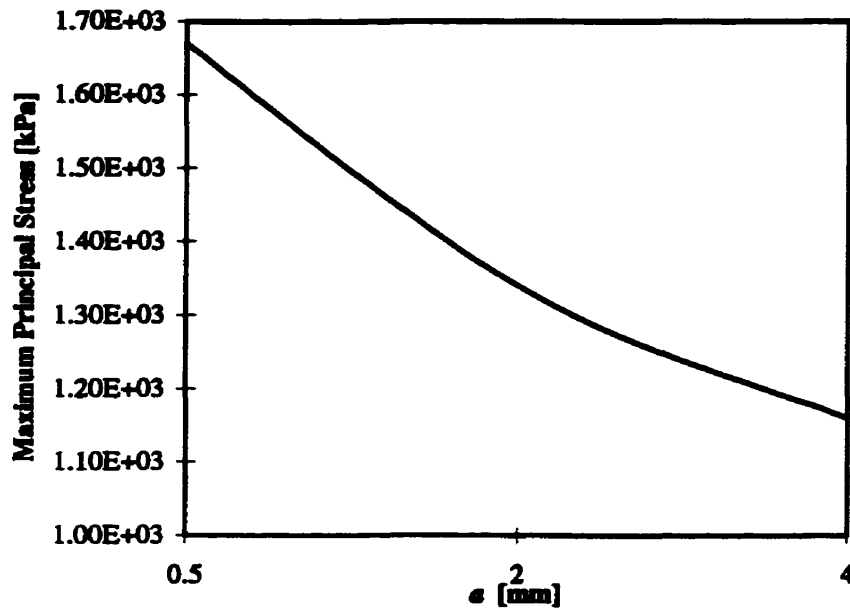


*Figure 3.5.1- Variation of Peak Principal Stress with Adherend Wall Thickness*

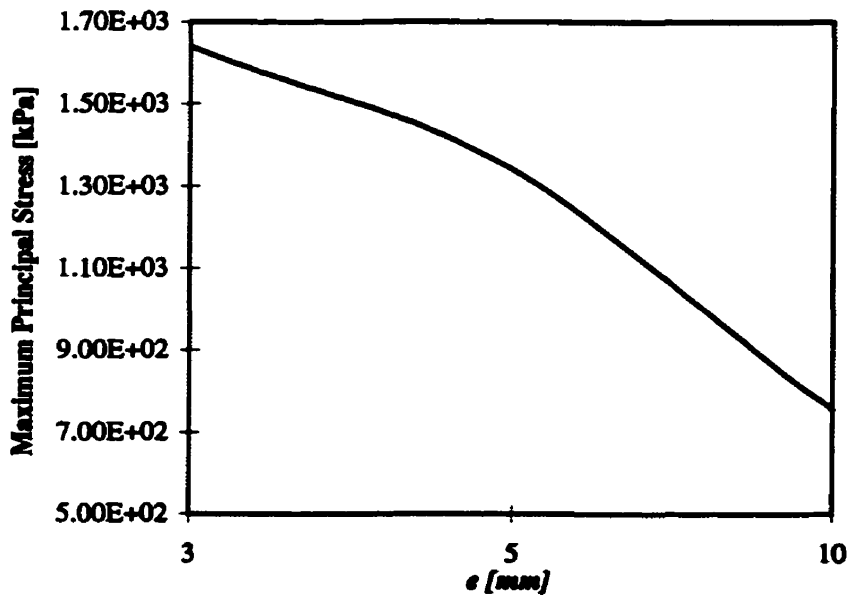


*Figure 3.5.2- Variation of Peak Principal Stress with Axial Engagement*

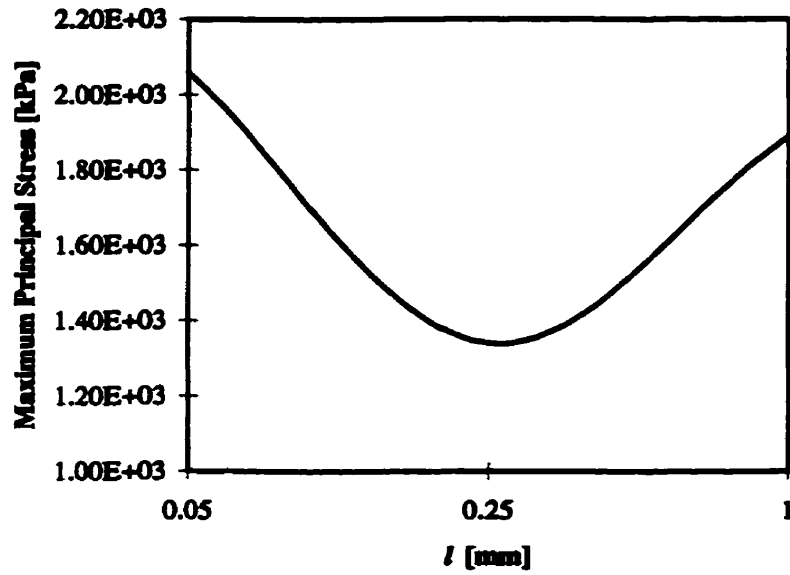


*Figure 3.5.3- Variation of Peak Principal Stress due to Bond Line Thickness*

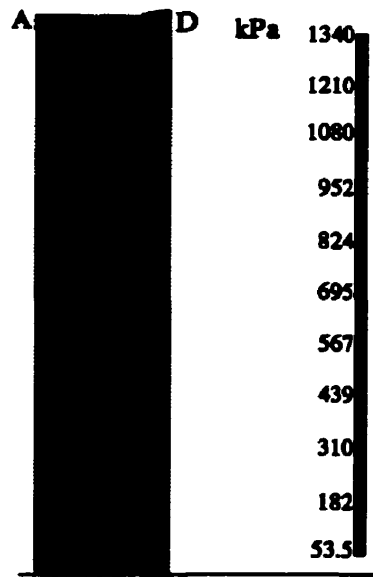


*Figure 3.5.4 - Maximum Principal Stress Contours in Epoxy Material for Test 1.4 (Bond AD Broken)*

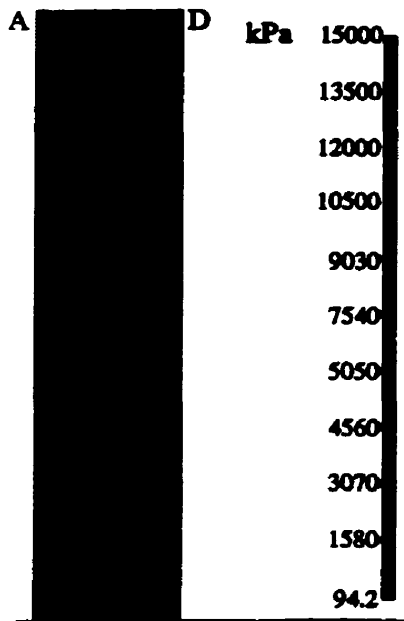


*Figure 3.5.5 - Maximum Principal Stress Contours in Epoxy Material for Test 1.1 (Bond AD Exists)*

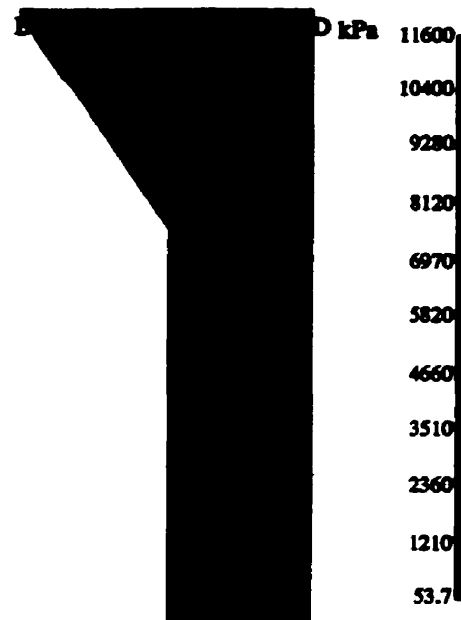


*Figure 3.5.6 - Maximum Principal Stress Contours in Epoxy Material with Epoxy Fillet for Test 1.3 (Bond BAD Exists)*

Figures 3.5.4 and 3.5.5 show the effect of breaking the bond along the DA interface. The stresses become much more distributed throughout the bond line thickness, and the peak principal stress is also reduced. This situation is advantageous, as more of the bond is now loaded. As well, risk of delamination in the carbon fiber material is reduced, as the stress concentration is moved to the region of the bond in contact with the metal. The effect of adding a fillet in the composite tube is fairly small. Figure 3.5.6 shows the stress contours of the 1.2 test, where a bond exists between the epoxy and the metal along DAB and a fillet is added in the composite tube to increase the bond line near the end of the joint (FB in figure 3.4.2). There is a large stress concentration at point B on figure 3.5.6 and there is little decrease in the maximum principal stress between test 1.1 and 1.2. The difference in the bond strength due to the fillet is considered negligible and, for manufacturing reasons, it will be left out of the final geometry. In general, the effect of breaking the bond along line DB in figure 3.5.5 has the effect of reducing the large stress concentration in the epoxy at either A or B depending on whether the epoxy fillet exists or not.

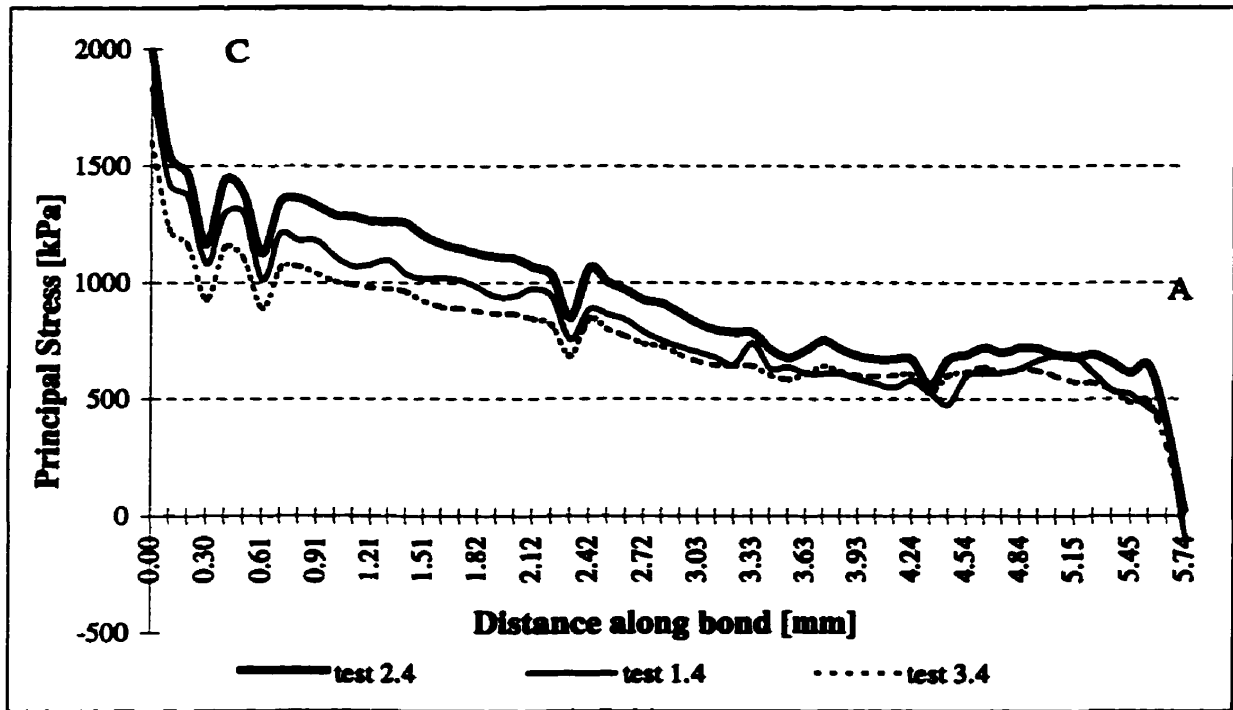


Figure 3.5.7 - Variation of Principal Stress Along Bond due to Adherend Thickness (a)

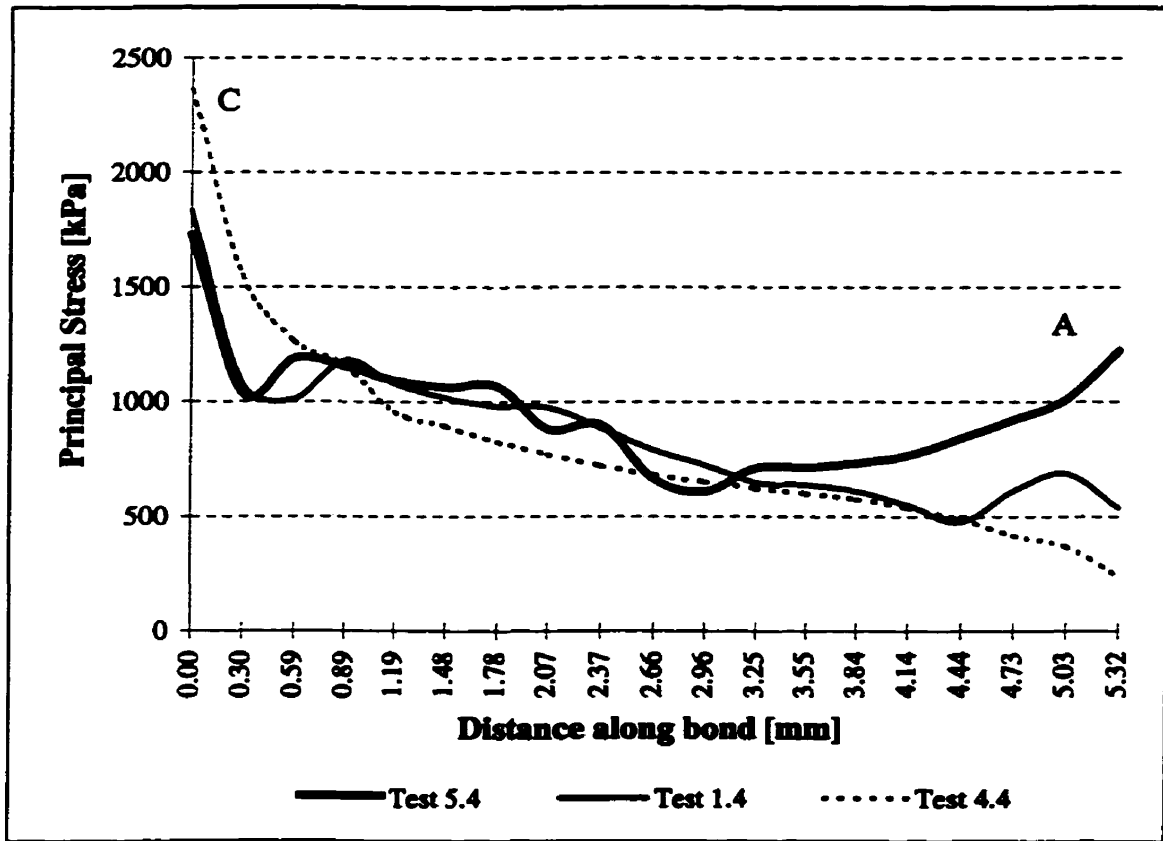


Figure 3.5.8 - Variation of Principal Stress Along Bond due to Bond Line Thickness (l)

The variation of the principle stress with the parameters  $a$  and  $l$  is shown in figures 3.5.7 and 3.5.8 respectively. Figure 3.5.7 shows the variation of the principal stress in the bond along the surface of the carbon fiber tube (AC) due to the variation of the adherend thickness,  $a$ . As the adherend decreases in thickness, the maximum principal stress in the bond increases. Therefore, according to the design goals stated previously, to optimize the bond for this geometry parameter involves decreasing the adherend thickness to the limit of structural strength. The optimized model will use a value of  $a$  of 1.0 mm. Figure 3.5.7 shows that the maximum principal stresses in the bond are only weakly dependent on  $a$ .

Figure 3.5.8 shows the variation of the maximum principal stress due to bond line thickness,  $l$ . As the bond line thickness increases, stress is distributed more evenly over the bond. The optimum line thickness should be somewhere in between 0.05 mm and 0.25 mm. According to the literature [36], the bond line thickness should remain between 0.01 and 0.1 mm for stability reasons. As such, a bond line thickness of 0.1 mm was chosen for the optimized model.

Obviously, in the interest of weight savings on the part, the axial engagement should be as short as possible. This factor will not be as critical in a purely tensile application. However, as the stage three linkage can be subjected to high transverse bending loads, the length of the axial engagement will be critical in the resulting strength of the bonded joint [8]. This factor will become very apparent later on during the testing phase of the optimized joint. As such, the value of  $e$  chosen for the optimized bond geometry is 10.0 mm.

Appendix A shows the maximum principle stress contours for the whole range of parameter variations. A.1 shows the maximum principal stress contours for the epoxy material of the base instance, namely test 1.4. A.2 shows the effect of the bond between the aluminum and the epoxy along DB in figure 3.4.2 on the entire bond region, showing the maximum principal stress contours in the epoxy material for test 1.1. A.3 shows the effect of the adherend thickness on the maximum principal stress contours and includes the stress contours for the epoxy material for tests 2.4 and 3.4. A.4 shows the effect of

the bond line thickness on the maximum principal and includes the stress contours for the epoxy material for tests 5.4 and 4.4. Finally, A.5 shows the effect of the axial engagement on the maximum principal stress contours, and includes the stress contours for the epoxy material for tests 6.4 and 7.4.

Thus for optimum weight and adequate stiffness, the summary of the results of the study are:

- make  $a$  as small as possible within the structural stability
- make  $e$  as short as possible within the structural stability
- make  $l$  such that it lies between 0.05 and 0.25 mm

### 3.6 Three Dimensional Finite Element Model

The structure of the translation stage experiences two dimensional bending loads as well as loads in tension and compression. Therefore, we can not assume the bond geometry is properly designed without subjecting it to off axis loads. Accordingly, a three dimensional finite element model was constructed to evaluate the design safety of the optimized bond geometry. Values for  $a$ ,  $e$ , and  $l$ , were obtained by the axisymmetric parameter variation performed in the previous section: 1.0 mm, 10.0 mm, and 0.1 mm respectively. Because of symmetry, only one half of the tube / insert was modeled, significantly reducing computation time. The three dimensional finite element model can be seen in figure 3.6.1. The blue composite tube elements are thin shell elements, with

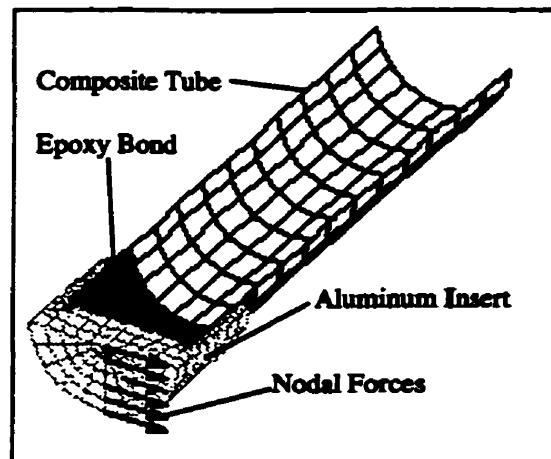


*Figure 3.6.1 - Three Dimensional Finite Element Model of Bonded Tube Geometry*

the material properties of unidirectional carbon fiber material. The yellow aluminum elements are linear brick elements and have the material properties of isotropic aluminum. The light blue epoxy elements have material properties of isotropic epoxy and are also linear brick elements. The load is distributed over seven nodes on the face of the aluminum insert, and the boundary conditions are such that the end of the tube is clamped while the symmetric surface is restricted to move along the plane of symmetry.

According to [3], the typical maximum load applicable by a finger is 40 N. If we consider a hand grasping the end effector, more than one finger will be in a position to apply force to the Freedom-7 structure. Thus, it is reasonable to assume a worst load case scenario of 80 N on the end effector. This load is obviously beyond the limits of the actuators, but can be obtained when the structure encounters a physical limit stop near the edge of the workspace. For the stage 3 linkage, the moment arm is 150 mm. The total bending moment on the interface is therefore  $12 \times 10^3$  N-mm. The offset for the end of the aluminum insert is 10 mm, therefore, the required force for the worst load case scenario, distributed over seven nodes, is 85.714 N per node. The units for IDEAS-Mater's Series V. 2.0 [37] is mN, therefore, the load applied to each node is 85 714 mN.

Figures 3.6.2, 3.6.3 and 3.6.4 show the maximum principal stress contours in the various components of the bond geometry. Figure 3.6.2 shows the maximum principal stress contours in the composite tube, with the bonded region outlined. Figure 3.6.3 shows the maximum principal stress contours on the bonded face of the aluminum insert. Figure 3.6.4 shows the maximum principal stress contours in the epoxy bond material. The locations for the stress concentrations are not in the same place on the bond for each of the entities. The maximum stress concentration for the composite tube occurs near the edge of the bonded region. The fibers in this area are in tension due to the bending load. The stress concentration for the aluminum end fitting, however, seems to be an artifact of the mesh, as it does not correspond to any real scenario. The peak principal stress in the epoxy material is on the free face of the bond fillet, which is one of the failure modes that was observed in [26]. As the stress is not concentrated near the interface with the composite tube, we can assume that there will be no delamination in the composite tube due to the bond.

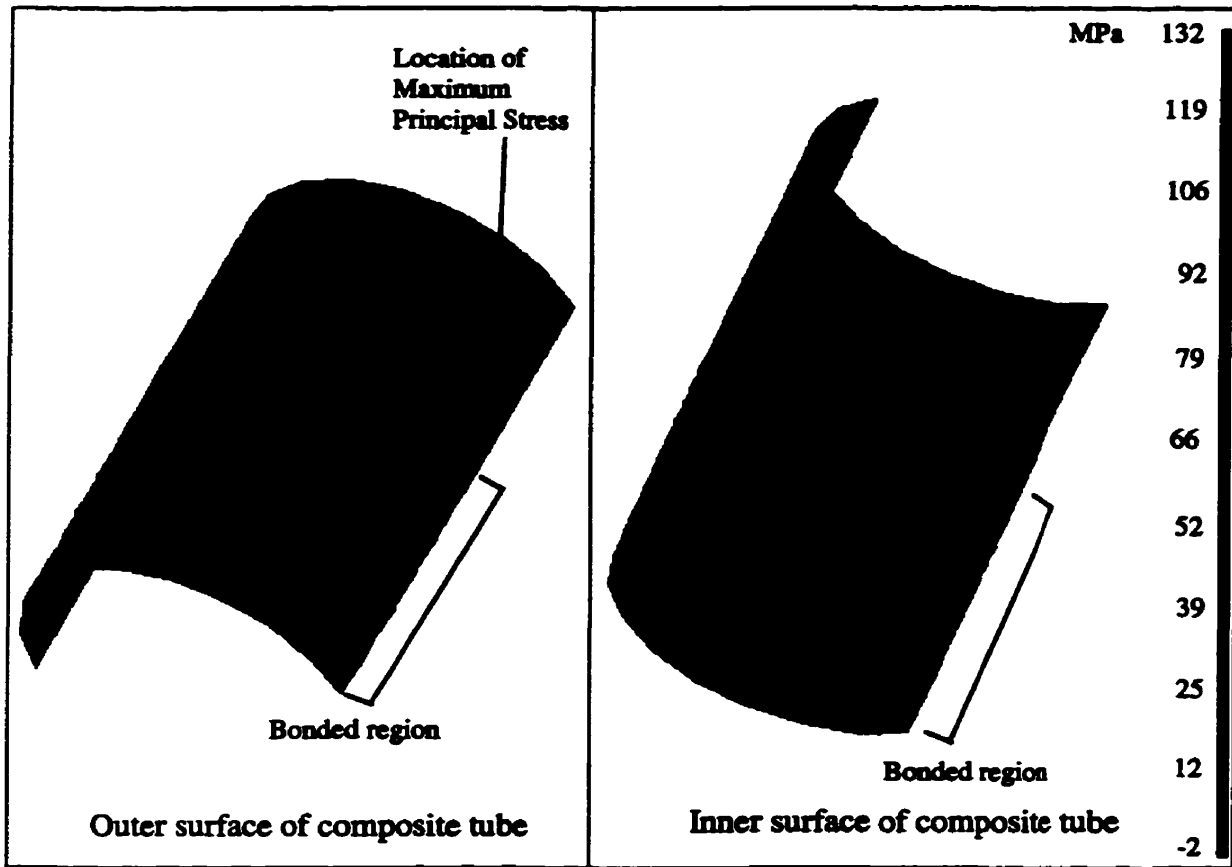


*Figure 3.6.2 - Maximum Principal Stress Contours in Composite Tube Close to Bonded Region*

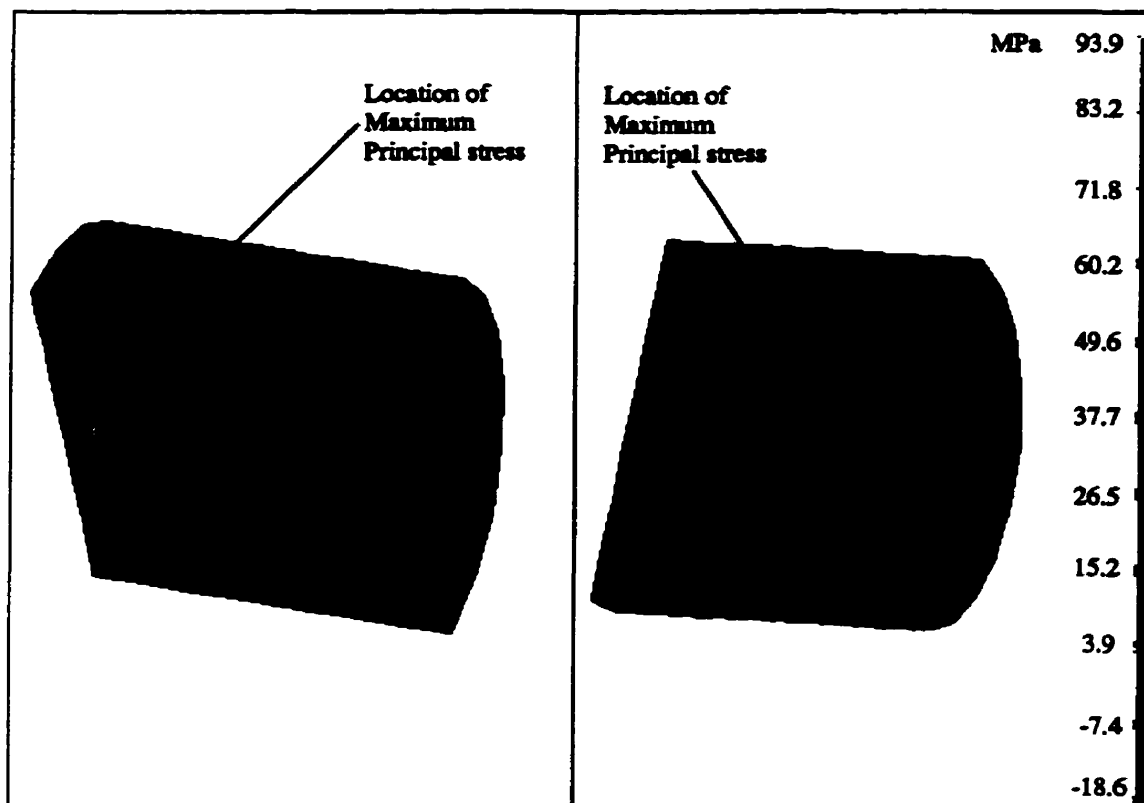


*Figure 3.6.3 - Maximum Principal Stress Contours for Bonded Face of Aluminum Insert*

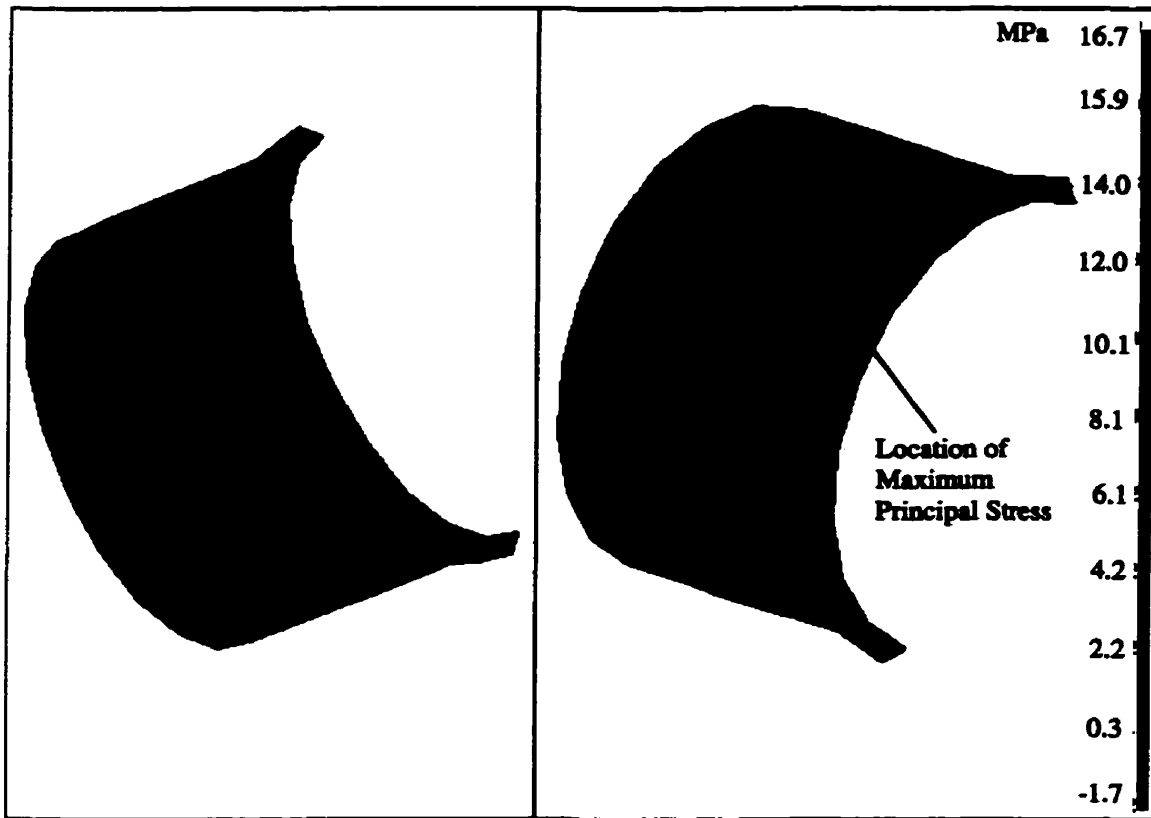


*Figure 3.6.4 - Maximum Principal Stress Contours in Epoxy Bond Material*

In figure 3.6.2, the maximum stress in the composite tube occurs in tension near the end of the bonded region. This stress concentration is due to the transfer of the tension stresses generated by the bending of the tube from the aluminum and epoxy to the composite tube, and is unavoidable. However, the stresses begin before the end of the epoxy bond, which contributes to a gradual transfer of the load and reduces the overall stress concentration. This gradual transfer is the reason for designing the metal end fitting with a fillet, and for creating a fillet with the epoxy material. The composite tube is not in danger of failing from this peak principal stress.

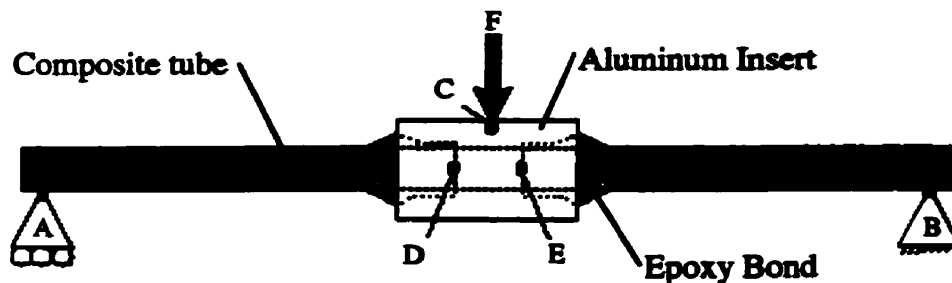
Figure 3.6.3 shows the inner surface of the aluminum insert. The peak principal stress is located right at the corner of the metal insert. This stress at this point is far below the yield stress of aluminum, so there is no danger of failure in this part.

Figure 3.6.4 shows the epoxy material. The maximum principal stress is located near the top of the fillet on the metal insert. The maximum principal stress is 16.7 MPa. The value of the stress at this point is close to the yield strength of the epoxy. The yield strength of the epoxy is 20.3 MPa [38]. The factor of safety for the optimized bond subjected to the worst case load scenario described above is therefore 1.22. The actual hand load on the end effector could be 1.22 times greater, or 97.2 N, before a failure would occur at the bonded joint. It would not be advisable to try to further optimize the geometry of the bond, as this would jeopardize the safety of the bond for the postulated worst case loading scenario. We can assume that the bond, as it stands, is optimized for this application.

## 4. Bonding Tests

### 4.1 Three-Point Bend Test

It was proposed to perform a three-point bend test to evaluate the three



*Figure 4.1.1 - Sketch of three-point bend test setup*

dimensional finite element model and the chosen optimal configuration of the bonded interface. The three-point bend test was performed according to Figure 4.1.1. A three-point bend test, rather than a four-point bend test, was chosen for fear that the composite material might fail locally due to the applied pressure. The three-point fixture above allows loading on the aluminum insert. The aluminum insert required a double bond configuration, with the load applied in the center, to allow for the maximum bending load applied during the test to be in the region of interest, and to allow for the test to be performed in a symmetric fashion.

The test was performed on the MTS machine [39]. Four samples were used (figure 4.1.2), each with a different bond geometry. The construction of the samples went as follows:

1. Aluminum inserts were machined with two bond interfaces according to the dimensions shown in table 4.1.1. (referenced dimensions are according to figure 3.2.1)
2. Unidirectional carbon-fiber / polyester tubing was cut into eight 100mm lengths.
3. The inside bonding surface of the aluminum insert was roughened with a small file to increase the shearing strength of the bond.

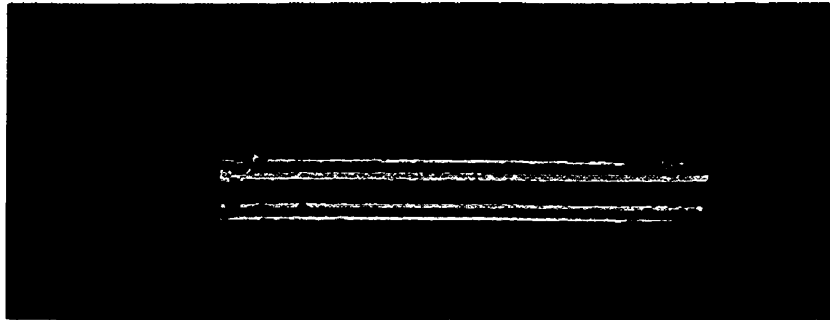


*Figure 4.1.2 - Three-point bending test specimen*

4. As suggested in [36], the surface of the composite tube that was to be bonded was also sanded with emery cloth to remove any release agent and extra resin that might have been present from the manufacturing process.
5. The aluminum inserts were clamped in such a way as to be vertical and coaxial with the composite tubes.
6. The bond volume was fully filled with Adbond epoxy [40] and a bond fillet was shaped by hand to approximately 45 degrees.
7. The set-up was left 24 hours at room temperature to cure.

Test #	$l$	$e$	$a$
1	0.1	10.0	1.0
2	0.1	10.0	3.0
3	0.5	10.0	1.0
4	0.1	5.0	1.0

Figure 4.1.3- Variation of dimensions for three point bending tests

The samples were mounted in a three-point testing jig that allowed for simply supported conditions. The load  $F$  was applied by a cylindrical applicator on a small flat surface machined into the aluminum inserts at C on figure 4.1.1 to assure a point load condition. The horizontal distances AC and CB are the

same at 100 mm. The horizontal distances DC and DE are also the same at 10 mm. The displacement rate for the position control was chosen to be 0.095 mm/sec, resulting in a quasi-static loading case.

## 4.2 Calculations for Bending Moment Load Case

The ideal shear force ( $V$ ) and bending moment ( $M$ ) diagram for the simply

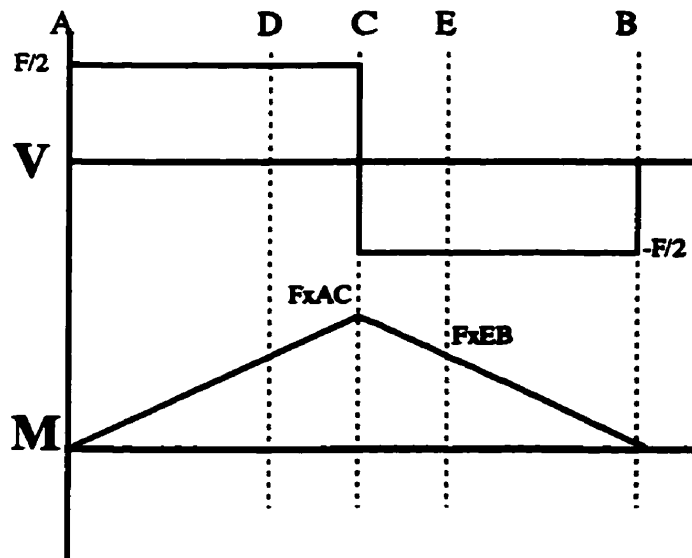


Figure 4.2.1- Shear and bending moment diagrams for three-point bending tests

supported three-point bend test is shown in figure 4.2.1. The maximum bending moment on the sample is at point C. The maximum bending moment on the bonded region is at

points D and E. First failure will occur here due to the tension caused by the bending of the sample. Due to the non-homogeneous nature of the test samples, the pure bending formula for the calculation of the resultant stress in the sample does not hold. The individual components have different moduli of elasticity and different bending radii for the same load. The ideal calculations for the stress in a prismatic beam under pure bending require that the radius of curvature for the beam is constant and that the cross sections of the beam remain undeformed and perpendicular to the longitudinal axis, an assumption that does not hold here.

To provide a design criterion for the bonded geometry, the actual load conditions have been reproduced as closely as possible. The bending mode is the load case that will be seen in the actual prototype hand controller, and a maximum failure load can be calculated as follows:

$$M_{\max} = F_{\text{hand}} \cdot l_3$$
$$F_{\text{test}} = \frac{2 \cdot M_{\max}}{EB}$$

- $M_{\max}$  is maximum bending moment expected in service (case of user hitting a physical limit stop)
- $F_{\text{hand}}$  is maximum user hand force. In our case we take this to be 40 N [3]
- $l_3$  is the length of the stage 3 linkage (see figure 1.4.3), 150mm.
- $EB$  is the distance from the simply supported edge to the end of the bonded area (see figure 4.1.1), 90mm.
- $F_{\text{test}}$  is the maximum force the sample is required to withstand without failure during the testing procedure

Applying the current values to the above equation, we get a minimum failure load of 133.33 N of force to be applied to the sample before first failure. If we take a minimum safety factor of 2.0, the load that will need to be supported by the sample is 266.67 N.

### 4.3 Test Results

The piston force vs. displacement curves for the four samples are shown in figure 4.3.1. The curves for tests 1, 2 and 3 show two definite failure modes. Figure 4.3.2 shows a failed specimen. These are caused by cracking in the epoxy bond. In the third region on the curve, the bond is fully failed, and the resistance to the bending of the sample is due entirely to the friction between the aluminum interface and the epoxy bond. The curve for test 4 shows only one failure, the catastrophic failure, followed by a similar region dominated by the friction force between the bond and the roughened aluminum insert. The *initial failure* (IF) is what will be dealt with in the comparison between the bond geometries.

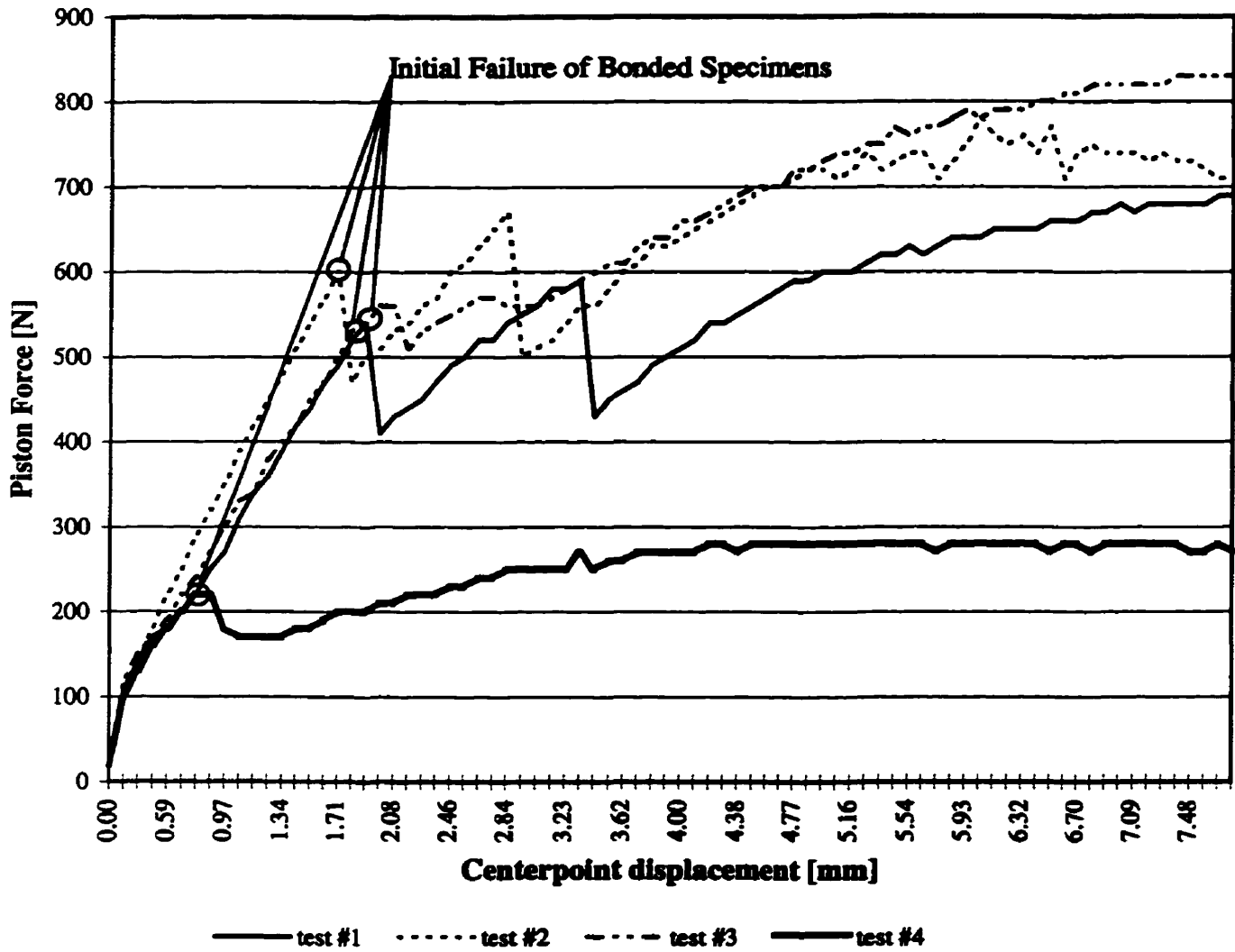


Figure 4.3.1 - Graph of piston force vs. centerpoint displacement

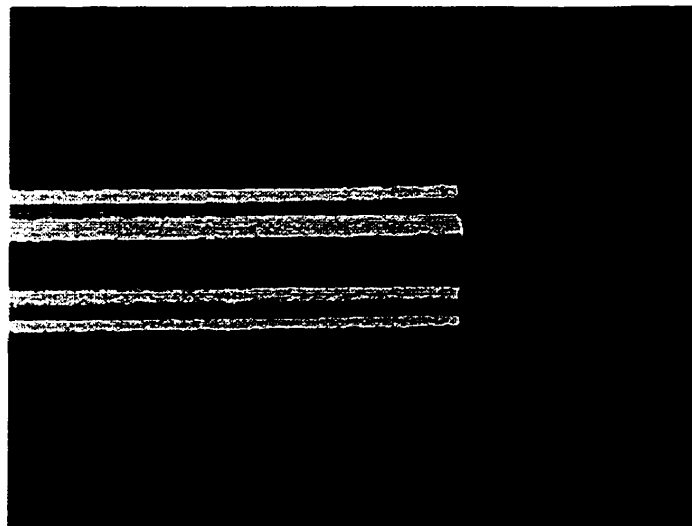


Figure 4.3.2 - Broken three-point bend specimen

The second sample, with an adherend wall thickness of 3.0 mm, shows the highest value of piston force for the IF. The IF occurs at 600 N. The third sample shows a IF at 560 N. The first sample's IF occurs at 540 N. Finally the fourth sample's IF occurs at 220 N.

From the curves, we can see the effect that each parameter has on the resulting strength of the bonded joint. As predicted in the axisymmetric model in chapter 3, increasing the bond line thickness and increasing the adherend thickness in effect strengthen the joint. However, it is obvious that the increase in strength is very slight compared to the increase in material in the joint. Decreasing the axial engagement of the joint decreased the overall strength of the joint. This coincides with the conclusions drawn from the finite element modeling performed in chapter 3. However, the effect on the overall strength of the joint is very great. The load that the joint can support before catastrophic failure is 40.7% of the nominal specimen (test sample #1). The joint in this case does not meet the safety requirements for use in structure.

It is interesting to note that the physical specimens showed a much higher failure load than predicted by the finite element model. The maximum piston force that should have been sustainable by the first sample, based on the finite element analysis, is 292.8 N. The actual value for the piston force at IF for the first sample was 1.91 times this theoretical value. However, the finite element model did not necessarily predict catastrophic failure. The physical test of the bonded sample may not have measured some initial cracking in the bond material that more closely matched the failure criterion obtained from the finite element model of the bonded joint. The physical test provides a factor of safety for the bond in bending of 2.33 over the worst load case scenario considered for a haptic device.

From these tests, we can see that the nominal joint configuration is very close to the optimized value. No great gains would be made in increasing the adherend wall thickness or the bond line thickness, and decreasing the axial engagement of the composite tube would jeopardize the overall strength of the bonded joint.

## ***5. Design of Box Beam***

### **5.1 Introduction**

The construction of a composite box beam to be used both as a structural member and as a cover for the distal stage strings was made for production and marketing reasons. A less expensive structure would consist entirely of the bonded composite tubes as described in the preceding chapters. However, the polymeric strings that are used to actuate the distal stage of the hand controller are fairly delicate, and should not be left exposed in a marketable product. Instead of using a tubular structure as the structural entity, and fixing a protective covering over it, thereby greatly increasing the link weight, the carbon fiber box-section was proposed as both a structural member and a cover to protect the distal stage strings.

### **5.2 Dimensional Requirements for the Box Beam**

The cross sectional dimensions of the box section for use as the distal linkage and the cover for the distal stage strings were determined by the interference requirements of the pulleys carrying the distal stage strings. The pulleys at the intersection of the stage 2 linkage and the distal stage linkage and the pulleys out at the distal stage are 23.75 mm in diameter and 6 mm in height. The pulleys at the distal stage also rotate  $\pm 45^\circ$  about an axis that is 3.25 mm below the center of the pulley. The centers of rotation of the distal stage pulleys are 32 mm apart, vertically. Through simple trigonometry, the clearance area for the box beam can be determined as 23.75 mm wide and 53.5 mm high. A cushion needs to be added around this minimum clearance to prevent interference between the bonded inserts that will be required for mounting the box-section to the other links in the translation stage and the distal strings. Figure 5.2.1 shows the clearance area for the strings at the distal stage end of the box section.

The box section requires a method of fixing to the rest of the translation stage structure. As with the bonded tubes, it was chosen to machine aluminum inserts to be

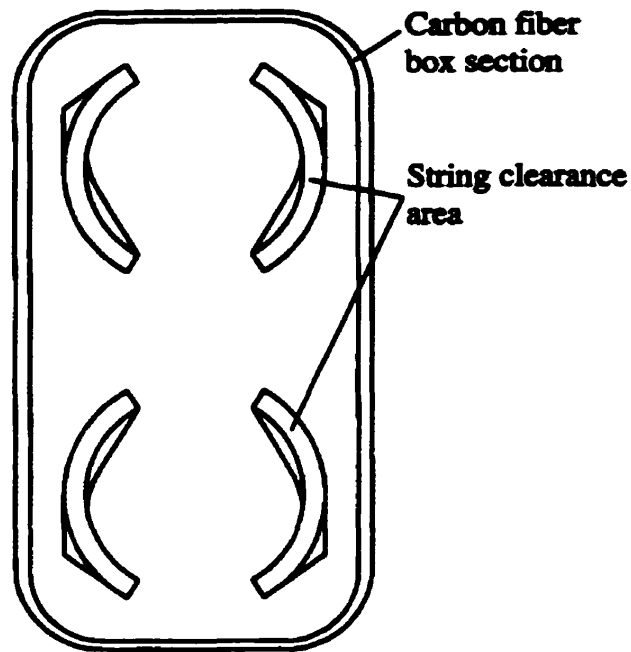


*Figure 5.2.1 - Clearance area for the distal stage driving strings*

adhesively bonded to the carbon material that would then become attachment points for the other aluminum parts required for the structure.

Figure 5.2.2 shows an exploded view of the assembly of the new carbon fiber

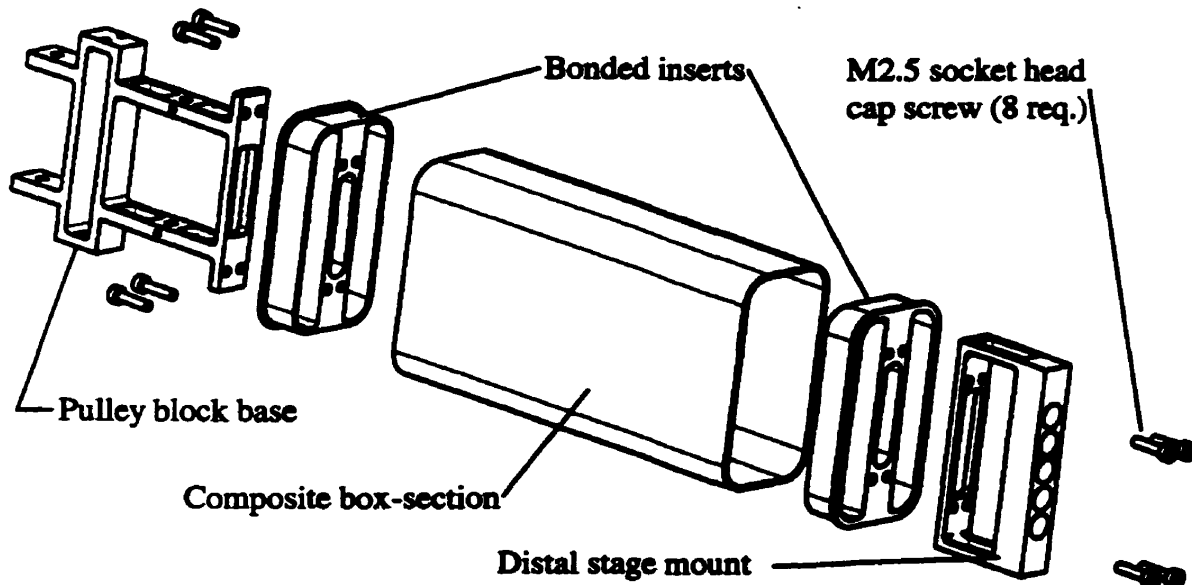


*Figure 5.2.2 - Exploded view of carbon fiber distal stage assembly*

distal stage assembly. The pulley block base served as a mounting point for the shafts connecting the distal linkage to the stage 2 and 3 linkages. The distal stage mount provided the interface with the rotational distal stage.

### 5.3 Finite Element Model of the Distal Stage Linkage

The design criterion for the translation stage of the hand controller is not based upon a traditional failure criterion, or even a displacement criterion as is often the case in robotics applications. The human haptic kinesthetic sense is not fine tuned enough to accurately discriminate between two points in space. Instead the lowest natural structural frequency of the assembly is the design goal.

To simulate a virtual contact with a solid wall with acceptable fidelity, the rate at which the signal is modified during the simulation is near 200 Hz. If the structural natural frequency is near or below 200 Hz, then resonances can be set up in the structure, reducing the fidelity of the simulation.

Three finite element models were constructed using I-DEAS Maters Series V2.0 of three separate distal linkage assemblies. The first finite element model was of the composite box-beam structure discussed here (figure 5.3.1). The second model corresponded to the proposed sheet-metal covered linkage (figure 5.3.2). An iterative process was used to determine the lay-up required for the composite part for it to have an equivalent deflection stiffness to the aluminum covered linkage. A lay-up of three woven layers (0/90) was chosen, for a lay-up of  $[(0/90)_3]_T$ . Unfortunately, due to the excessive cost associated with a filament winding machine, the only option for fabricating the box beam was hand lay-up. For this reason a more rigorous optimization of the laminate, including precise angle plies to increase material damping, was not possible within the scope of this work. Such an optimization process, however, is a suggestion for future work on this project.

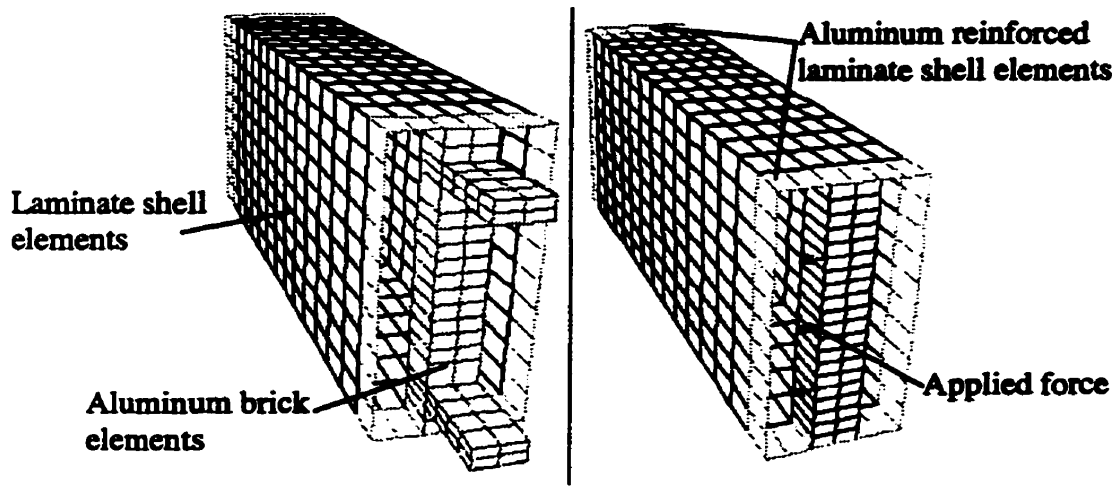


*Figure 5.3.1 - Finite element mesh of composite box-section linkage*

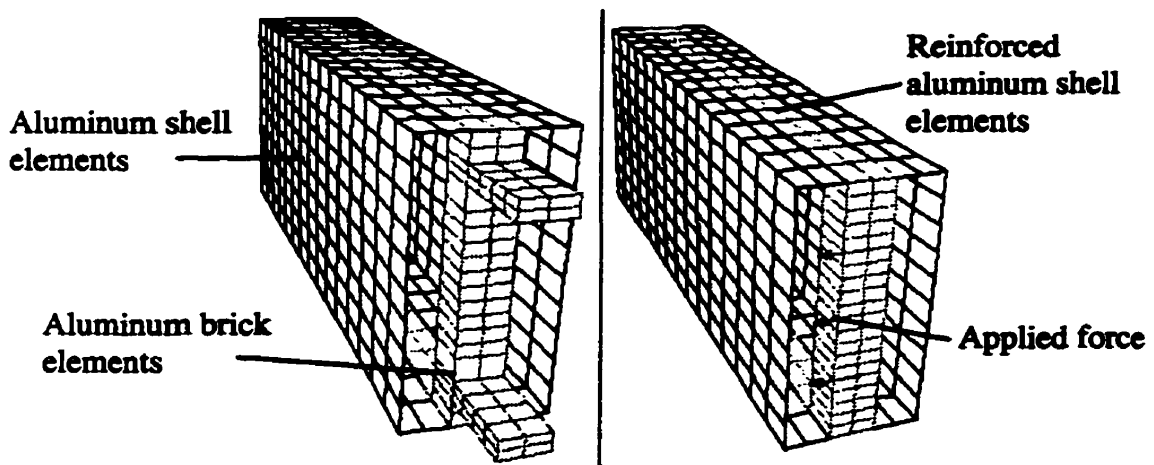


*Figure 5.3.2 - Finite element mesh of aluminum sheet-metal covered linkage*

## 5.4 Results of Finite Element Model

The finite element models were solved for a test load case of 10 N in static bending to determine the effective stiffness of the linkage. The models were also solved using a normal mode dynamics iterative solver to determine the lowest resonant natural frequencies for the first three modes. There were no boundary conditions placed on the models for planar motion during the normal mode dynamics solution because it was

	Aluminum Covered Linkage	Composite Linkage
Max. Deflection Vertically	1.50x10 <sup>-2</sup> mm	1.37x10 <sup>-2</sup> mm
Vertical Natural Freq.	552 Hz	728 Hz
Horizontal Natural Freq.	[ 186 Hz ]	221 Hz
Total Estimated Weight	127 g	82 g

*Table 5.4.1 Summary of Comparison Between Box Beam Finite Element Models*

desired to find the resonant frequencies in all three primary directions.

Table 5.4.1 summarizes the most important results of the modeling. From table 5.4.1, it is obvious that the composite linkage compares favorably to the aluminum covered linkage. There is a gain in vertical bending stiffness of the linkage of 8.67% for the composite linkage over the aluminum covered linkage. The vertical natural frequency of the composite linkage increases 31.89% over the aluminum covered linkage. The horizontal natural frequency of the aluminum linkage does not meet the design criterion of 200 Hz, while the composite linkage does. Finally, it is expected that a decrease in total weight of the linkage from the aluminum covered to the composite of 35.43% will occur. From these results, it is obvious that a composite box-section in place of an aluminum sheet-metal cover is a very advantageous design choice.

## ***6. Box Beam Prototype***

### **6.1 Carbon Fiber Box Beam**

The actual construction of the box beam prototype required several steps. The first step was the construction of an external *mold* for the carbon fiber material. The mold was made in two halves. The stock material for the mold was extruded aluminum channel. The use of the channel allowed for corners with consistent curvature of fairly large radius. It is important to avoid sharp corners when working with an external mold. The channel size was chosen to have the same internal dimensions as the external dimensions of the composite box-beam structure. The inner surface of the mold was polished to provide for a good surface finish for the composite piece. Holes were drilled and tapped in the walls of the channel to provide clamping points for the two halves of the mold. The purpose of the mold is to provide a rigid surface on which to place the carbon-fiber material to give it shape. The raw carbon-fiber material comes in the form of long sheets of woven or unidirectional fibers pre-impregnated with an epoxy *resin*. The epoxy resin holds the fibers together in the finished piece while the fibers, being much stronger than the epoxy, are responsible for carrying the loads applied to the part. The *lay-up* refers to the process by which layers of the carbon fiber material are placed in succession, one on top of the other, to create a wall thickness for the composite part. The material for the layers can be cut different ways to obtain different *fiber orientations*, allowing customization of layer properties as explained in Chapter 2.

The choice of an external mold was made for two reasons: first, the cross-section had to be hollow to allow the passing of the distal stage strings, and second, a marketable product would require a superior surface finish to be acceptable. While the first condition could be met with an internal, removable mold, the second required the external mold to prevent material wrinkling during the *cure*.

To cure a composite part, the carbon-fiber material has to be subjected to prolonged periods of heat and pressure in order to harden the epoxy resin. The cure cycle

refers to the controlled changes in pressure and temperature applied to the composite part during the hardening process of the epoxy resin. All composite materials require a cure cycle. However, some resins cure at much lower temperatures than others. The cure cycle that is used for the material chosen [37] for the composite box-section is the following:

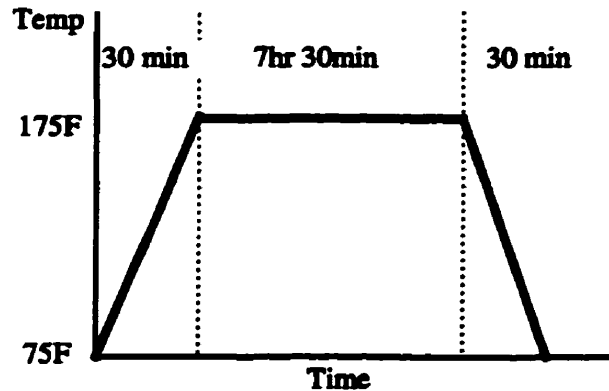


*Figure 6.1.1 - Time-temperature Profile for LTM25 Cure Cycle*

Previous attempts at a lay-up with the split mold were unsuccessful because of the choice of a thin teflon sheet as a *release film*. The release film is required so that the epoxy resin does not stick to the mold during the cure cycle. Several problems occurred with this technique. First, the mold had to be closed from the start of the lay-up process to allow for the insertion of the teflon film. Not only did this make the lay-up technique more difficult but didn't allow sufficient pressure to be applied to the corners of the box beam during curing. The teflon film had a tendency to stretch away from the corners of the mold, causing gaps between the part and the mold surface that, after curing, resulted in excessive dry spots on the outer surface.

Amisol, a company that produces Freekote liquid releases, was approached and they provided a combination of B15 liquid sealant and Freekote 700NC release agent to treat the inside of the mold [42]. This solution worked very well. Application of the sealant and release agent took 20 minutes plus polymerizing time (24 hours) and the resulting surface finish was much better than the originally proposed teflon film. The

release agent on the mold surface allowed the lay-up to be started with the mold apart, which made the lay-up technique much easier.

The first layer of the carbon-fiber material was put in place with the mold apart. Two pieces of the (0/90) woven carbon fiber material 45mm x 175mm were placed inside one half of the mold with the edges flush with the split edges of the mold. Two other pieces 60mm x 175 mm were placed in the other half with an overhang of approximately 15mm. The layers also overlap on the middle of the large face of the box beam by approximately 5mm. Part of the second layer of woven material is added before the mold is joined to allow for better placement and compression of the layers. Two pieces of 60mm x 175mm are cut of the [0/90] woven material and are placed flat on the large surface of the mold, with a small overlap of approximately 5mm beyond the midpoint of the corner curvature. This small overlap is essential for good bonding of the full layer to the smaller 30mm x 175mm pieces that are added once the mold is closed. A complete third layer consisting of two pieces of 60mm x 175 mm, and two of 30mm x 175 mm are put in place with the mold closed. The final result is a lay-up consisting of three layers,  $[(0/90)_3]_T$ , where the (0/90) group represents the woven graphite material. In the regions of overlap near the corners, the lay-up is actually  $[(0/90)_5]_T$ , and along the middle of the large face of the box-beam,  $[(0/90)_4]_T$ . The lay-up process is shown step by step in figure 6.1.2.

Two pieces of the teflon release film were applied to the inside of the composite part, followed by a layer of breather material for the even application of the vacuum to the whole piece. The teflon film in this case prevents the breather material from sticking to the cured epoxy. The *vacuum bag* is a sealed plastic sheet that completely covers the part. By drawing a vacuum inside this bag, the composite material is pressed up against the wall of the mold, compressing the layers together and forming a much stronger piece. The reason it is necessary to avoid sharp corners in an external mold, as was mentioned above, is that the vacuum bag cannot infiltrate a sharp radius to apply an even pressure on the composite material. It is the lack of vacuum pressure on the material that causes dry spots to occur.

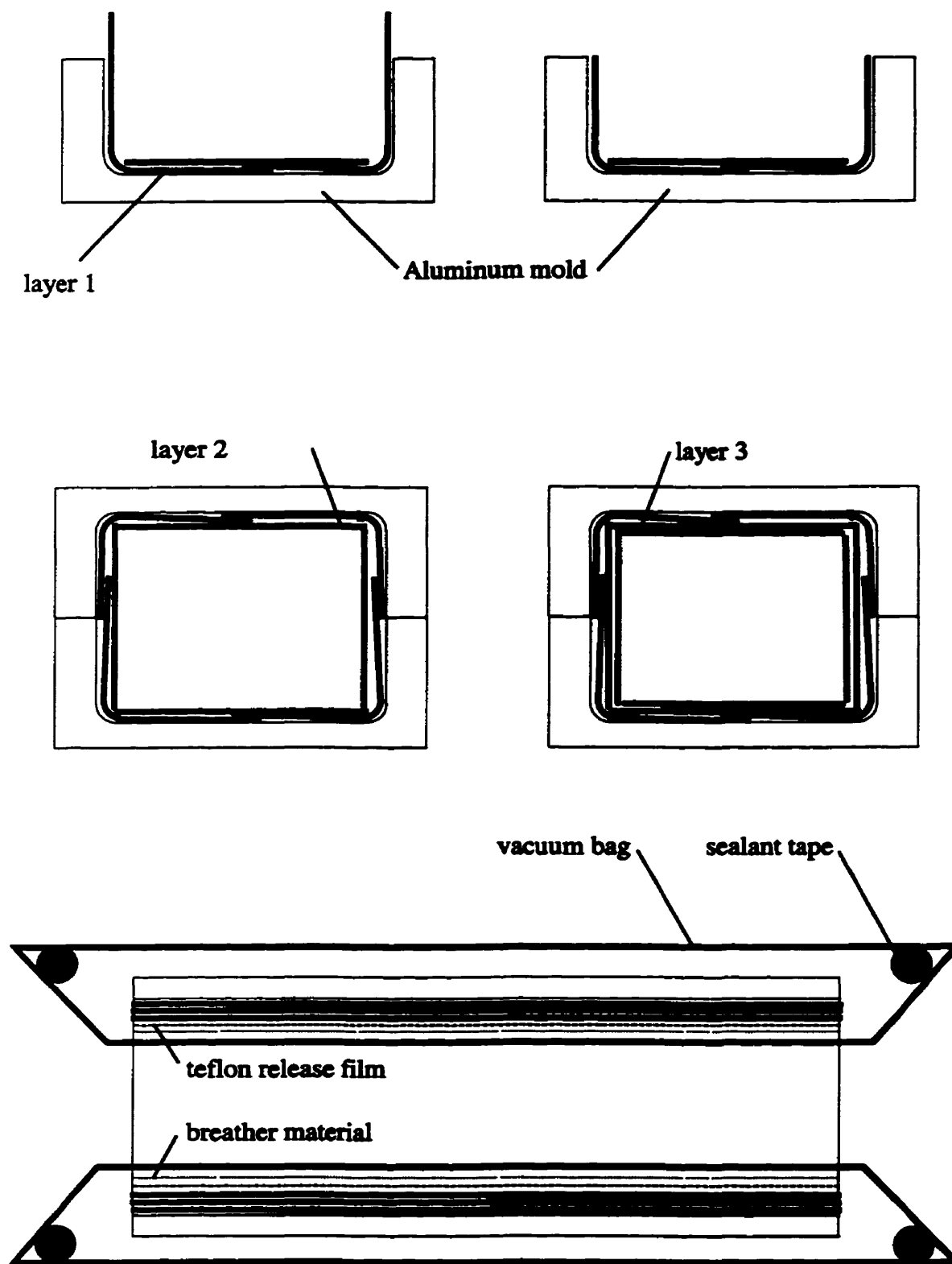


*Figure 6.1.2 - Lay-up Procedure for Composite Box-Section*

The vacuum bagging technique was slightly different that is traditional for an external mold application. The oven to be used did not have a pressurizing pump, only a vacuum pump attachment. Therefore, instead of an inflatable internal bladder to apply pressure to the part, a cylindrical arrangement of the vacuum bag was devised. Two cylinders of vacuum bagging material, sealed along the side, were placed inside and outside the mold. The ends were then sealed to each other along the circumference. This allowed for atmospheric pressure to be applied to the full internal surface of the mold, without the added expense of an inflatable bladder.

The cured piece had good surface finish on both the outside and inside surfaces. There was no wrinkling on the inside surface of the box beam because the material was slightly under tension. It was difficult to get even pressure into the corners, and they ended up slightly resin rich. It was obvious by looking at the thickness of the walls throughout the cross section. The best compression occurred on the large face of the box beam. This leads to a slight problem with dimensional tolerances. It is difficult to control the final interior dimensions of the box beam since they are very dependent the compression that could be obtained on the faces of the part and the quality of the vacuum pressure in the corners. For the case of the Freedom-7 project, good dimensional control was required on the inside surface of the box beam since machined end fittings are to be bonded to this inside surface.

## 6.2 End Fittings

The final design of the end fittings was determined after significant progress had already been made on the construction of the box beam. Originally, small plates fixed on the exterior surface of the box beam were intended to be used as mounting points for the various aluminum parts required for the bearing mounts and joint shafts of the hand controller. Last minute design changes led to a modification of this idea to allow for precisely machined, end fittings to be bonded to the inside wall of the box section. As discussed in the previous section, the interior dimensions of the box beam are not well controlled and can seriously affect the bond line thickness and, consequently, the strength of the bonded joint. As well, due to the close clearance selected for the distal stage

strings, the wall thickness of the metal insert must necessarily be very small, which poses machining difficulties. A compromise was made between these various requirements, and the piece was designed.

The material selection for the end fitting was another problem area. One of the design goals of the Freedom-7 was reduced link inertia. To achieve this goal, parts of minimum weight were required for all areas. The existing metal prototype it made entirely of aluminum-6061. To avoid using two different metals and encouraging galvanic corrosion among the metallic parts, it would be logical to choose aluminum 6061 as the material for the bonded inserts. However, aluminum forms an oxide very easily in air and this aluminum oxide is highly anodic. In the presence of an electrolyte such as sea water, there can be significant corrosion of the contact surfaces between aluminum and a cathodic material such as graphite. As a result, the aluminum end fittings require etching to remove the aluminum oxide layer on the bonding surface before the bonding operation.

The West-System's aluminum etching kit [43] was used to prepare the bonding surface of the aluminum inserts. The portions of the insert not subject to adhesive bonding were masked with tape, and the etching process was carried out according to the directions on the etching kit. With the careful preparation of the aluminum and composite surfaces the galvanic corrosion of these parts should be kept to a minimum.

### **6.3 Bonding of End Fittings**

The bonding of the aluminum end fittings required the construction of a jig to keep the two planes of the end fittings parallel. The jig consisted of two accurately machined right angle L's mounted on magnetic bases. The magnetic bases fix themselves to the top of a metal level table. The right angles make use of the mounting holes on the end-fittings to hold the end-fittings in place. A dial-gauge was used to measure the deviation of the end-fittings and the box-section from parallel.

As sated before, the internal dimensions of the box-section were poorly controlled with the manufacturing method. The resin rich areas in the corners of the box-section had to be filed down to allow the end-fittings to fit inside.

One standard procedure for ensuring even bond line thickness over a large bonding area is to use small gauge wire embedded in the bond material to act as a spacer during the adhesive bonding [36]. These wires normally overlap the bonded region and are cut flush with the edge once the adhesive is cured. These wires are not needed in this case to maintain the bond line thickness as the corners of the metal inserts are in contact with the resin rich areas in the corners of the box-section. The main shear carrying areas of the bonded interface, the flat faces of the bonded region, have a good, uniform bond line thickness without the discontinuities and potential stress concentration points that could be caused by the inclusion of the standard wire spacers in the bonded region.

Due to the long cure time (24 hours) of the Adbond epoxy [40], there was some seepage around the interface with the end fitting and the composite material. The strength of the bond was not compromised, as the bond length was designed with a large factor of safety. However, for future production, an epoxy with a much lower cure time should be considered.

## 6.4 Structural Tests on Freedom-7

The existing aluminum prototype at MPB Technologies was configured in such a way as to be able to accept both a distal stage linkage and a stage three linkage in the form of a box beam. Therefore, a second box beam was constructed using the same technique as for the first, and substituted for the stage three linkage (instead of using the bonded composite tubes). This was a marketing design change, and will not affect the continuing research into the proper design of bonded interfaces for small diameter composite tubing that continues in the next chapters.

	End Fittings	Carbon Fiber	Overall Composite	Equivalent Aluminum
Distal Stage Link	17.5 g x 2	23.7 g	101.5 g	103.2 g
Stage 3 Link	17.5 g x 2	28.0 g	106.6 g	98.2 g

*Table 6.4.1- Weight Distribution for Box-Beam Parts*

The weights of the individual parts of the box beam assemblies are shown in table 6.4.1, as well as the overall weights of the assembled linkages and the corresponding aluminum linkages. They do not match with the estimated weights from table 5.4.1. It is obvious from the weight breakdown that the aluminum inserts for the composite box beams are significantly over-designed. As mentioned before, the machinists have difficulties working with aluminum of very thin wall thickness. Therefore, to facilitate the machining process, the wall thicknesses were increased and more material was left in the center for mounting of the interface parts. The weights of the end fittings account for 34.4% and 32.8% of the overall weights of the distal and stage 3 linkages respectively. It is by no means unreasonable to consider that a redesign of the end fittings could reduce their weight by 50%, making the overall weight of the link assemblies 84g for the distal stage linkage and 89.1 g for the stage 3 linkage, which would be much closer to the original estimated weights. This redesign would constitute a weight savings of 19.2 grams, or 18.6%, in the distal stage, which is the major contributor to the overall inertia of the translation stage.

## 6.5 Frequency Response of Translation Stage

Two dynamic response tests were performed on the translation stage of the Freedom-7 hand controller. The first consisted of sending a frequency varying sine wave individually to each of the three motors and measuring the end effector acceleration in the nominal direction governed by each motor. The purpose of this test was to determine the resonant frequencies of the structure in each direction. If we consider the translation stage to be planar, with the positive x-direction parallel to the stage 1 and 3 linkages pointing towards the motor mounts from the distal stage, the positive y-direction parallel to the distal stage linkage pointing out towards the user, the right hand rule gives us the positive z-direction as downwards perpendicular to the plane of the translation stage (see figure 1.4.6). A small magnitude rotation of the stage 3 motor about the centered position provides an instantaneous movement along the x-axis. The small magnitude rotation of the stage 2 motor provides movement along the y-axis. The small magnitude rotation of the stage 1 motor governs the displacement along the z-axis. It is important to note that, as the stage 1 and 3 motors are co-planar, their effects on the displacement of

the distal stage are coupled. Therefore, the independent axes only hold for small magnitudes of joint displacement around the neutral position. The neutral position has all the joint angles at  $90^\circ$ . The second series of dynamic tests to be performed on the translation stage consisted of inducing an impulse in the motors of a set amplitude and duration and measuring the maximum acceleration of the end effector. This test was performed in order to measure the overall inertia of the structure in each of the three motor directions.

Ideally, the resonant frequency for the structure in each of the three directions should be greater than 200 Hz. This is an adequate resolution to simulate contact with a solid surface in a virtual environment. The maximum acceleration at the end effector for the motor impulse test should be as high as possible, yet equal in all directions. The higher the maximum acceleration at the end effector, the greater the *crispness* of the device. Haptic sensations will feel more realistic and less sluggish. However, if the maximum acceleration is not the same for each link, the operator may sense a change in the response of the device based upon the device's orientation. This is undesirable, as the Freedom-7 is intended to be able to be oriented in any direction.

For convenience, the frequency response curves have been grouped in Appendix B. Figures B1 through B5 show the accelerometer output vs. the excitation frequency of the stage 1 motor (z-direction) for the five configurations of the translation stage links. B1 shows the response of the aluminum structure after a very careful assembly, with proper pre-tensioning of the bearings and alignment of the shafts. B2 shows the response of the aluminum structure after a somewhat less controlled, less experienced assembly procedure. B3 shows the response for the translation stage with the two carbon fiber links included in the structure. B4 shows the response with only the carbon fiber distal stage linkage and B5, with only the stage 3 linkage. Similar tests were performed for each of the other two motors, with figures B6 through B10 referring to the stage 2 motors (y-direction) and figures B11 through B15 referring to the stage 3 (x-direction) motor. A summary of the first resonant frequency for the translation stage in each configuration can be found in table 6.5.1.

	x-direction	y-direction	z-direction
Original Aluminum Assembly	189.9 Hz	115.0 Hz	100.1 Hz
Second Aluminum Assembly	103.9 Hz	95.6 Hz	94.2 Hz
Two Carbon Linkages	128.0 Hz	127.8 Hz	102.9 Hz
Carbon Distal Stage Linkage	115.9 Hz	91.9 Hz	91.9 Hz
Carbon Stage 3 Linkage	109.9 Hz	130.3 Hz	101.3 Hz

*Table 6.5.1- Summary of First Resonant Frequencies for the Freedom-7 Translation Stage*

Several conclusions may be drawn from these tests about the frequency response of the translation stage. First, the frequency response of the translation stage is heavily dependent on the assembly procedure. For the stage 1 mode, the aluminum prototype experienced a drop of the natural frequency of 7.75% between the careful and inexperienced assemblies. Second, the stage 1 mode was not affected by the inclusion of the carbon linkages, as the frequency response is dependent on the stiffness in bending of the stage 2 linkage (which was not modified) and the mass of the distal stage, which as discussed before, suffered from difficulties in the machining of the end fittings. Third, the incorporation of the carbon links improved the frequency response for the stage 2 mode. With the inclusion of the two composite links the natural frequency rose 12.2% over the original assembly and 20.6% over the inexperienced assembly. The stage 3 linkage was the greatest contributor to this improvement, and for the test with it alone, the natural frequency was 22.4% higher than the inexperienced assembly of the aluminum prototype. Fourth, the inexperience of the assembly contributed to the damping of the translation stage. In every case the magnitude of the signal from the accelerometer was higher for the original assembly of the aluminum structure than for the inexperienced assembly of the aluminum structure. Finally, there was a problem with the design of the pulley block base (see figure 5.2.2). The inclusion of the carbon distal stage was very detrimental to the performance of the stage 3 mode. The natural frequency dropped by 34.0% and the magnitude of the signal was very high. The assembly with only the stage 3

linkage out of carbon behaved similarly to the aluminum prototype, so its contribution to this mode is considered limited.

## 6.6 Refined Finite Element Model of Distal Stage Linkage

Further investigation was required to determine the cause of the poor performance. More refined finite element models than the one constructed in chapter 5 were used to determine specifically the modal vibrations in the x-direction for the distal stage linkage. The author was suspicious of the strength in bending of the pulley block base, as the weight reducing cutouts could significantly compromise the stiffness of the part. For this reason, two models were used. The first modeled the distal stage linkage as it was for the physical tests (figure 6.6.1). The second added a reinforcing cover that extended from the carbon fiber material back over the pulley block base (figure 6.6.2), similar to the configuration seen in the sketch in figure 1.4.6.

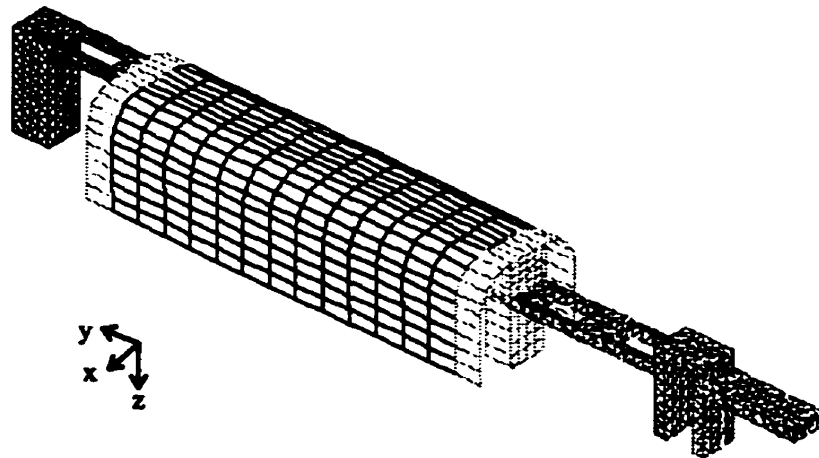


*Figure 6.6.1 - Refined model of distal linkage for vibration simulation*

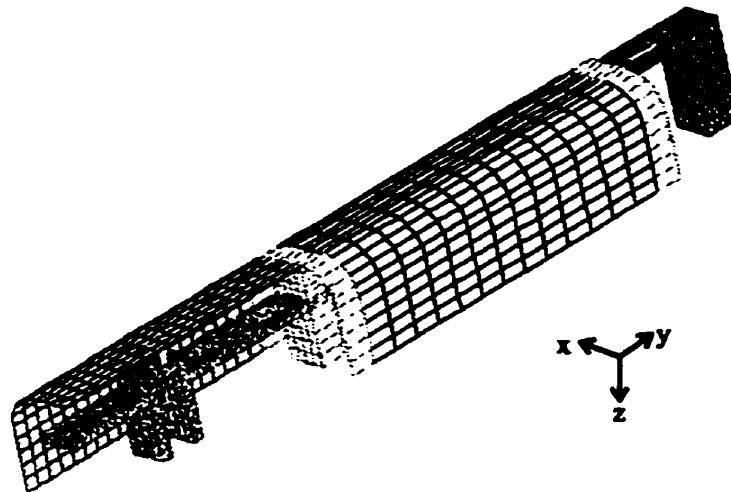


*Figure 6.6.2 - Refined finite element model of distal linkage with added cover for vibration simulation*

The two models were solved using the iterative normal mode vibration solver in I-DEAS Masters Series V2.0. They were constrained to move along the  $x$ - $z$  plane, in order to simulate the vibrational modes that would occur for the stage 3 excitation. The shafts were considered as pin connections with the axis of rotation along the  $y$ -axis. The first normal mode vibration result for the uncovered distal stage is shown in figure 6.6.3.

The black outline shows the vibration mode, which is about the stage 2 linkage axis. The frequency of vibration is shown at 127.93 Hz, which is very close to the measured frequency of the vibration in the  $x$ -direction with only the carbon distal stage shown in Appendix B, figure B14 of 139 Hz. The model seems to be a little less stiff than the physical structure, and tends to vibrate at a slightly lower frequency. This might also be accounted for by the lack of material damping in the finite element model as well as the inaccuracy of modeling the bearing and other interface behaviors as described in section 6.5. The lack of material damping could cause errors up to 5% and the interface effects could account for an additional 10% error in the natural frequencies, based on the vibration tests performed on the aluminum prototype.

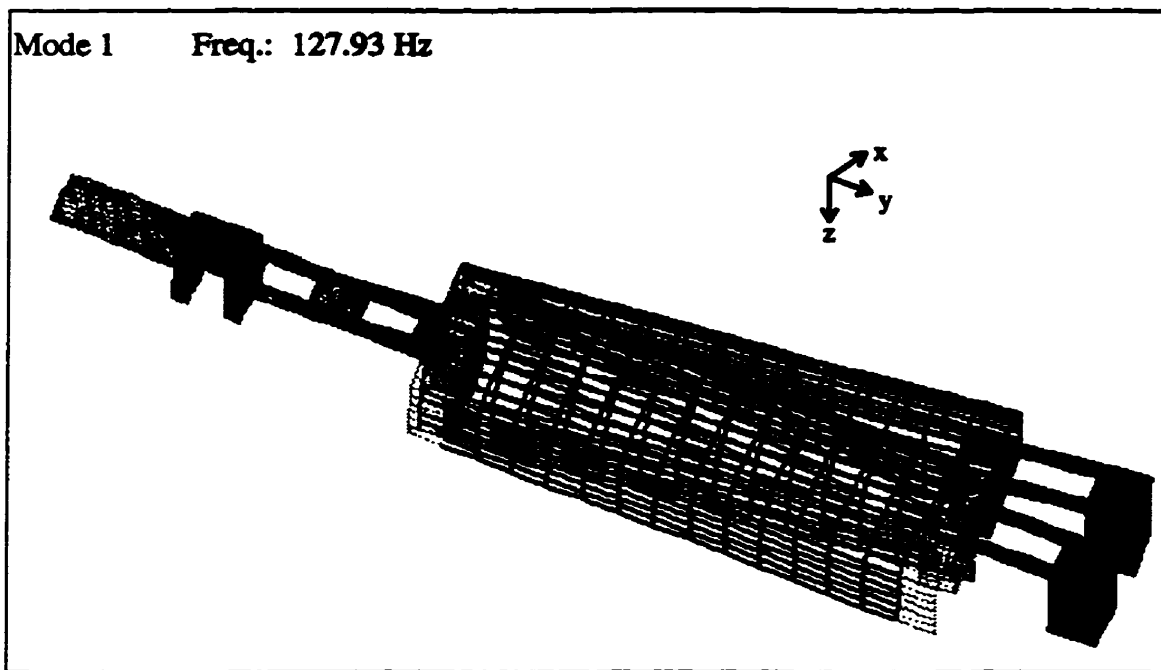


*Figure 6.6.4 - Normal mode vibration in x direction for uncovered distal stage*

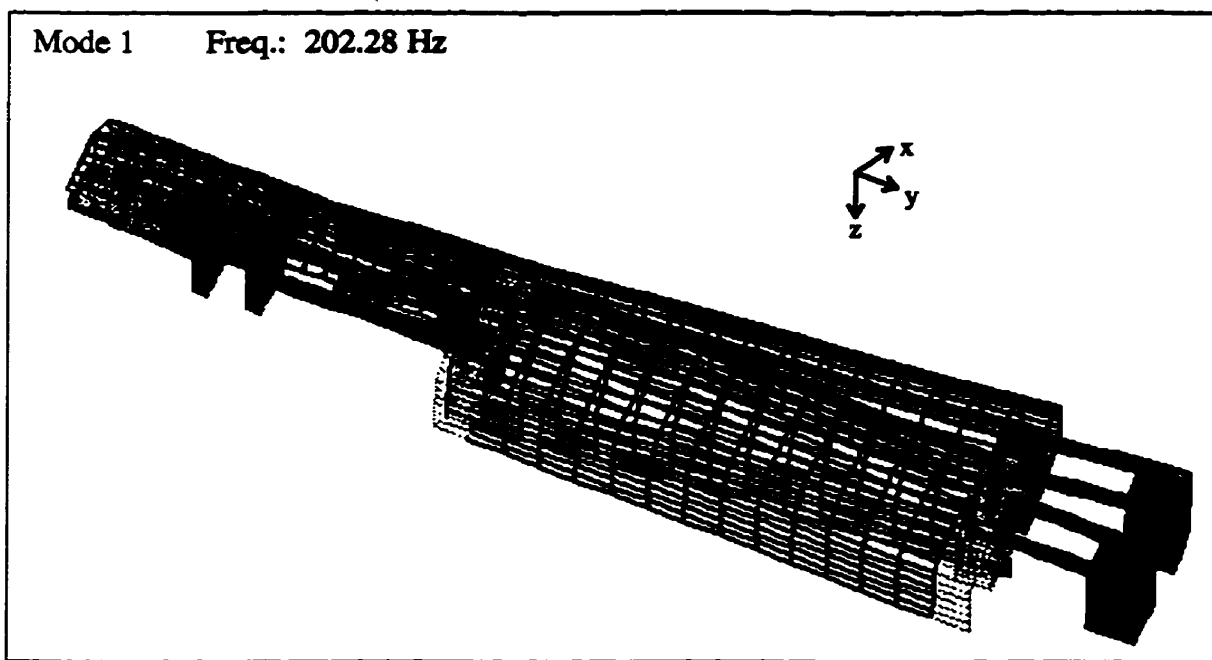


*Figure 6.6.3 - Normal mode vibration in x direction of distal stage with an added cover*

The solution of the covered model for the modal vibrations is shown in figure 6.6.4. The frequency of vibration is 202.28 Hz for the first modal frequency in the x-direction. Even if we do not take into account the slightly lower value for the natural frequency of vibration in the finite element model, incorporating this design into the translation stage structure would result in an increase in the natural frequency of 5.9% over the aluminum box beam prototype. Obviously, the assumption that the lack of stiffness in the pulley block base was the result of the poor frequency response is correct, and the inclusion of a composite cover over the pulley block base is an excellent solution.

In order to determine the problem in the pulley block base that caused the weakness in the x-direction vibration, the two models were solved for the static load case where a load of 10 N was applied to the stage 3 linkage shaft in the x-direction and the distal stage mount was clamped in place. The maximum principle stress contours in the pulley block base for this load case are displayed in figure 6.6.5 for the uncovered distal linkage and in figure 6.6.6 for the covered distal linkage.

From the contours, it is obvious that the weak point in the pulley block base comes from the weight reduction cutouts around the shaft that joins the distal and the stage 2 linkages. The cutouts create non-rigid sections in these areas because they are cut right through instead of having a small flange as would an I-beam. For the covered distal stage linkage, the magnitude of the stress in the weaker region around the shaft holes is much less than for the uncovered case. It is also apparent that some of the load is transferred through the stand-off between the two shaft holes to the composite cover. This redistribution of the load explains the gains in structural stiffness obtained by adding a composite cover to this piece.

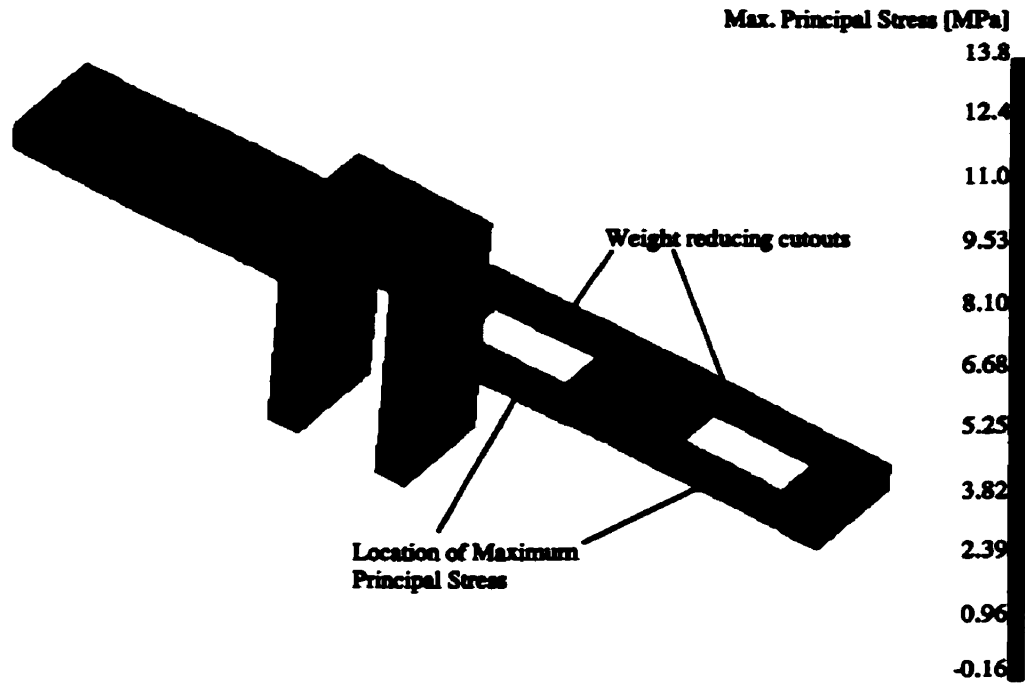


Figure 6.6.5 - Stress contours in uncovered pulley block base

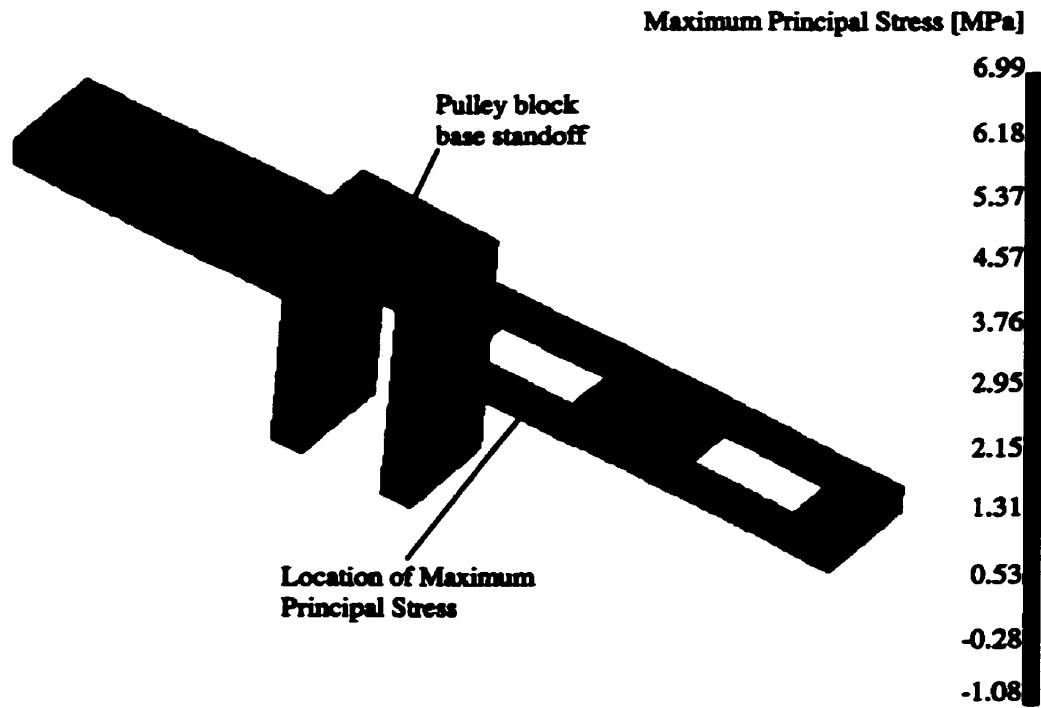


Figure 6.6.6 - Stress contours in covered pulley block base

## 6.7 Maximum Acceleration Test

In order to measure the reduction in link inertia, a test was performed to measure the maximum acceleration of the end effector for a given impulse function. It is desirable to have the highest end effector acceleration possible. A higher end effector acceleration capability will allow a greater crispness of the haptic sensations fed back to the user through the device.

The physical test for the maximum link acceleration consisted of sending a single 10 ms pulse of 10 V peak to each of the motors in turn, and measuring the instantaneous output of the accelerometer mounted at the end effector position on the translation stage in each case. This test will be referred to as the *beep* test, as the signal sent to the motors is a short voltage beep. The signal was generated by a polynomial waveform synthesizer, model 2020 by ANALOGIC. The waveform synthesizer was programmed to a square wave of period 10 seconds, amplitude 10 V peak and a duty cycle of 0.1%. The pulse was used to trigger a single sampling display for a digital oscilloscope, which read the output of the accelerometer.

The beep test was performed on each configuration of the translation stage (except for the original aluminum assembly) for each motor direction. The output of the accelerometer had been calibrated to 10.20 mV/g according to [44]. Table 6.7.1 summarizes the results of the maximum acceleration tests.

	x direction (stage 3)	y direction (stage 2)	z direction (stage 1)
Aluminum assembly	3.43 g	2.94 g	2.94 g
Two composite linkages	3.92 g	2.94 g	3.92 g
Composite distal stage linkage	3.92 g	3.92 g	3.92 g
Composite stage 3 linkage	3.43 g	2.54 g	2.94 g

Table 6.7.1 - Summary of maximum acceleration test on Freedom-7 translation stage

The results of this test show that, for the most part, the inclusion of the composite links have a beneficial effect on the maximum end effector acceleration. The greatest

gains are made in the x and z directions for the inclusion of both composite links. However, with the redesign of the metallic end fittings, the gains in maximum acceleration should be higher, as the link weights and therefore the counterbalancing weights should decrease along with the structural inertia.

## **6.8 Summary for Box Beam Prototyping and Testing**

The hand lay-up method for fabricating a composite box beam is time consuming and inappropriate for a production model of the haptic hand controller. A more suitable manufacturing method would be filament winding. Accurate fiber orientations, along with good dimensional tolerances could be obtained for a much longer box section, that could then be cut to the required lengths for the linkages. However, for prototyping purposes, the hand lay-up in the external mold provided a good surface finish and was less expensive than obtaining a filament winding machine.

The design of the metal end fittings was not carried out rigorously enough. An overly cautious design coupled with the inherent difficulties in machining aluminum parts with small wall thickness created a part that was too heavy for the design requirements. By simply revising the part to be have one half the bond engagement would decrease the weight of the end fitting by 50% and approach the required design criterion.

The bonding of the aluminum end fittings to the composite box beam was accomplished without difficulty using a bonding jig to hold the parts in place during the epoxy cure. A shorter cure epoxy could be substituted to allow for a quicker assembly time for the linkage.

The inclusion of composite materials has benefits beyond what was measured in the physical tests on the translation stage. The vibration characteristics of the translation stage are very heavily dependent on the assembly process, and the inexperience of the author resulted in assembly dominated values for the lowest natural frequency of vibration in some modes for the translation stage.

The vibration modes that took advantage of the composite material showed some improvement over the aluminum prototype. There was little gain in the maximum acceleration of the end effector due to the over-design of the bonded inserts that increased the weight of the composite links. Problems associated with the design of the aluminum

interface parts such as the pulley block base for the distal stage also contributed to the poor performance of the composite linkages. Further finite element analysis confirmed the weakness of the pulley block base part, and showed that the simple inclusion of a composite cover to reinforce this part would greatly improve the dynamic response of the composite distal stage linkage.

It is clear that the composite materials show benefits for the dynamic performance, however more care has to be taken with the construction of the metal interface parts that are needed for the incorporation of the advanced materials into the structure.

## ***7. Conclusions and Recommendations***

This thesis has undertaken to refine and improve the design of the Freedom-7 haptic hand controller for dynamic and structural response. Analysis was performed to determine the optimum method for inclusion of composite materials in the translation stage of the hand controller. Improvements have been made in the analysis and design of composite parts for robotic applications:

- An optimized bond geometry is proposed for the joining of small diameter composite tubes to metallic inserts. The finite element modeling predicts a failure that is slightly lower than the measured failure of the test specimens. This configuration is proposed as a replacement for machined aluminum linkages in the translation stage of the hand controller, such as the stage 3 linkage.
- Physical testing of the optimized bonded geometry confirmed the analytical effects obtained through finite element analysis. The strength of the bond in bending is only weakly dependent on the adherend wall thickness and the bond line thickness, but is very dependent on the axial engagement of the tube and the aluminum insert. The overall strength of the physical specimen was higher than that of the finite element model, suggesting an overly conservative modeling of the joint.
- The distal stage linkage of the translation stage of the Freedom-7 is replaced by a box beam structure that is at once a structural element of the translation stage and a protective covering for the distal stage strings. The lay-up and box-beam structure of the carbon fiber is beneficial to the dynamic performance of the translation stage. However, insufficient strength in the machined aluminum inserts are responsible for a drop in the lowest natural resonant frequency of the translation stage.
- Swept sine tests were performed on the translation stage, using an accelerometer to measure the resonant peak vibrations at the end effector. This allowed for a separation of the modal vibrations for the excitation of each motor individually.

- **Maximum link accelerations were measured using an accelerometer mounted at the end effector for a voltage pulse to each motor. The response of the translation stage to this excitation depends on the link weights and inertias as much as the actuator capabilities.**

## **7.1 Recommendations for Future Work**

The Freedom-7 haptic hand controller could greatly benefit from the inclusion of composite materials in the structure of the translation stage. However, more work is required to narrow the design requirements to allow for proper exploitation of the potentials of the composite material parts. The following are some suggestions for future work on the Freedom-7 project, based on the observations and conclusions drawn from this work:

- **Implement the addition of a reinforcing cover over the pulley block base. The addition of a reinforcing cover of carbon fiber material over the pulley block base of the distal stage has been shown, by finite element analysis to improve the dynamic performance of the distal stage linkage.**
- **Redesign the bonded aluminum inserts on the distal stage box beam for reduced weight.**
- **Perform an extensive analysis on the human haptic system to determine specific requirements of a haptic manipulator, such as maximum allowable end point deflection, sensory bandwidth, etc..**
- **Perform a complete lay-up optimization routine on the linkages of the translation stage to determine the optimum fiber orientations for the specific haptic requirements and produce filament wound box sections using this lay-up.**

## **8. Bibliography**

1. Hayward, V. & Astley, O.R., "Performance Measures for Haptic Interfaces", *Robotics Research: the 7<sup>th</sup> International Symposium*, Springer Verlag, pp.195-207.
2. Durlach, Nathaniel, & Mavor, Anne, eds., "Virtual Reality: Scientific and Technological Challenges", National Academy Press, Washington, 1995.
3. Massie, T., "So Real I Can Almost Touch It: The Use of Touch as an I/O Device for Graphics and Visualization", *Course Notes for SIGGRAPH '97*, University of California at San Diego, 1996.
4. Yim, Mark, "The Haptic Device Spectrum", *Course Notes for SIGGRAPH '97*, University of California at San Diego, 1996.
5. Massie, Thomas & J. Kenneth Salisbury, "The PHANTOM Haptic Interface: a Device for Probing Virtual Objects", *Dynamic Systems and Control*, Vol.1, ASME 1994, pp.295-299.
6. Strong, Chris and Sinclair, Ian, "Large Workspace Hand Controller", MPB Technologies Inc., March 31, 1995.
7. Salcudean, S.E. et al., "Design and Control of a Force-Reflecting Teleoperation System with Magnetically Levitated Master and Wrist", *IEEE Transactions on Robotics and Automation*, Vol.11, No.6, Dec. 1995, pp.844-857.
8. Lee, Dai Gil, et al., "Development of the Anthropomorphic Robot with Carbon Fiber Epoxy Composite Materials", *Composite Structures*, Vol. 25, 1993, pp.313-324.
9. Ni, R.G. & Adams, R.D., "The Damping and Dynamic Moduli of Symmetric Laminated Composite Beams - Theoretical and Experimental Results", *Journal of Composite Materials*, Vol. 18, Mar. 1984, pp.104-212.
10. Adams, R.D. & Bacon, D.G.C., "The Dynamic Properties of Unidirectional Fiber Reinforced Composites in Flexure and Torsion", *Journal of Composite Materials*, Vol.7, Jan.1973, pp.53-67.
11. Lee, Dai Gil, et al., "Manufacturing of a SCARA Type Direct-Drive Robot with Graphite Fiber Composite Material", *Robotica*, Vol.9, 1991, pp.219-229.

12. Sung, C.K. & Shyl, S.S., "A Composite Laminated Box-Section Beam Design for Obtaining Optimal Elastodynamic Responses of a Flexible Robot Manipulator", *International Journal of Mechanical Science*, Vol.32, No.5, 1990, pp.391-403.
13. Adams, R.D. and Bacon, D.G.C., "Effect of Fiber Orientation and Laminate Geometry on the Dynamic Properties of CFRP", *Journal of Composite Materials*, Vol.7, Oct.1973, pp.402-431.
14. Sung, C.K., & Thompson, B.S., "A Methodology for Synthesizing High-Performance Robots Fabricated with Optimally Tailored Composite Laminates", *Transactions of the ASME*, Vol.109, Mar.1987, pp.74-86.
15. Rosenberg et al., "Electromechanical Human-Computer Interface with Force Feedback", United States Patent # 5 576 727, Nov. 19, 1996.
16. Burdea, Grigore C., "Force and Touch Feedback for Virtual Reality", John Wiley and Sons, NY, 1996.
17. Laschet, G., "Numerical Strength Predictions of Adhesively Bonded Multimaterial Joints", AGARD-CP-590, No.12, Jan.1997.
18. Immersion Corporation homepage, [www.immerse.com](http://www.immerse.com).
19. "Project Proposal: Stylus Hand Controller", MPB Technologies Inc. & McGill University, January 10, 1996.
20. Hayward, Vincent, "Toward a Seven axis Haptic Device", IROS'95. Pittsburgh, August 1995.
21. Lawrence, Dale A., & Chapel, Jim D., "Performance Trade-offs for Hand Controller Design", *IEEE International Conference on Robotics and Automation*, 1994, Vol.4, pp.3211-3216.
22. Hayward, V., et. al., "Freedom-7: A High Fidelity Seven Axis Haptic Device with Application to Surgical Training", to appear in ISER'97, June 15-18, 1997, Barcelona Spain.
23. Fasse, Ernest D., & Hogan, Neville, "Quantitative Measurement of Haptic Perception", *IEEE International Conference on Robotics and Automation*, 1994, Vol.4, pp.3199-3204.

24. Kazerooni, H., & Snyder, T.J., "Case Study on Haptic Devices: Human-Induced Instability in Powered Hand Controllers", *Journal of Guidance, Control and Dynamics*, Vol.18, No.1, Jan-Feb 1995, pp.108-113.
25. Lees, Dr. W.A., "Stress in Bonded Joints", *Adhesion*, Vol.12, 1988, pp.141-158.
26. Adams, R.D., & Harris, J.A., "Bonding of Composites to Metals", *Adhesion*, Vo.12, 1988, pp.193-204.
27. Xiong, Y., & Raizenne, D., "Stress and Failure in Bonded Composite-to-Metal Joints", AGARD-CP-590,no.10, Jan.1997.
28. Charalambides, M.N., et al., "Strength Prediction of Bonded Joints", AGARD-CP-590, No.11, Jan.1997.
29. Price, A. & Molds, J., "Bonded Propshafts: design and Assembly of Composite Tubes and Metal End Fittings", *Materials Science and Technology*, Vol.9, June 1993, pp.528-535.
30. Gordaninejad, F. et al., "Nonlinear Deformation of a Shear-Deformable Laminated Composite-Material Flexible Robot Arm", *Transactions of the ASME*, Vol. 114, March 1992, pp.96-102.
31. Gordaninejad, F. et al., "Nonlinear Dynamic Modelling of a Revolute-Prismatic Flexible Composite-Material Robot Arm", *Journal of Vibrations and Acoustics*, Vol. 113, Oct. 1991, pp.461-468.
32. Aerospace Composite Products, 14240 Doolittle Drive, San Leandro, California.
33. Top Sports Inc., 173 Peel St., Montreal, Quebec, 1997.
34. Lessard, L., course notes for "Mechanics of Composite Materials", McGill University, Montreal, 1995.
35. Beer, Ferdinand P., Johnston, E. Russell, "Mechanics of Materials: 2<sup>nd</sup> Edition", McGraw-Hill Inc., New York, 1992.
36. Applied Aerospace Structures Corporation, "Composite Training Course", Oct. 24<sup>th</sup>-27<sup>th</sup>, CA, 1995.
37. SDRC I-DEAS Master's Series V2.0, Integrated Design Engineering Software, user manual, Structural Dynamics Research Corporation, Milford, OH, 1994.

38. CIBA-GEIGY Selector Guide, Furane Aerospace Adhesives, 5121 San Fernando Rd., LA, CA, 1992.
39. Shokrieh, M., "MTS Shortened User's Manual", McGill University, 1994.
40. Adchem Corporation, Adbond High-Strength Structural Adhesive, 5300R resin and 5300H hardener.
41. The Advanced Composites Group, Technical Manual, Tulsa, Ok., 1996.
42. Amisol Company Ltd., Freekote 700NC, Lachine, Quebec, 1997.
43. Gougeon Brothers Inc., West-System Technical Manual, 860-8 Aluminum Etching Kit, Bay City, Mi., 1994.
44. PCB Peizelectronics Inc., ICP Accelerometer Calibration Data, model no. 303A03, serial no. 8665, 3425 Walden Ave., Depew, New York, 1985.
45. Massie et al., "Force Reflecting Haptic Interface", United States Patent # 5 587 937, Dec. 24, 1996.
46. Kazerooni, H., & Her, M.G., "The Dynamics and Control of a Haptic Interface Device", IEEE Transactions on Robotics and Automation, Vol.10, No.4, Aug.1994, pp. 453-464.
47. Choi. S.B, et. al., "Modeling and Control of a Single-Link Flexible Manipulator Featuring a Graphite-Epoxy Composite Arm", IEEE 1990, pp.1450-1455.
48. Papadopoulos, E. & Abu-Abed, A., "Design and Motion Planning for a Zero-Reaciton Manipulator", IEEE 1994, pp. 1554-1559.
49. Putré, Michael, "Space-age robots come down to earth", Mechanical Engineering, Jan, 1995, pp.88-89.
50. Konno, A., et al., "Vibration Controllability of Flexible Manipulators", IEEE 1994, pp.308- 314.
51. Thompson, B.S, & Sung, C.K., "An Analytical and Experimental Investigation of High-Speed Mechanisms Fabricated with Composite Laminates", Journal of Sound and Vibration, Vol.111, No.3, 1986, pp.399-428.
52. Bryfogle, M.D. et al., "Kinematics and Control of a Fully Parallel Force-Reflecting Hand Controller for Manipulator Teleoperation", Journal of Robotic Systems, Vol.10, No.5, 1993, pp.745-766.

# Appendix A

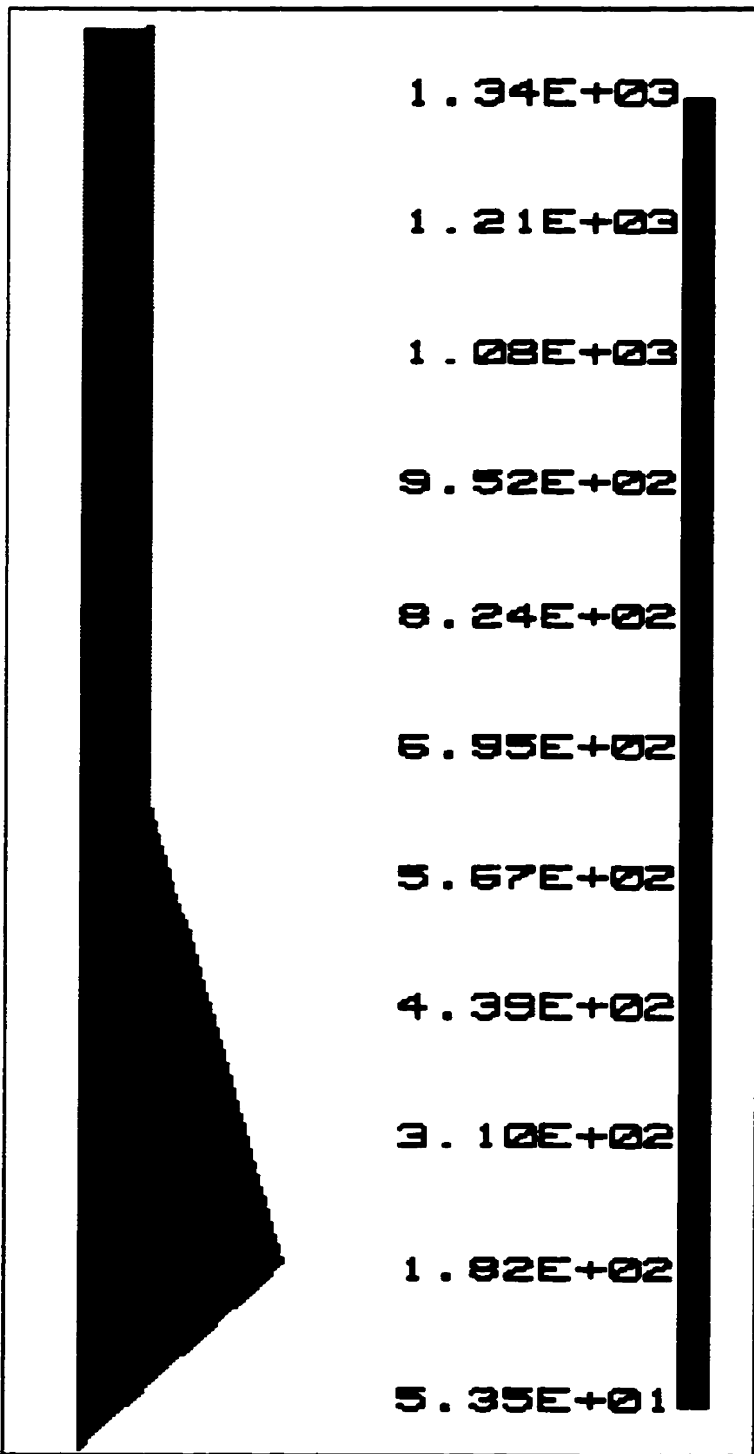


Figure A 1- Test 1.4

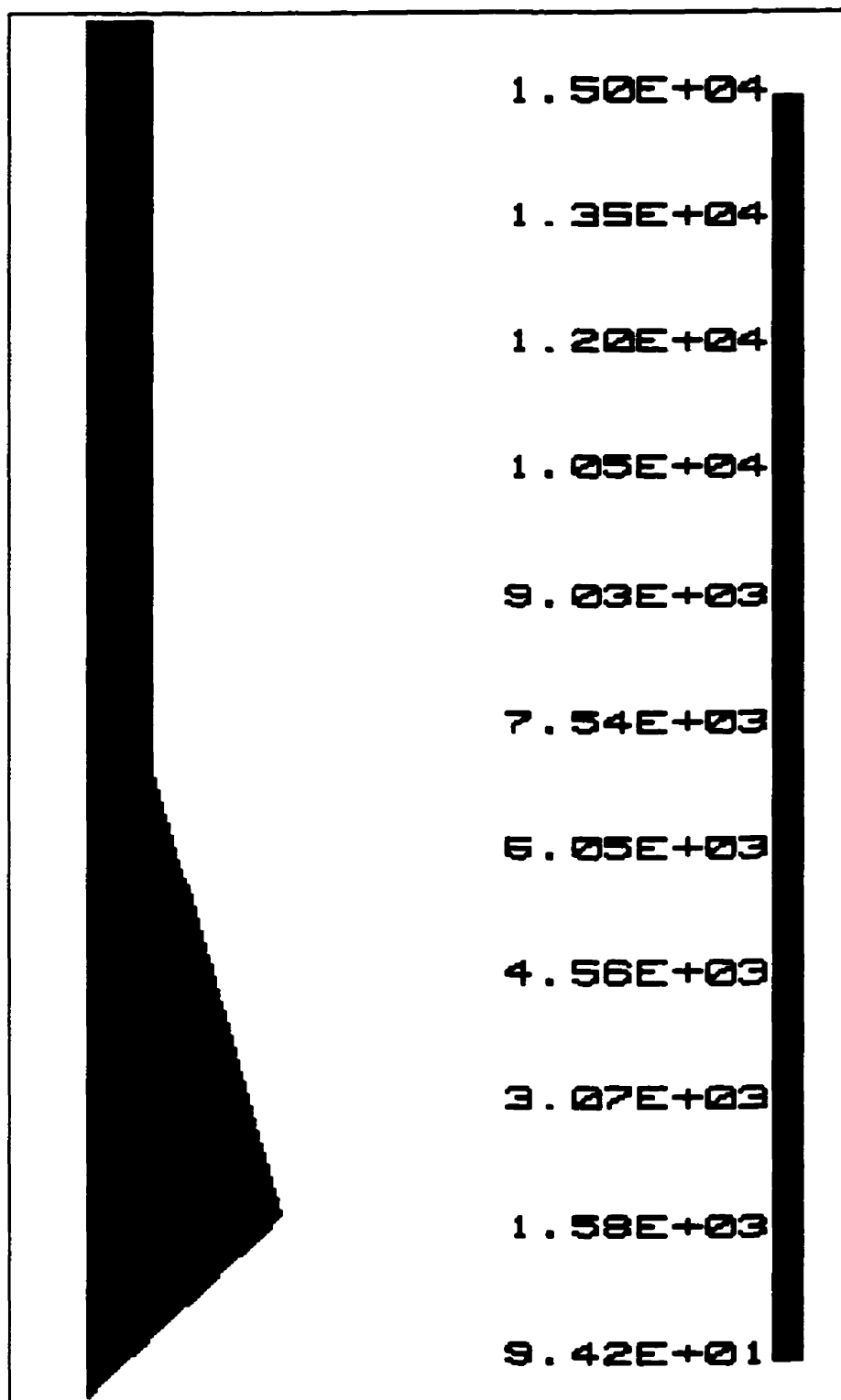


Figure A 2 - Test 1.1

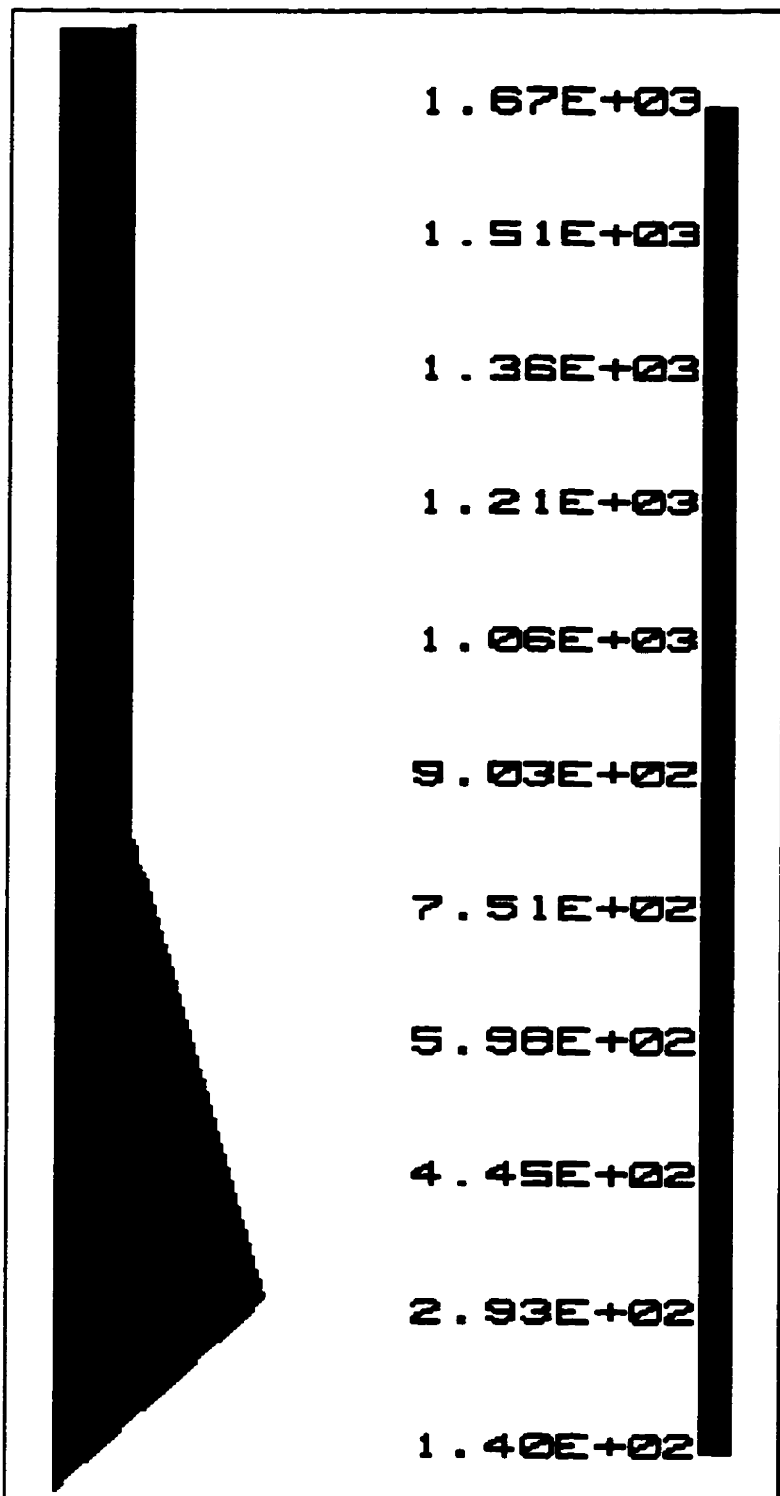


Figure A 3- Test 2.4

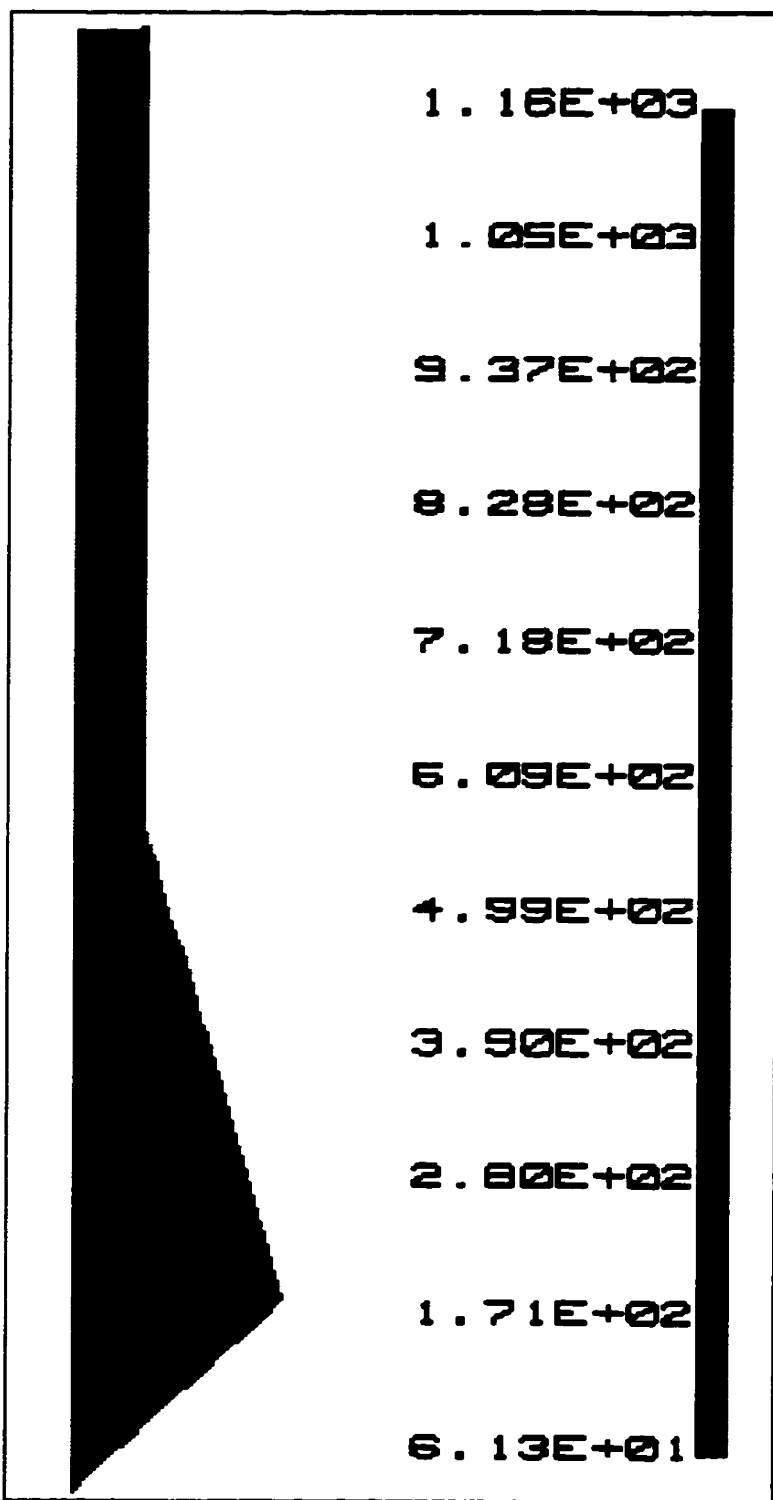


Figure A 4 - Test 3.4

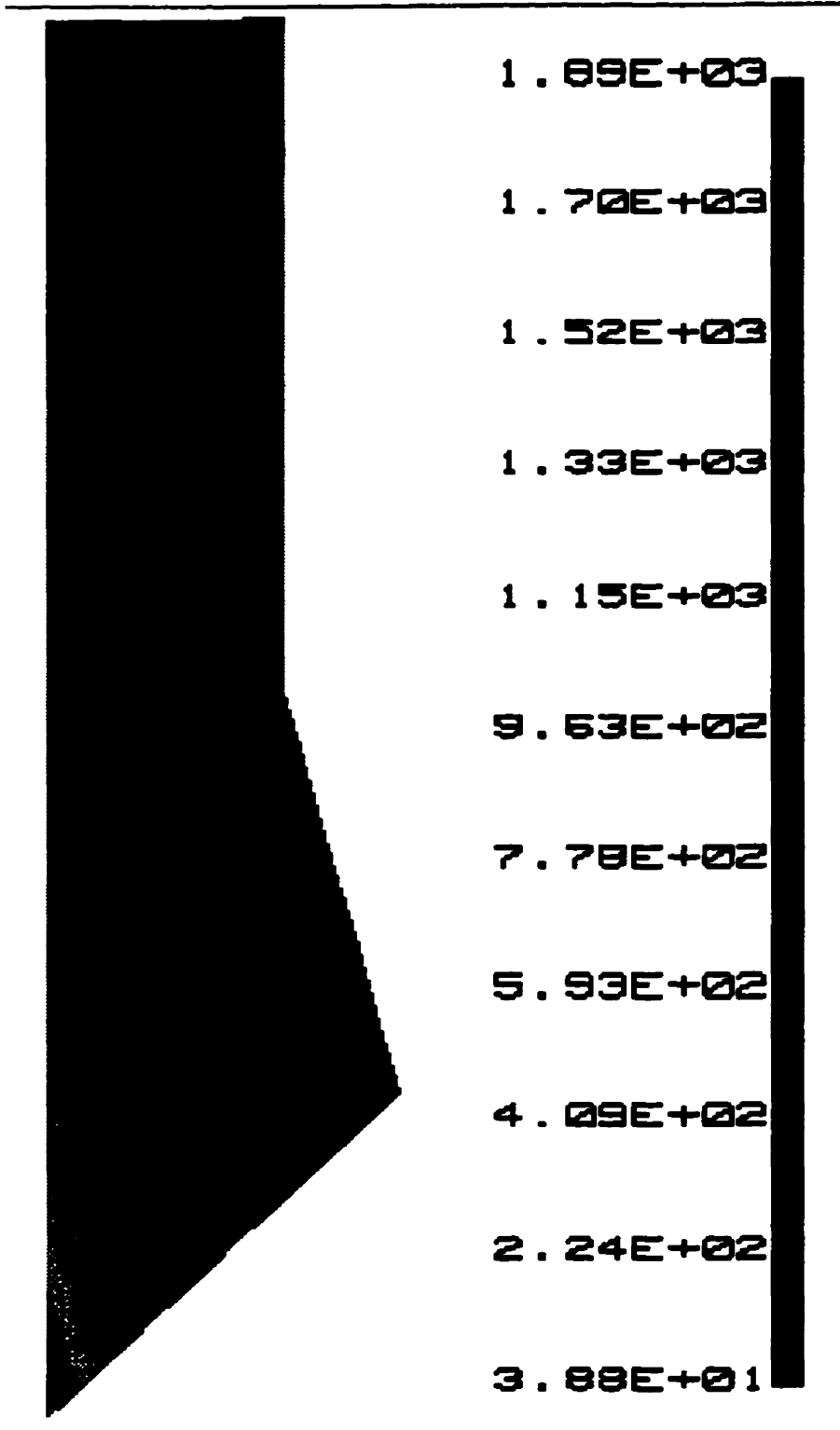


Figure A 5 - Test 4.4

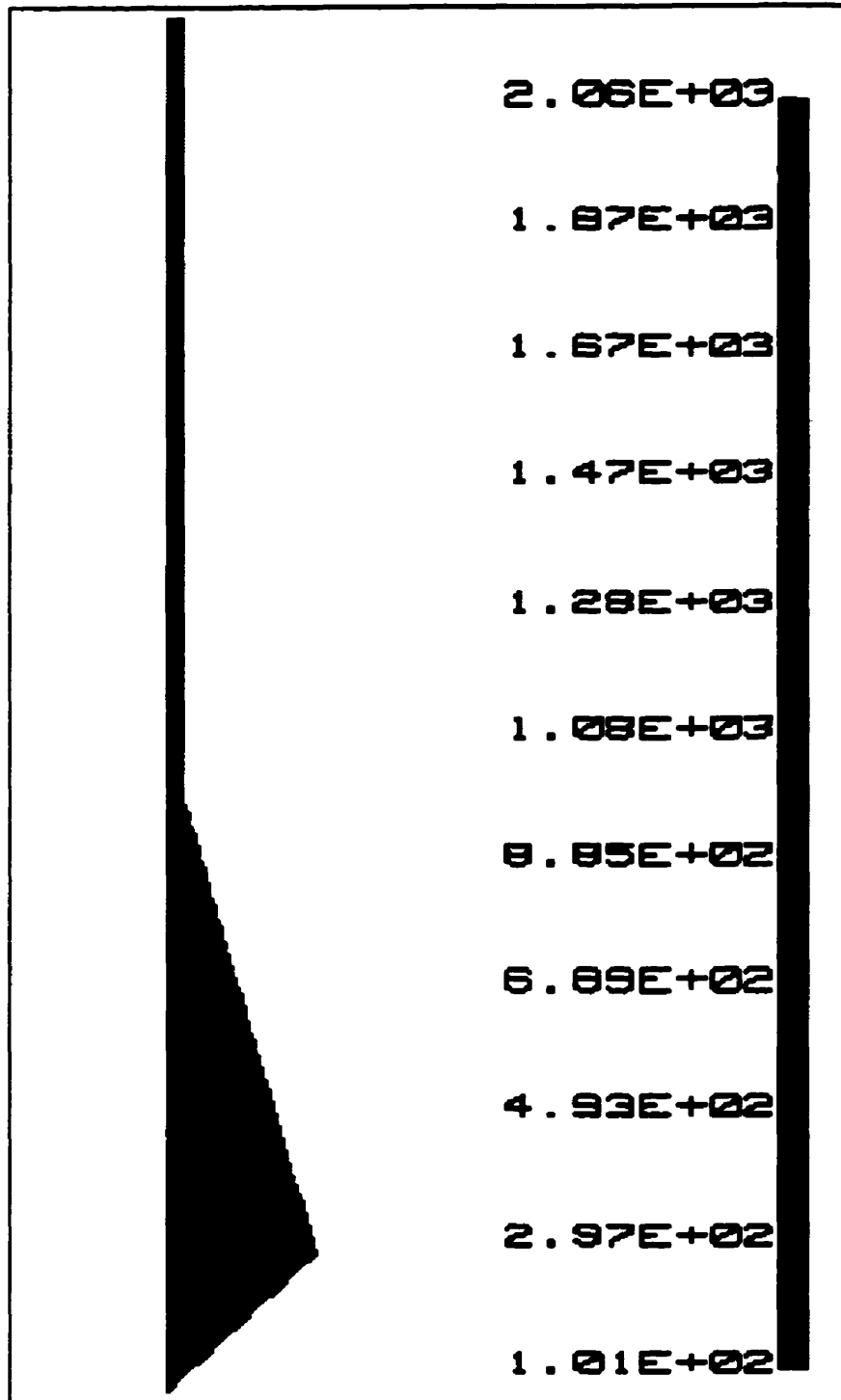


Figure A 6 - Test 5.4

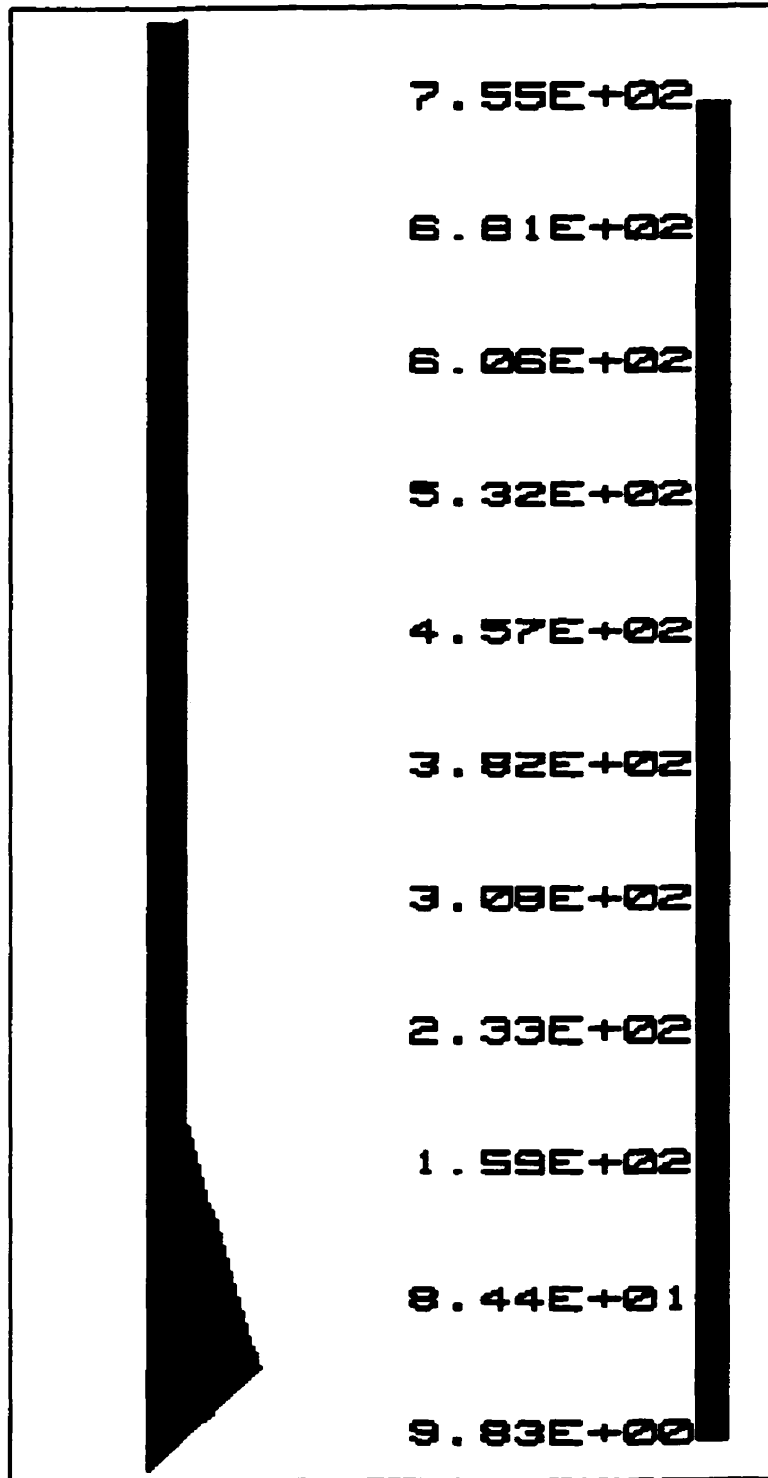


Figure A 7 - Test 6.4

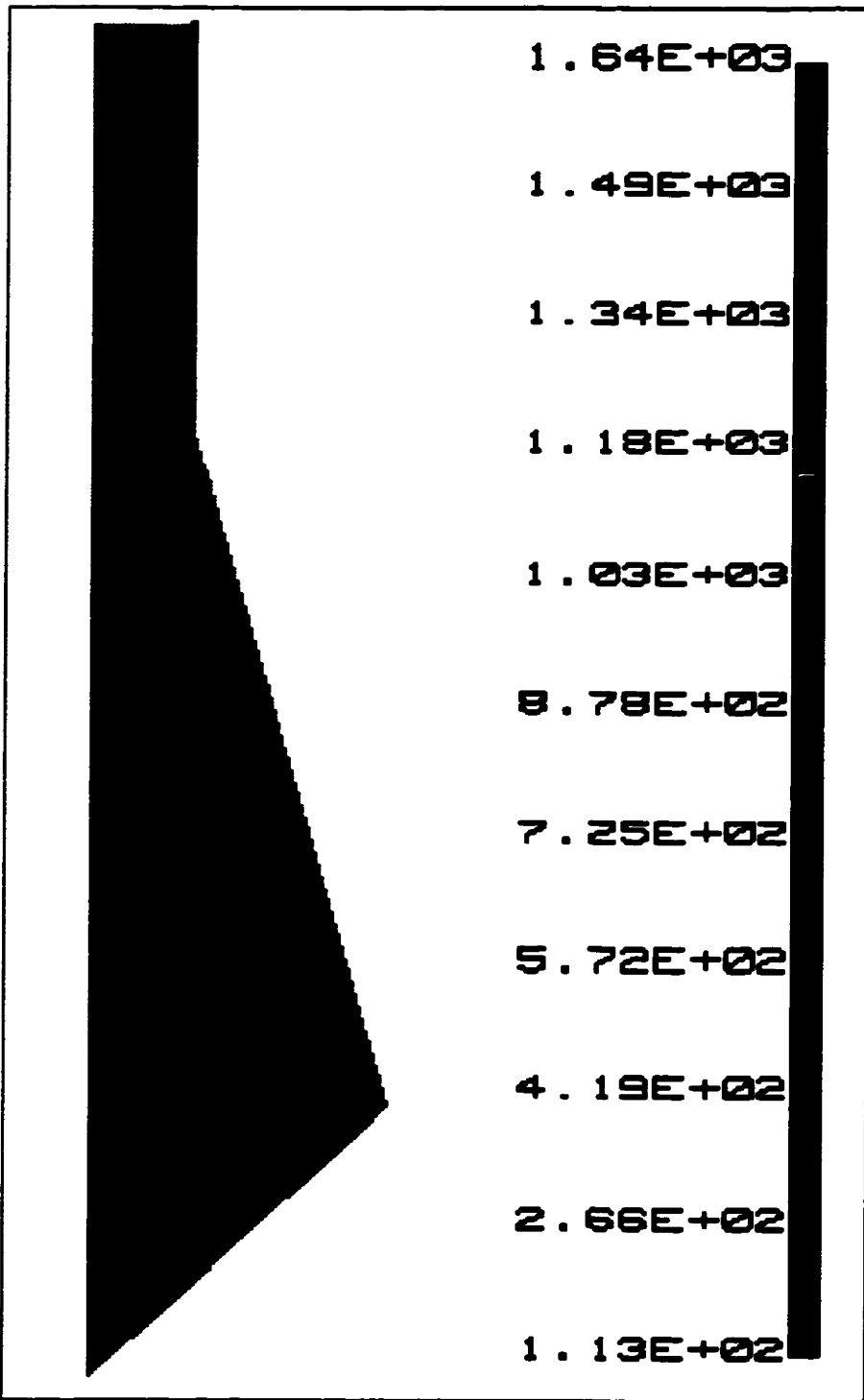


Figure A 8 - Test 7.4

# 10. Appendix B

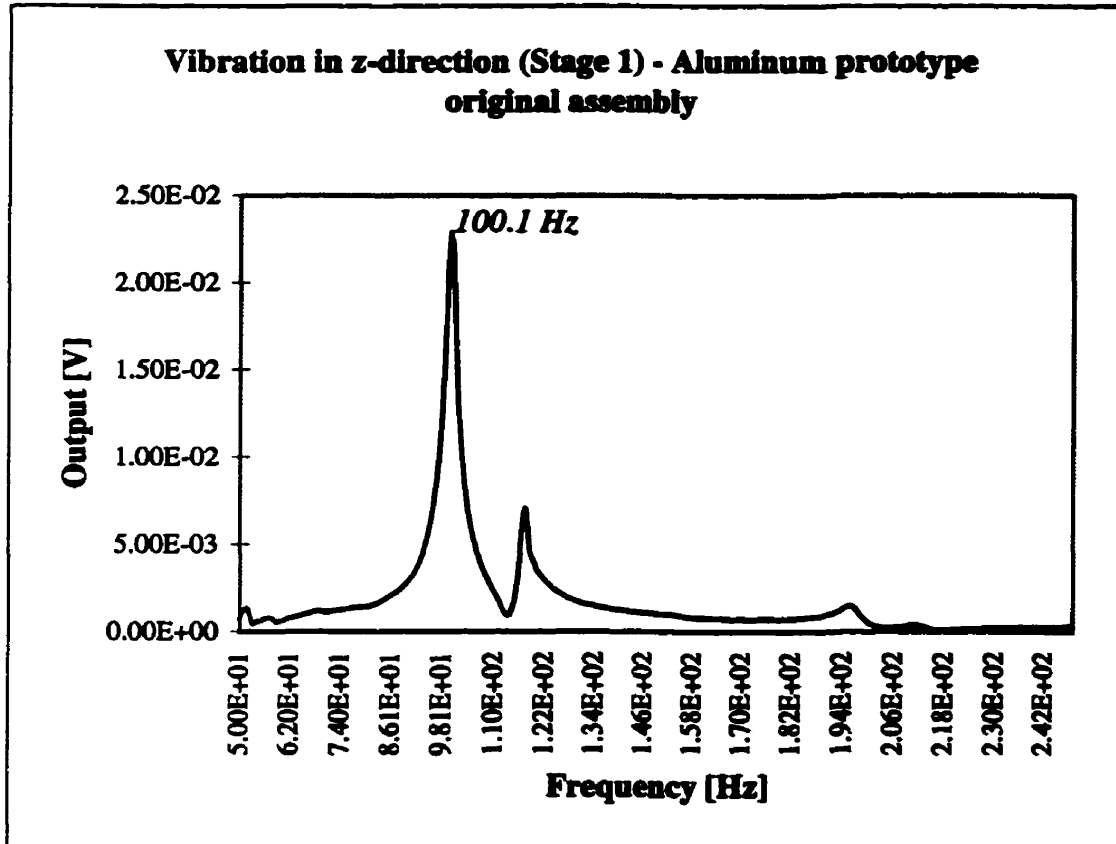


Figure B 1

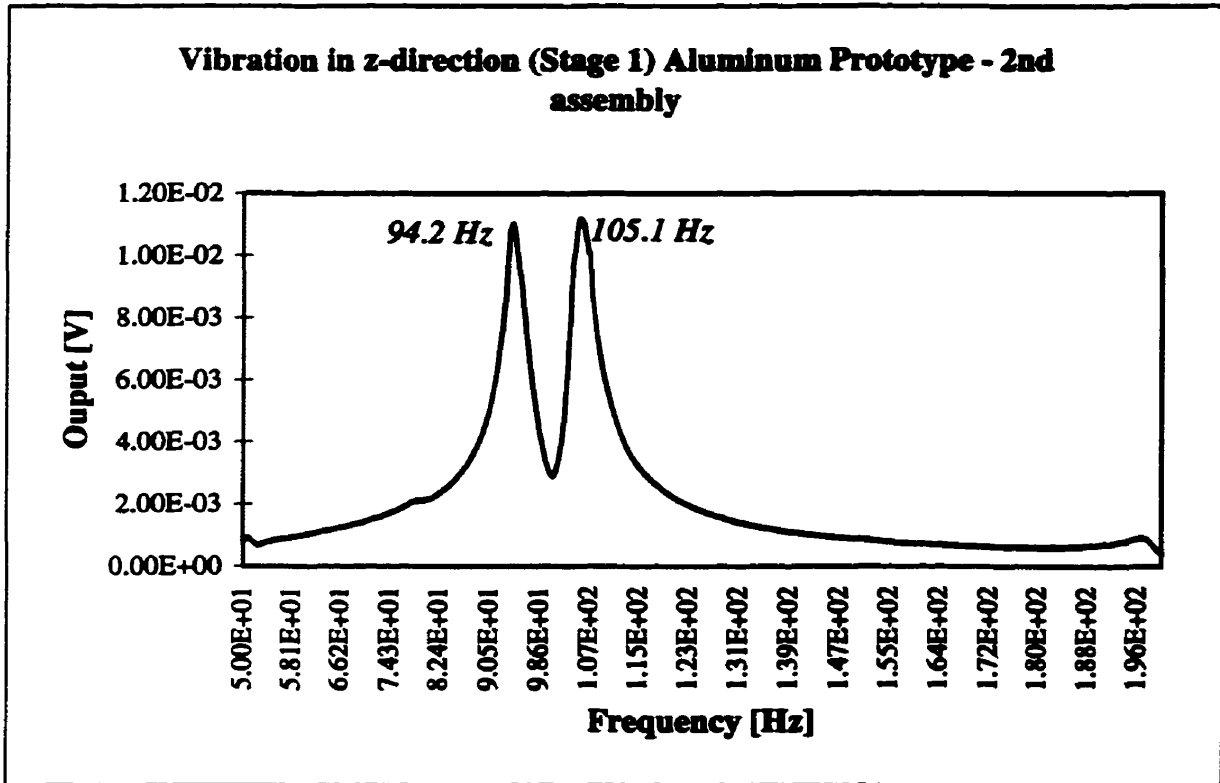


Figure B 2

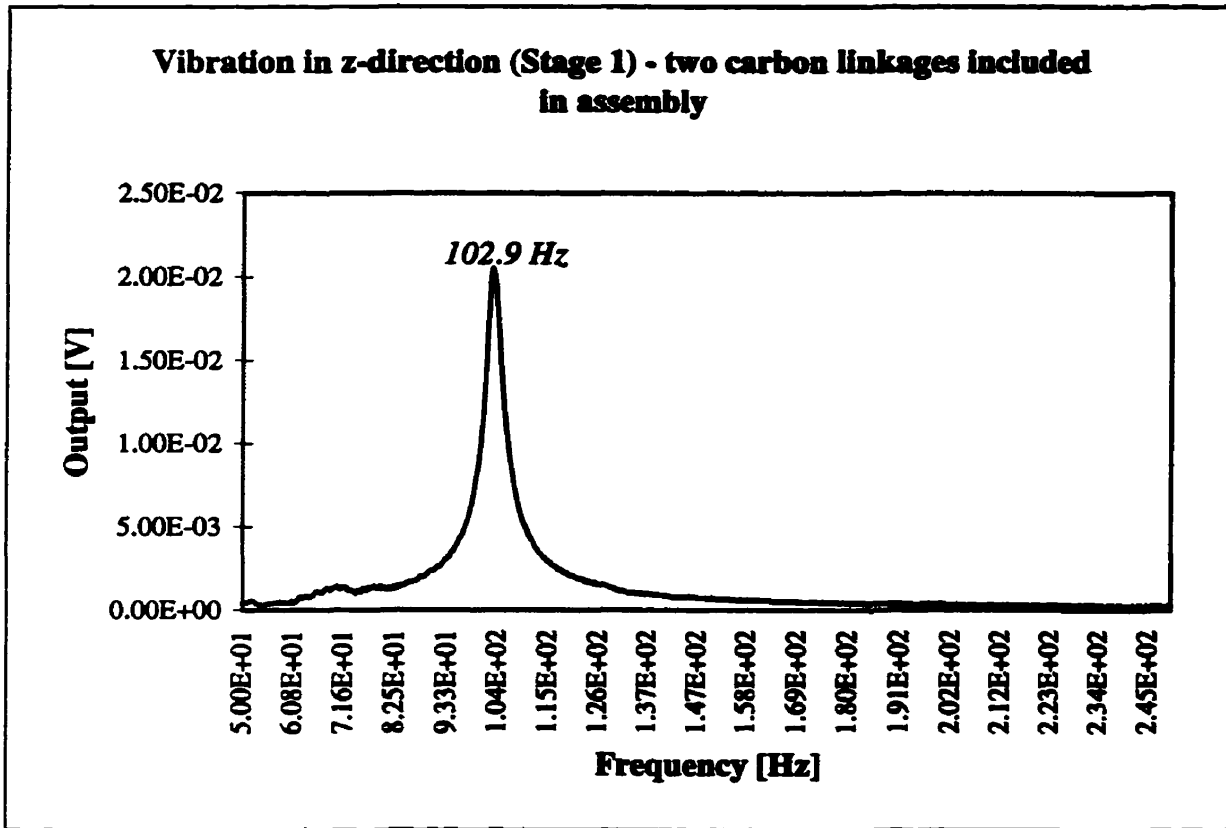


Figure B 3

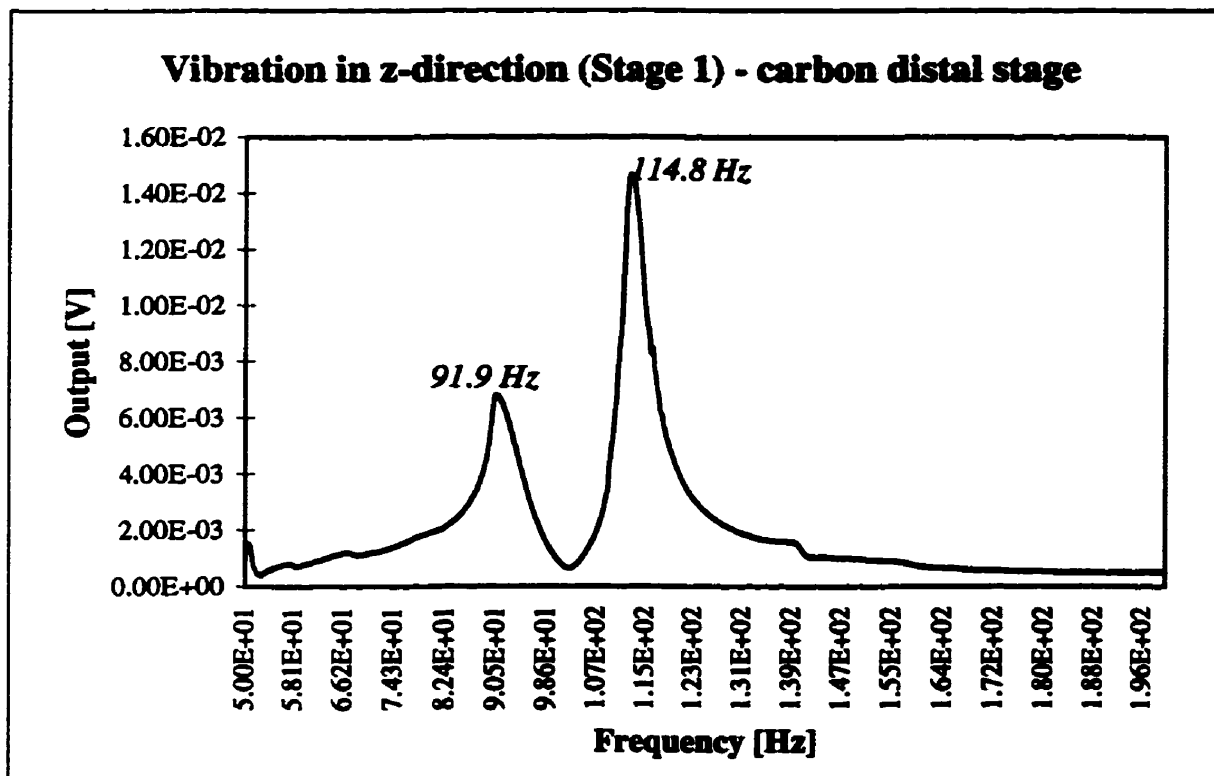


Figure B 4

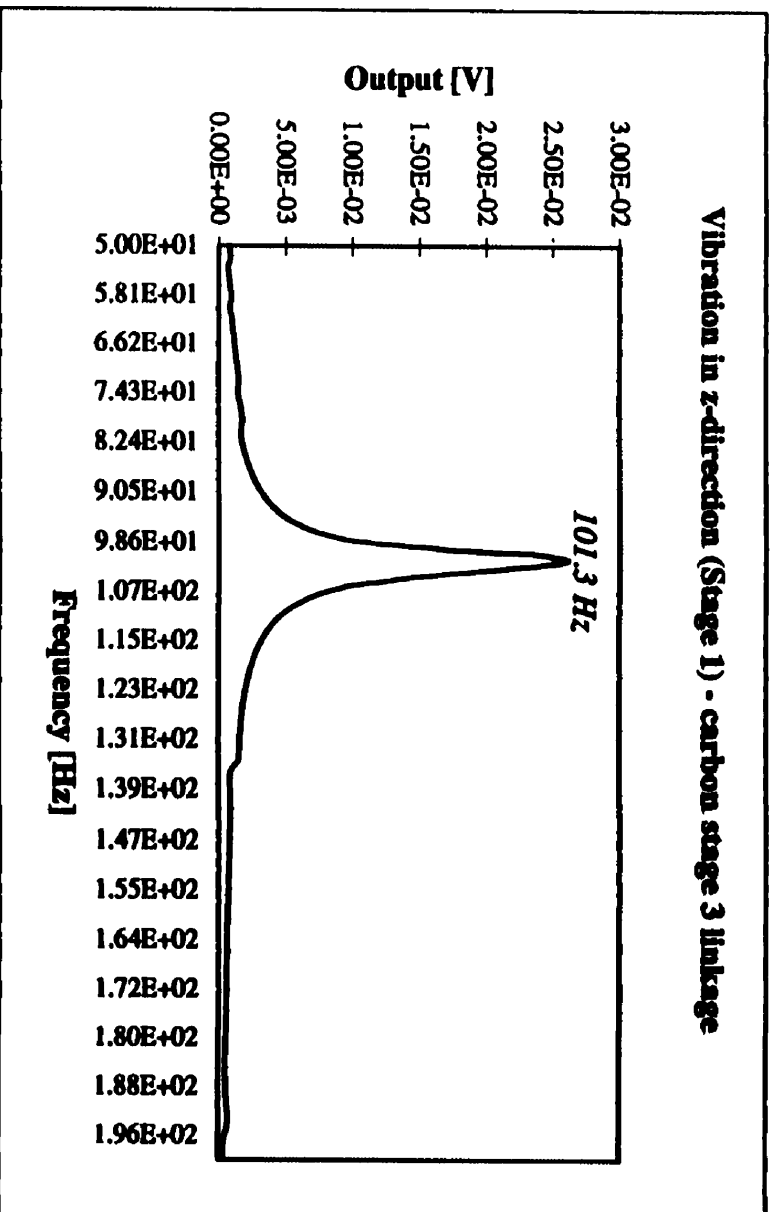


Figure B 5

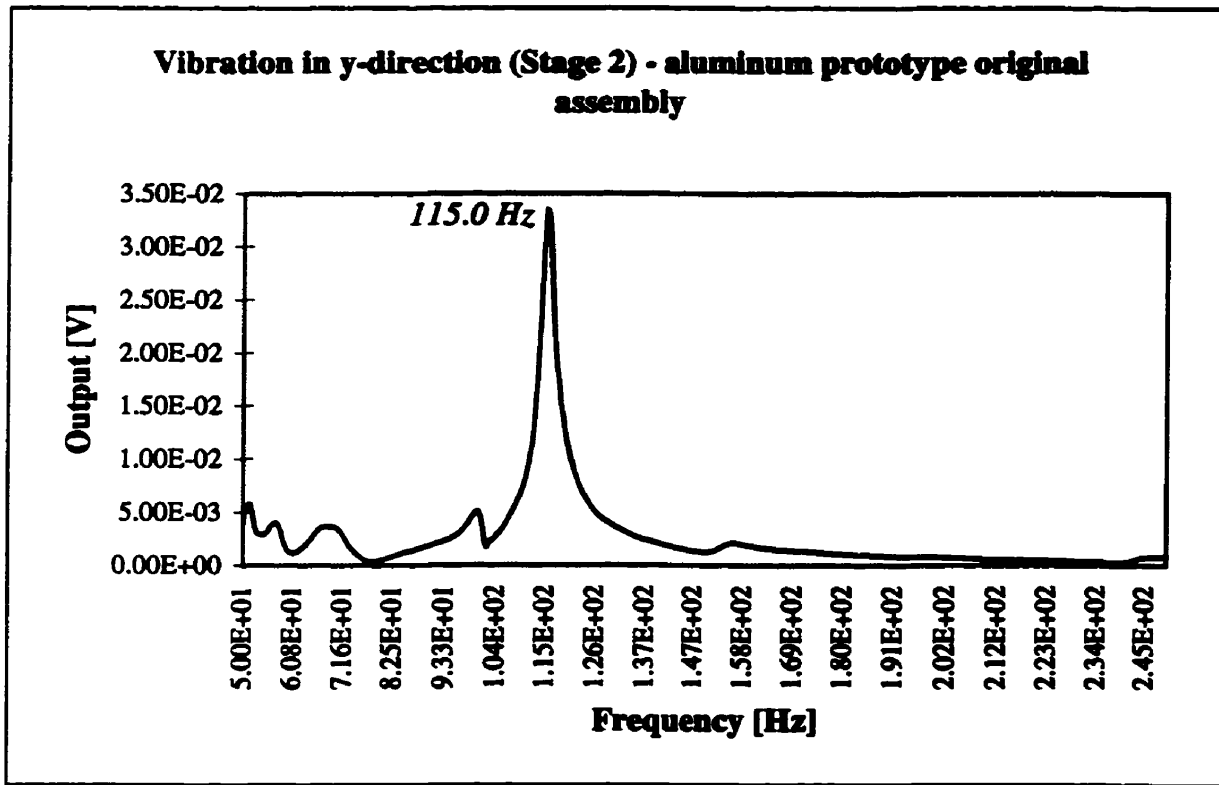


Figure B 6

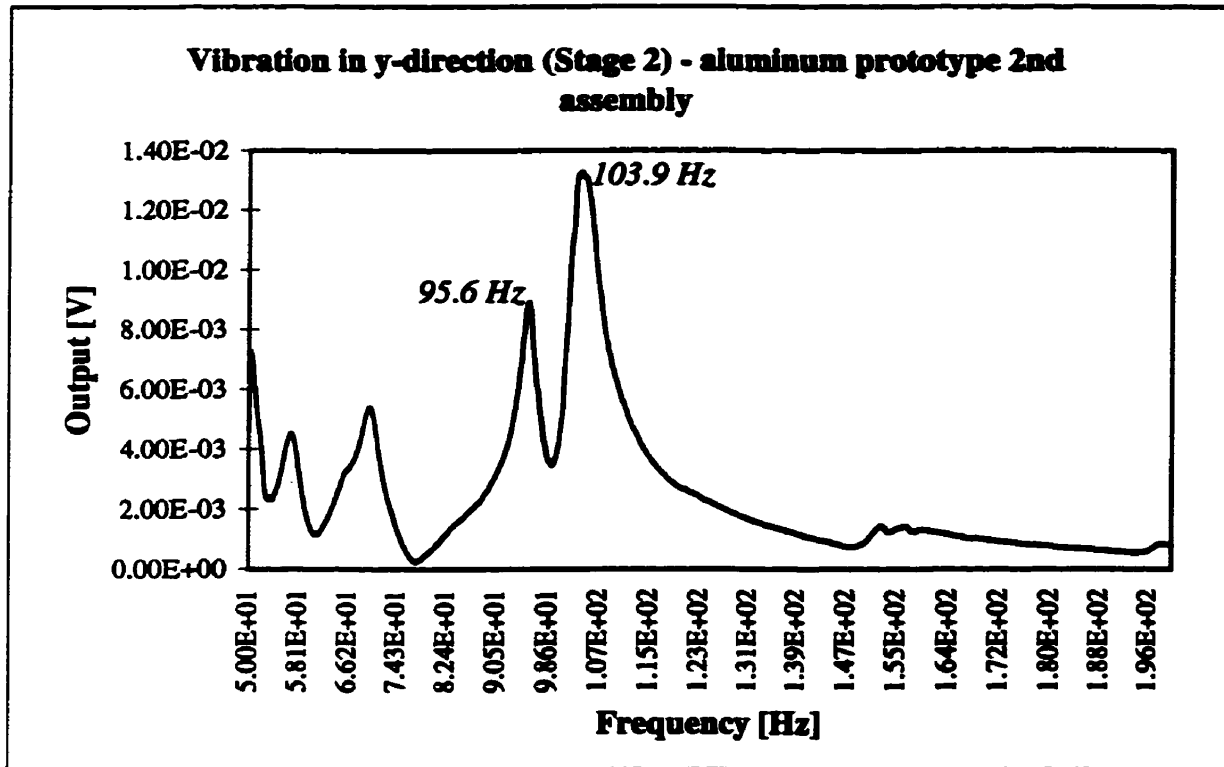


Figure B 7

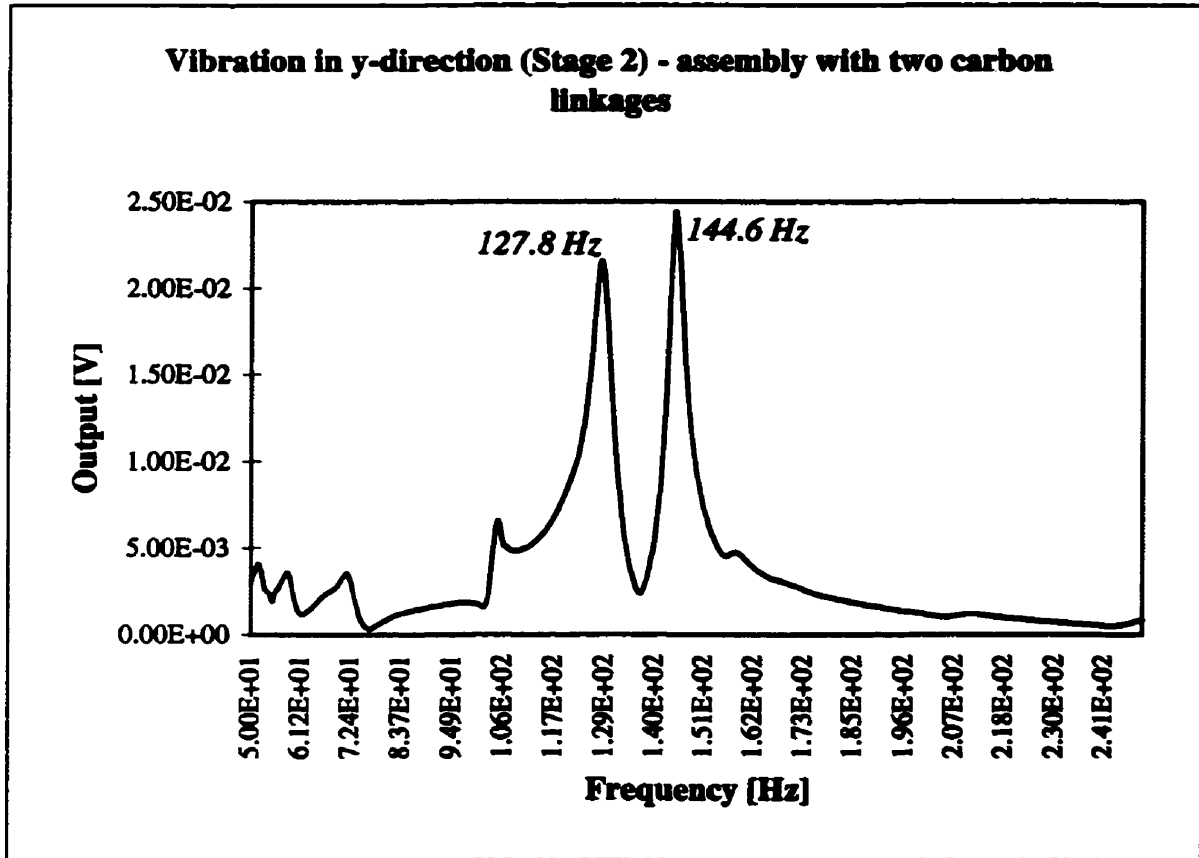


Figure B 8

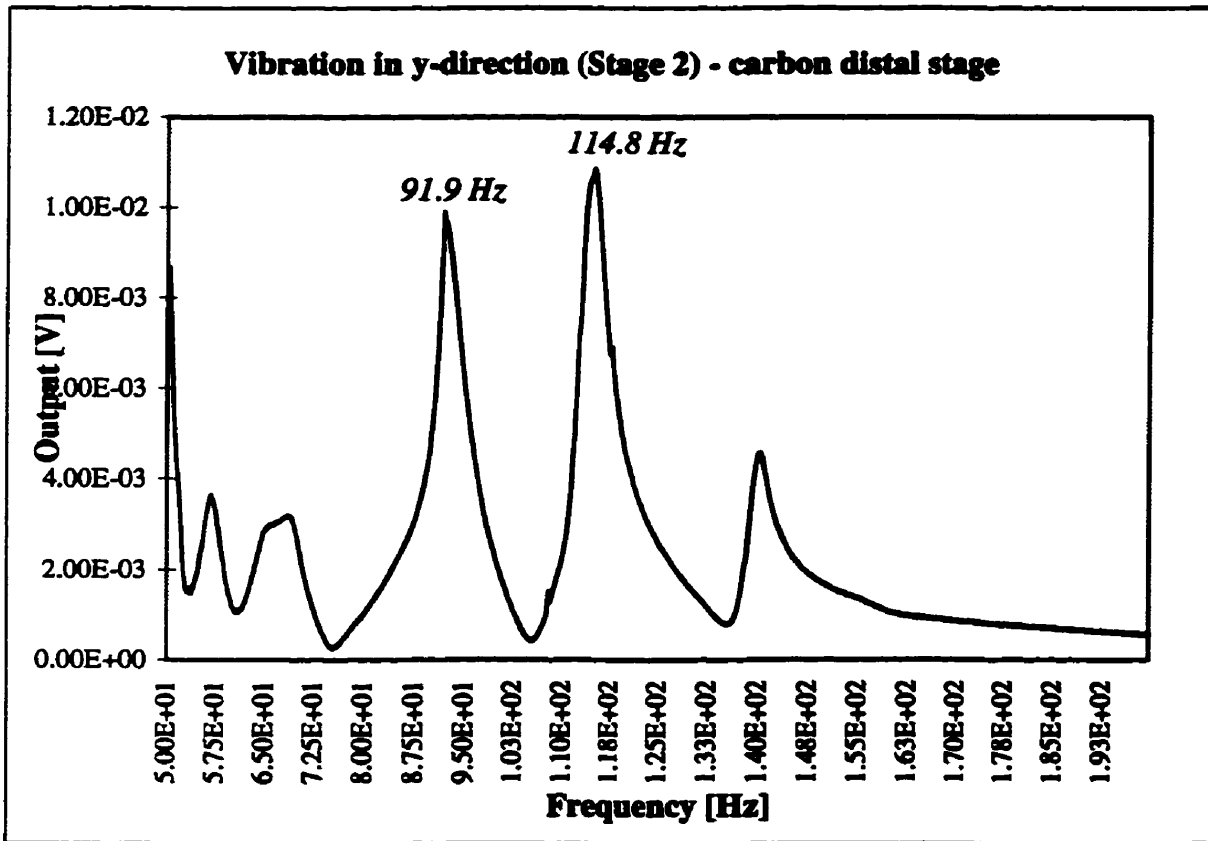


Figure B 9

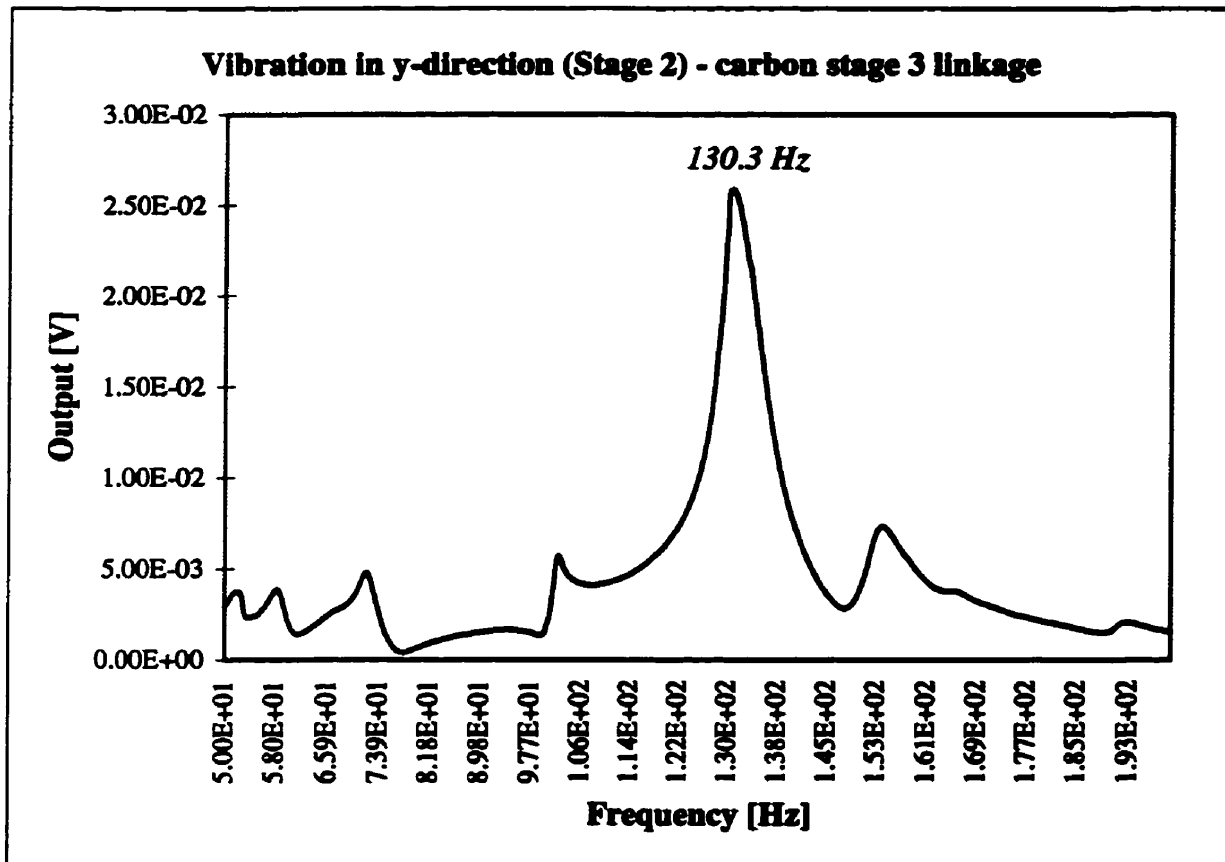


Figure B 10

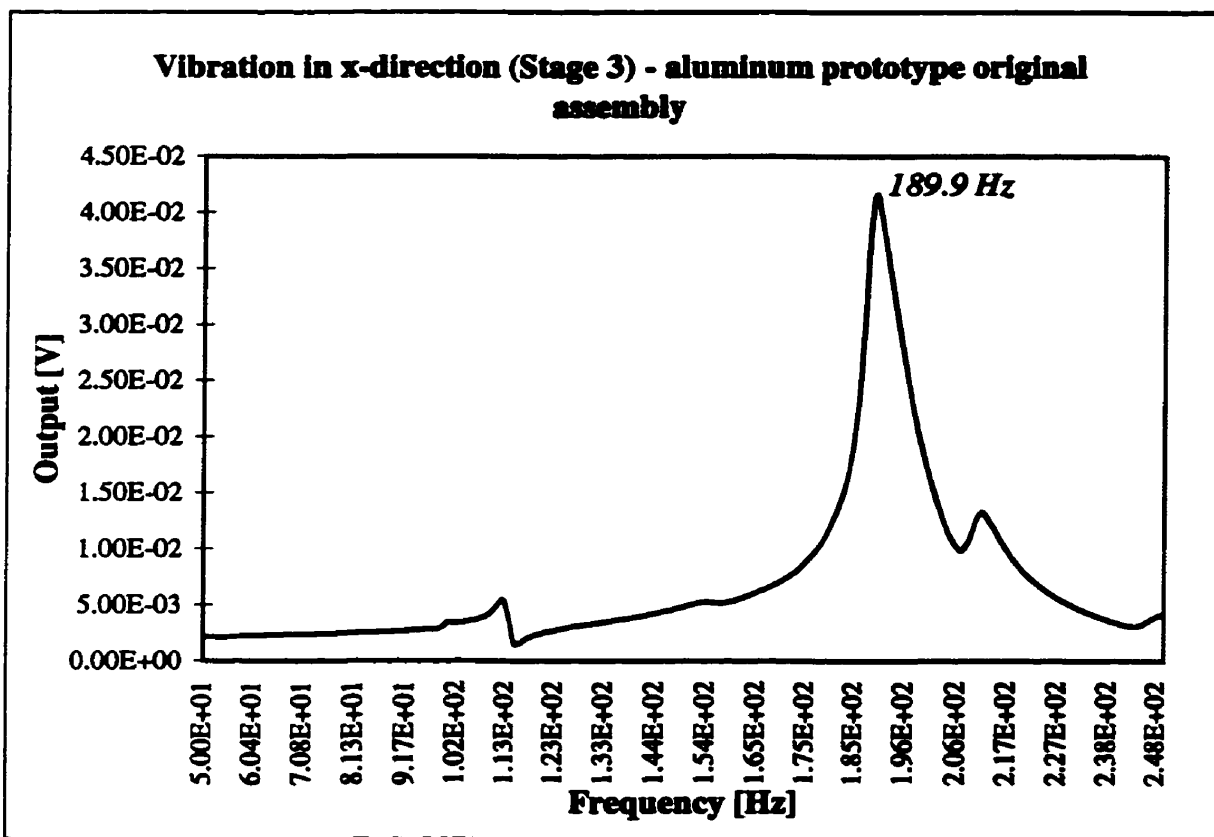


Figure B 11

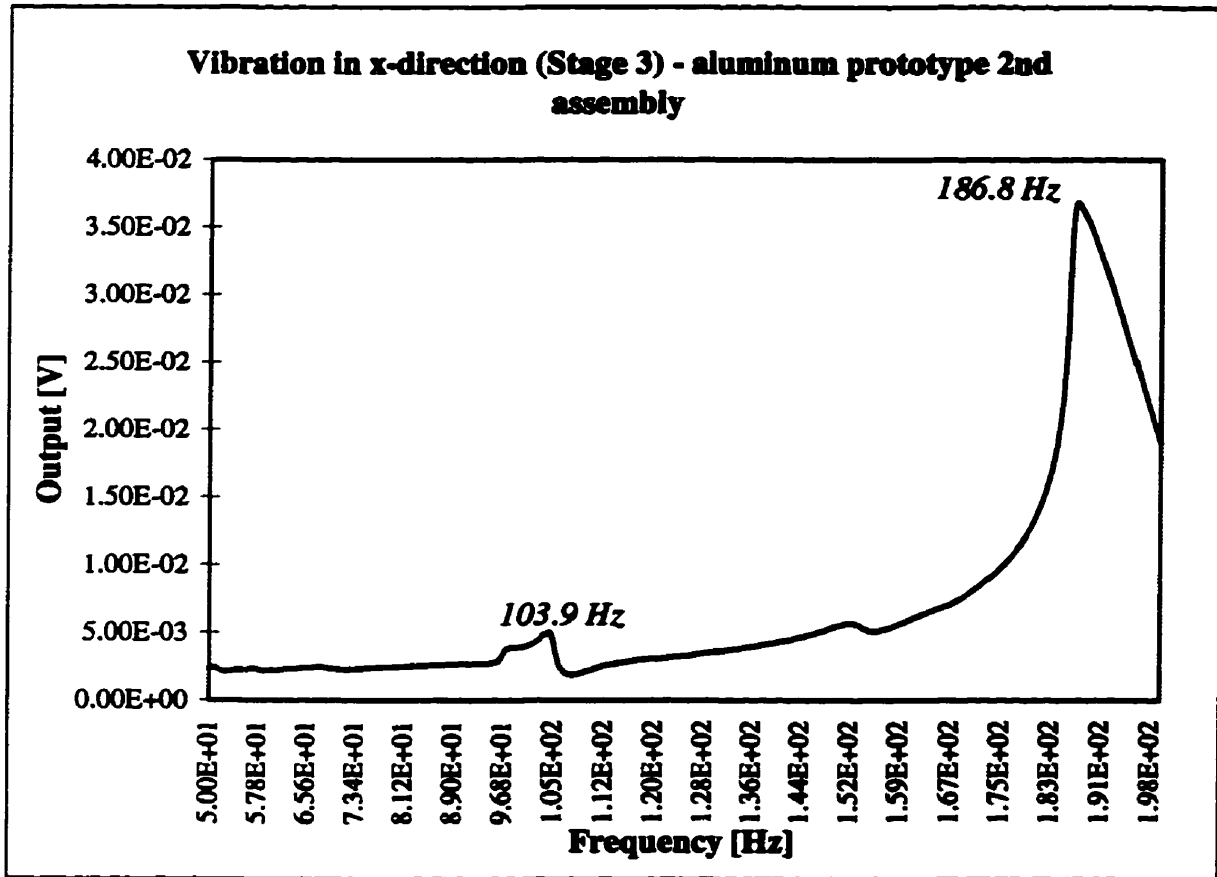


Figure B 12

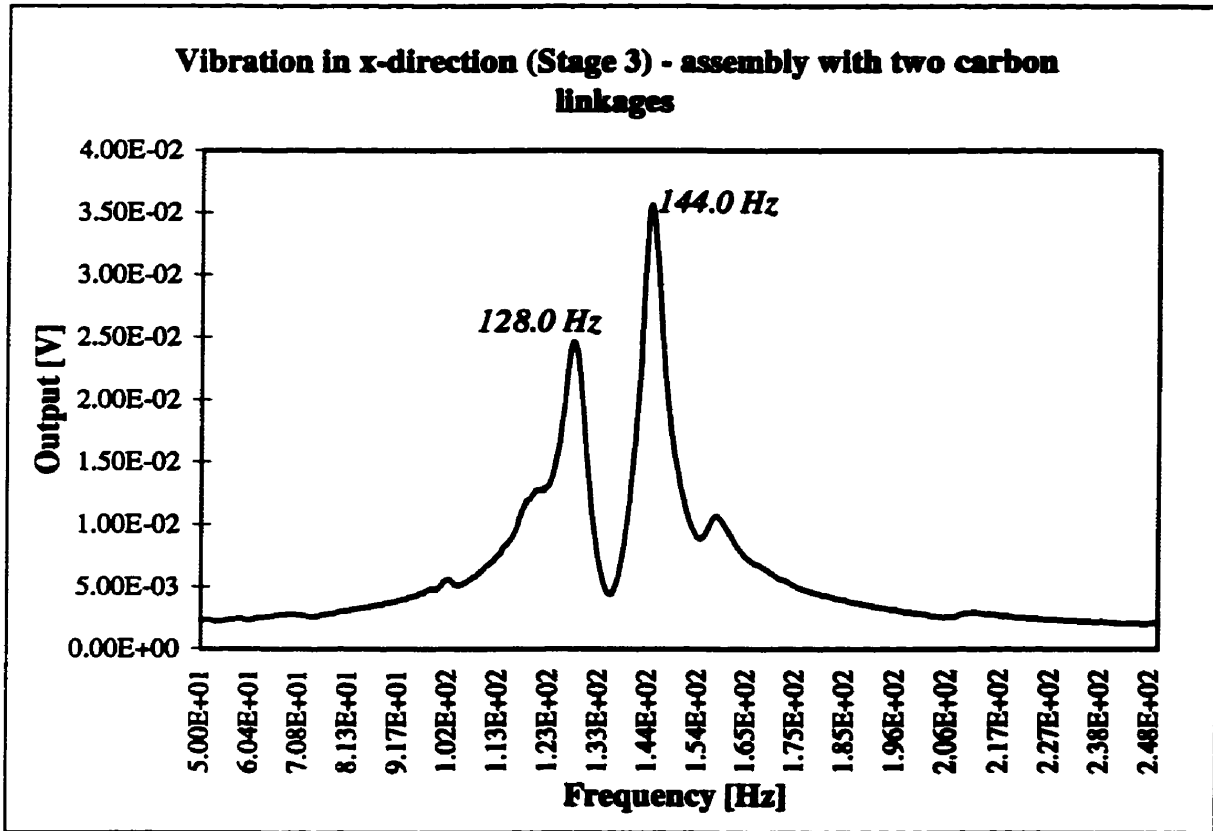


Figure B 13

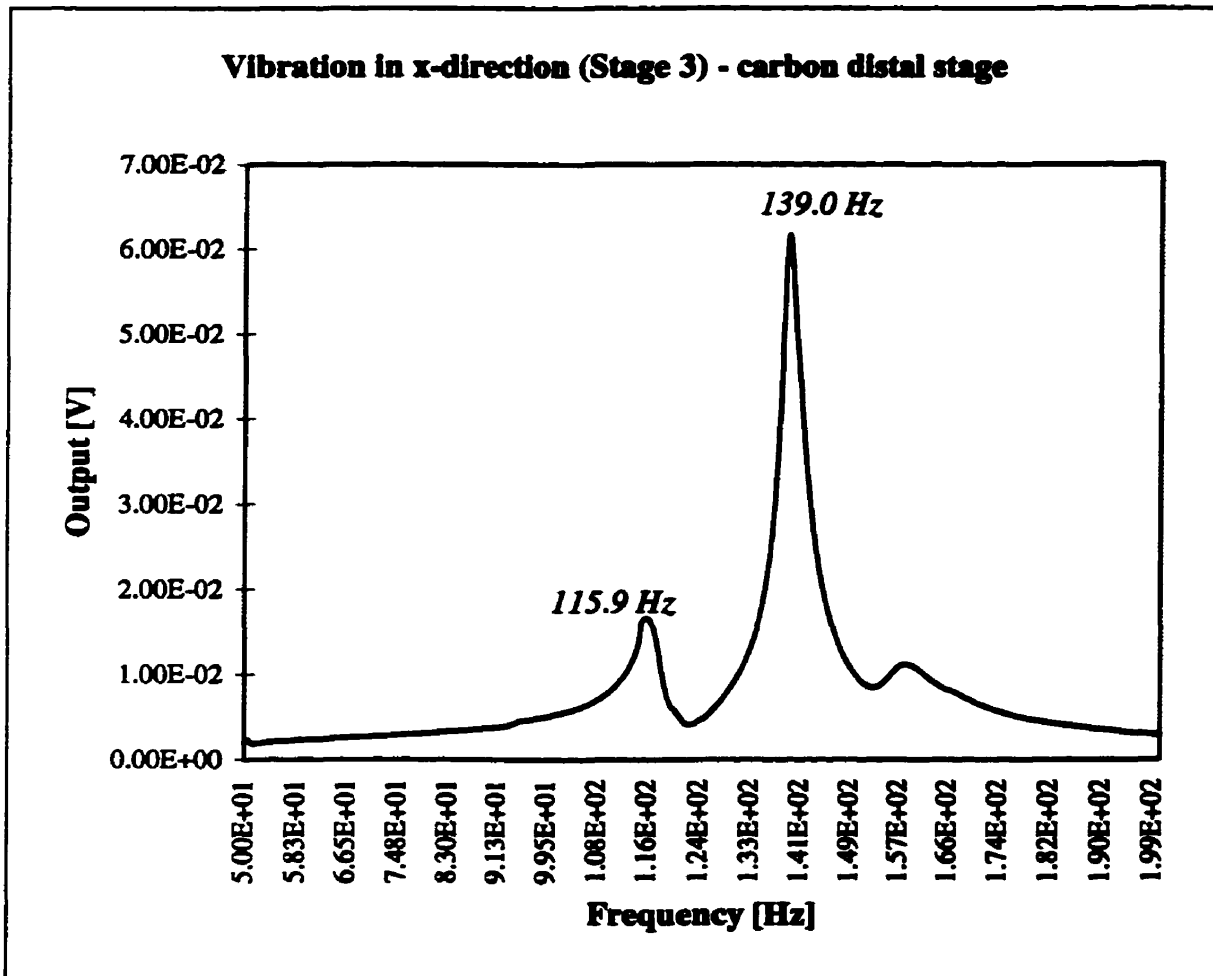


Figure B 14

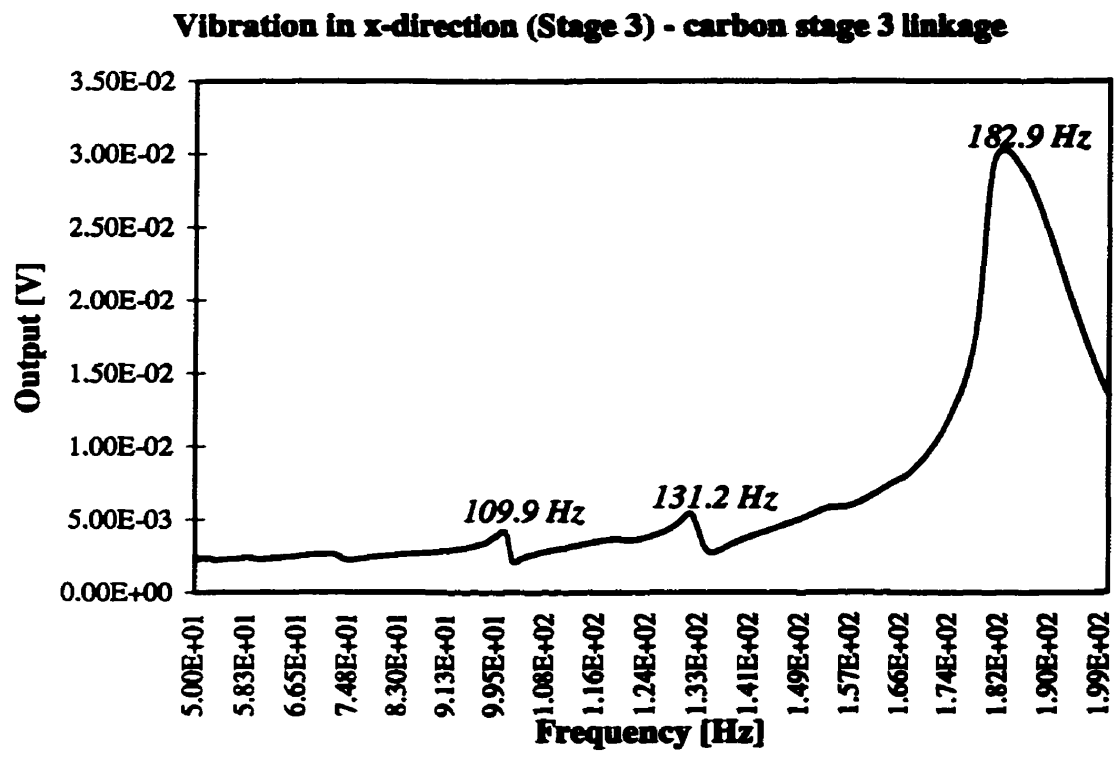


Figure B 15